Opto-electrical approach to visualize magnetic nanostructures of chiral antiferromagnets

Dissertation

Zur Erlangung des Doktorgrades der Naturwissenschaften
(Dr. rer. nat.)

der

Naturwissenschaftlichen Fakultät II
Chemie, Physik und Mathematik

der Martin-Luther-Universität
Halle-Wittenberg Vorgelegt von

Herrn Atul Pandey

Gutachter:
Prof. Dr. Georg Woltersdorf
Prof. Dr. Stuart S.P. Parkin
Prof. Dr. Sebastian T. B. Goennenwein

Tag der öffentlichen Verteidigung:
02.07.2025

Dedicated to

My Father

Jagat Narayan Pandey

And every other farmer of the world whose work ensures food on our plates

Eidesstattliche Erklärung

Hiermit erkläre ich, dass ich die vorliegende Arbeit selbstständig verfasst und keine anderen als die angegebenen Quellen und Hilfsmittel benutzt habe. Alle Stellen der Arbeit, die wörtlich oder sinngemäß aus anderen Quellen übernommen wurden, sind als solche kenntlich gemacht. Ich habe keine vergeblichen Promotionsversuche unternommen und keine Dissertation an einer anderen wissenschaftlichen Einrichtung zur Erlangung eines akademischen Grades eingereicht. Ich bin weder vorgestraft noch sind gegen mich Ermittlungsverfahren anhängig.

Halle (Saale), den 27.10.2024,

Atul Pandey

Acknowledgments

This work has been possible with the support of many people, both professionally and through moral support, providing mental strength in a long, four-year journey.

I would like to express my sincere gratitude to Prof. Dr. Georg Woltersdorf for giving me the opportunity to pursue a PhD in his group. His technical expertise and very comprehensive knowledge of physics always provided a fruitful scientific discussion. I am very thankful to him for giving me the freedom to perform experiments and showing trust in me, at the same time encouraging me to do better and improve things. This helped me to build a scientific temper and to grow as a scientist.

The state-of-the-art research infrastructure brought to MPI, Halle by Prof. Dr. Stuart Parkin helped me to increase the efficiency of my research work. His friendly and constructive comments during our scientific discussions aided in the better planning of my experiments.

I owe a special thanks to Jitul Deka for his selfless and relentless efforts in fabricating the device structures for the ANE measurements. I genuinely admire his trust in me during the times when several measurements did not succeed. His prompt actions enabled me to try one thing after another until we could see the light at the end of a long tunnel.

Reflecting on the content of this thesis makes me better realize the meaning of the metaphor "standing on the shoulders of giants". The work presented here stands upon several shoulders, whom I would like to acknowledge as follows:

- Jitul Deka: fabrication of device structures and micromagnetic simulations.
- James Mark Taylor and Edouard Lesne: guidance in the field of noncollinear antiferromagnets and providing Mn_3Sn samples.
- Chris Koerner: expertise in SNOM and scientific discussions.
- Rouven Dreyer and Palvan Seyidov: construction of the experimental setup for the HDP measurements that I later modified for carrying out ANE studies.
- Jiho Yoon: fabrication of Mn_3Sn nanowire structures with E-beam and providing PMA racetrack nanowire devices.

I appreciate the very sincere efforts from Prajwal Rigvedi for depositing several Mn_3Sn films that helped me to figure out non-magnetic signals in ANE measurements of these samples.

I would like to thank all my group members and colleagues for their help with resolving technical and scientific problems, especially Chris, Rouven, James, and Wolfgang Hoppe. I also thank Saban Tirpanci for teaching me E-beam lithography and sputter deposition. This was further assisted by Niklas Liebing (lithography) and Wolfgang (sputter deposition). I thank Binoy Krishna Hazra for providing the PMA sample for the HDP measurements. I thank Aleksandra Stakhnova for the excellent 3D graphics that helped to represent our experimental results better.

For taking their valuable time to proofread and improve this thesis, I thank Rouven, Wolfgang, Berthold Rimmler, Abhay Kant Srivastava, Sagar Gambhira, Varun Ramaprasad (from California University, San Diego), Souvik Das, Pranava Keerthi Sivakumar, and Banabir Pal.

For the administrative support, I thank Tobias, Robert, Antje, Kathrin, and Kristin. I appreciate the friendly and supportive response from Tobias and Kristin.

Through this journey, I learned that even a challenging task in difficult circumstances could be accomplished in the surroundings of people with helping hands, sympathetic words, listening ears, and well wishes in the heart. I am happy to have had my colleague Rouven, who has always been there to listen to my concerns and make me feel heard. I share equal credit for this work with my other half, my very dear Anvi. Her companionship and love is what motivates me to do what I do. I appreciate her patience and support through all this, especially during the last year when I was so lost in work that I could not be with her even when I was with her. I thank my brother Anuj and my mother Rajeshvery for not letting me feel alone, even from thousands of miles away. I am also grateful to my master's thesis supervisor, Prof. Chiranjib Mitra, for guiding and mentoring me through all the difficult decisions I had to make. And last, but by no means least, I thank all the friends making the last four years lively and cold winters warm: Jitul, Srishti, Aakash, Aakanksha, Sanjana, Abhi, and Nupur.

Abstract

This dissertation presents magnetic domain imaging methods based on Berry curvature-driven optical and magnetotransport responses. The goal is to investigate chiral antiferromagnetic materials, which are ideal for spintronic applications. Major features of antiferromagnets (AFs) are high speed dynamics and negligible stray fields that allow for miniaturization. While the readout signal in collinear AFs, generally based on anisotropic magnetoresistance, is not large enough for practical utilization, chiral noncollinear AFs show strong optical and magnetotransport signals associated with the nontrivial topology of their band structures. The optical responses include magnetic circular dichroism (MCD) and magneto-optical Kerr effect. Similarly, magnetotransport responses based on anomalous Nernst effect (ANE) or anomalous Hall effect are used to deduce magnetic ordering in these materials.

In this work, spatially resolved MCD or ANE signals are measured to image magnetic domains. Here, laser heating generates an electrical response based on these effects. In the first step, we show that the MCD-based approach can image out-of-plane (OOP) magnetized materials that show a large MCD signal. Next, we use ANE-based readout to image magnetic domains in both the in-plane and the OOP ferromagnetic thin films with nanoscale spatial resolution. The ANE signal is directly proportional to the magnetization and a temperature gradient. For meaningful ANE-based imaging, it is crucial to know the characteristics of this gradient. We deduce spatial distribution and the magnitude of the nanoscale temperature gradient by studying a well-defined magnetic texture.

Finally, a manganese-based Weyl semimetal (Mn_3Sn) exhibiting a noncollinear AF ordering is studied. The hexagonal crystal structure of the compound hosts a Kagome plane on which Mn atoms form an inverse triangular spin structure. A small net moment in the Kagome planes that can couple to an external magnetic field allows the magnetic ordering to be switched. The field-induced switching in Mn_3Sn is observed with the spatially resolved ANE measurements down to nanoscale regime. The observed results are compared with the MOKE-based hysteresis measurements.

Zusammenfassung

In dieser Dissertation werden Bildgebungsmethoden für magnetische Domänen vorgestellt, welche durch die Berry-Krümmung gesteuert werden können. Ziel ist es, chirale antiferromagnetische Materialien zu untersuchen, die ideal für spintronische Anwendungen sind. Hauptmerkmale von Antiferromagneten (AFs) sind die schnelle Dynamik und vernachlässigbare Streufelder, die eine Miniaturisierung ermöglichen. Während das Auslesesignal in kollinearen AFs, das im Allgemeinen auf dem anisotropen Magnetwiderstand beruht, für die praktische Anwendung nicht groß genug ist, zeigen chirale nichtkollineare AFs starke optische und magnetische Signale, die mit der nichttrivialen Topologie ihrer Bandstrukturen zusammenhängen. Zu den optischen Reaktionen gehören der magnetische Zirkulardichroismus (MCD) und der magneto-optische Kerr-Effekt. In ähnlicher Weise werden Magnetotransportantworten, die auf dem anomalen Nernst-Effekt (ANE) oder dem anomalen Hall-Effekt beruhen, verwendet, um die magnetische Ordnung in diesen Materialien abzuleiten.

In dieser Arbeit werden räumlich aufgelöste MCD- und ANE-Signale gemessen, um magnetische Domänen abzubilden. Hier erzeugt die Laser-induzierte Erwärmung eine elektrische Reaktion, die auf diesen Effekten beruht. In einem ersten Schritt zeigen wir, dass der MCD-basierte Ansatz Domänen in Materialien abbilden kann, welche senkrecht zur Ebene (OOP) magnetisiert sind. Als Nächstes verwenden wir die ANE-basierte Detektion, um magnetische Domänen in ferromagnetischen Dünnschichten sowohl in der Ebene als auch senkrecht zur Ebene magnetisiert mit räumlicher Auflösung im Nanometerbereich abzubilden. Das ANE-Signal ist dabei direkt proportional zur Magnetisierung und einem Temperaturgradienten. Für eine aussagekräftige ANE-basierte Bildgebung ist es entscheidend, die Eigenschaften dieses Gradienten zu kennen. Wir leiten die räumliche Verteilung und die Größe des Temperaturgradienten auf der Nanometerskala ab, indem wir eine wohl definierte magnetische Textur untersuchen.

Abschließend wird ein Weyl-Halbmetall auf Manganbasis (Mn_3Sn) untersucht, das eine nichtkollineare AF-Ordnung aufweist. Die hexagonale Kristallstruktur der Verbindung beherbergt eine Kagome-Ebene, auf der Mn-Atome eine inverse dreieckige Spinstruktur bilden. Ein kleines Nettomoment in den Kagome-Ebenen, das an ein äußeres Magnetfeld koppeln kann, ermöglicht das Umschalten der magnetischen Ordnung. Das feldinduzierte Umschalten in Mn_3Sn wird mit räumlich aufgelösten ANE-Messungen bis in den Nanobereich hinein beobachtet. Die beobachteten Ergebnisse werden mit den MOKE-basierten Hysteresemessungen verglichen.

Glossary

Terms	
AF	Antiferromagnet
AFM	Atomic force microscope
AHE	Anomalous Hall effect
AHC	Anomalous Hall conductivity
AMR	Anisotropic magneto resistance
ANE	Anomalous Nernst effect
ANC	Anomalous Nernst conductivity
BZ	Brillouin zone
CMP	Cluster multipole
COP	Cluster octupole
DMI	Dzyaloshinskii–Moriya interaction
FEM	Finite element modelling
FM	Ferromagnet
FWHM	Full width at half maxima
IP	In-plane
HDP	Helicity-dependent photoconductivity
LED	Light emitting diode
LCP	Left circularly polarised
MCD	Magnetic circular dichroism
MCA	Magnetocrystalline anisotropy
MO	Magneto-optical
MOKE	Magneto-optical Kerr effect
MOOP	Magnetic octupole order parameter
MRAM	Magnetoresistive random-access memory
NA	Numerical aperture
NCAF	Non collinear antiferromagnet
NF-SANE	Near-field SANE
PD	Photo diode
PEEM	Photo emission electron microscopy
PMA	Perpendicular magneto anisotropy
PMMA	Polymethyl methacrylate
RCP	Right circularly polarised
SANE	Scanning ANE
SHE	Spin Hall effect
SNR	Signal to noise ratio
SNOM	Scanning near-field optical microscope
SOC	Spin-orbit-coupling
SQUID	Superconducting quantum interference device
OOP	Out-of-plane
VSM	Vibrating sample magnetometery
XMCD	X-ray magnetic circular dichroism
XRD	X-ray diffraction

Contents

Part I

Introduction

Chapter 1

Lead-in

Spin electronics aims to utilize the electron's spin degree of freedom in data storage devices. Doing so may improve storage capacity and the data processing speed beyond the charge-based paradigm of metal-oxide-semiconductor technology [1, 2]. Traditionally, ferromagnets (FMs) are used as key active elements whose magnetic states are employed as bits. The miniaturization of such spintronic devices requires individual magnetic bit units made of FMs to be densely packed. Here, the magnetic stray fields due to interactions between neighboring bits are a major limitation for the packing density [3, 4]. An elegant solution that has been used since the very first spintronic sensors, as well as in magnetic random access memories [5, 6], is a synthetic antiferromagnet [7, 8] formed from thin ferromagnetic layers coupled via a thin metallic antiferromagnetic coupling layer. Recently, there has been increased interest in utilizing innately antiferromagnetic (AF) materials for spintronic applications [4, 9–12], which are free from stray fields.

Using AF materials in spintronic devices offers a number of advantages, including miniaturization of the size of the bits down to the nanoscale [4], fast switching in the THz regime [4, 13], and stability against environmental magnetic perturbations [14]. Being able to switch the antiferromagnetic ordering and read the state electrically or optically brings such devices closer towards technological realization. However, the readout signal associated with the magnetic states of AF is usually not large enough for practical utilization in spintronic devices. While the magnetic state of a ferromagnet can be readily detected by a strong Anomalous Hall effect (AHE) [15] based readout, AFs rely on a much weaker anisotropic magnetoresistance (AMR) based response [4]. Imaging of AF magnetic domains requires cumbersome synchrotron-based X-ray magnetic dichroism techniques [16]. On the other hand, ferromagnetic domains can be easily imaged using magneto-optical Kerr effect (MOKE) based optical microscopes. Alternately, new kinds of AFs are explored, which show large readout signals related to their AF states. Over the last decade, there has been significant development in the field of topological materials [17, 18], including the discovery of chiral antiferromagnets [19–22].

In this dissertation, we discuss manganese-based Weyl semimetals of the type Mn_3X (X=Sn, Ge) that show noncollinear AF (NCAF) ordering. The hexagonal crystal structure of these compounds hosts a Kagome plane on which antiferromagnetically coupled Mn

atoms are arranged on a triangular lattice. The triangular coplanar arrangement of Mn moment on three lattice sites results in a negligible net moment, similar to collinear AFs. The nontrivial topology of their band structure gives a large Berry curvature that acts as a fictitious magnetic field [23]. As a result, they exhibit band structure-driven large magnetotransport and optical responses. The readout signal based on these effects relates to antiferromagnetic ordering. Therefore, it can be used to detect their magnetic state. Thus, they are promising to show the combined advantage of FMs (large readout signal) and AFs (negligible stray field).

Berry curvature-driven optical and magnetotransport responses in NCAFs include anomalous Hall effect [24–29], anomalous Nernst effect (ANE) [30–34], MOKE [35–40], and magnetic circular dichroism (MCD) effect [41, 42]. In order to detect the magnetic state and imaging domain structures of novel topological antiferromagnetic materials, it is imperative to develop measurement techniques based on Berry curvature-driven signals. In this work, such methods based on the MCD and ANE effects are developed. The readout signal based on MCD or ANE can be generated by laser heating. The advantage of laser heating is that it can be locally confined. The resultant readout signal, therefore, relates to the local magnetic state in the region of confined laser heating. Spatially resolved scanning measurements of such readout signals allow for magnetic domain imaging. A laser heating underneath the focal spot of a scanning optical microscope is used to image the magnetic domain with a spatial resolution of the laser beam focal spot size.

The size of the focal spot in the optical microscope is fundamentally limited by the optical diffraction limit of $\lambda/2NA$, where λ is the laser wavelength, and NA is the numerical aperture of the objective lens being used for focusing the laser beam [43, 44]. For typical optical microscopes, this limit is a few hundred nanometers [45]. Generally, it is understood that AFs exhibit domain structures at the sub-micrometer scale [35, 46]. In order to understand their behavior (e.g., their response to magnetic fields and spin torques or interaction with structural defects), imaging of the magnetic order with nanometer resolution is required, as it has been done with X-ray-based photoemission electron microscopy (PEEM) [47–50]. However, PEEM is extremely surface sensitive. To improve the spatial resolution beyond the diffraction-limited laser focal spot size, an enhanced optical near-field scattered from a nanoscale-size object [51, 52] is utilized. This is done by focusing a laser beam on the apex of an atomic force microscope (AFM) tip. The resulting enhanced optical near-field is confined to the apex of the tip, which has a diameter of a few nanometers. Such an optical near-field provides laser heating that is confined to the nanoscale.

In the first step, we demonstrate that laser heating-induced MCD response can be utilized to detect out-of-plane (OOP) magnetization. Here, MCD-driven differential absorption for left- and right-circularly polarized laser beams results in helicity-dependent photoconductivity (HDP). By performing scanning HDP measurements, we image magnetic domains in a well-defined OOP-magnetized wire structure with a sub-micrometer spatial resolution.

Next, we study laser heating-induced temperature gradient that generates an ANE-driven electrical response transverse to the magnetization and the temperature gradient [53]. This allows for deducing both in-plane (IP) and OOP magnetization because the temperature gradient can be generated in and out-of-plane of the sample. Previously, scanning ANE (SANE) measurements have been performed to image IP magnetization with a spatial resolution of a few micrometers [54–57]. Extending the method to the optical near-field improves the spatial resolution to the nanoscale [58–61]. These experiments rely on an ANE signal generated by the laser heating-induced OOP temperature gradient. However, the spatial distribution of such a temperature gradient has not been studied yet, but highly requested for a realistic understanding of SANE imaging. Moreover, the magnetic origin of observed contrast in the magnetic domain structures has not been verified. We perform SANE imaging in IP-magnetized ferromagnetic thin films of CoFeB. To verify the magnetic origin of the observed contrast, the SANE images are compared with those obtained by a standard magnetic imaging method based on the Kerr effect. Since the ANE signal is directly proportional to the temperature gradient, we consider the inverse problem and deduce the temperature distribution by studying a well-known Landau pattern surrounding a magnetic vortex core [62, 63].

The spatial nonuniform intensity distribution of the focused laser beam results in an IP temperature gradient that can be used to probe OOP magnetization [56,61]. Finite element modeling (FEM) simulations of the laser heating indicate that the IP temperature gradient's magnitude is comparable to that of the OOP temperature gradient. Inspired by this result, the optical near-field-based magnetic imaging is extended to visualize magnetic domains in an OOP-magnetized racetrack nanowire. This demonstrates that the method can be utilized to probe magnetization in OOP-magnetized samples with nanoscale spatial resolution.

Finally, the SANE microscopy technique is used to study a thin film of Mn_3Sn that shows NCAF ordering. A magnetic field is applied along the different directions in the Kagome plane of the hexagonal crystal structure. Field-inducing switching of the magnetic ordering is visualized with nanoscale spatial resolution. The switching observed by the ANE method is further verified by the MOKE-based hysteresis measurements.

The thesis is divided into three parts. The first introductory part contains an introduction, scientific background, and methods. The second part is focused on examining different aspects of the two imaging techniques based on opto-electrical responses. This is done by applying the imaging method to ferromagnets whose magnetic properties are well understood. The final part discusses the ANE-based study of a NCAF Mn_3Sn film. These parts are further divided into eight Chapters, for which the outline is as follows:

- Chapter 2: A discussion on the scientific background required to understand NCAFs and Berry curvature-driven optical and magnetotransport effect in NCAFs. Additionally, a brief discussion on various sample preparation techniques is presented.

- Chapter 3: The technical details of the sample preparation, magnetic domain imaging techniques, micro-magnetic, and COMSOL-based finite element modeling simulations.
- Chapter 4: MCD-driven HDP signal is used to probe magnetization in an OOP-magnetized material. Studying a well-defined magnetic structure demonstrates the reliability of the technique for imaging magnetic domain structures in PMA wire structures.
- Chapter 5: A scanning optical microscope is utilized to create a laser heating-induced temperature gradient. The magnitude and spatial distribution of the OOP component of the temperature gradient are discussed. We show the magnetic origin of laser heating-induced ANE signal and perform magnetic domain imaging by performing spatially resolved measurements of such an ANE signal. The dependence of the magnitude of the ANE signal on various measurement geometrical factors is also discussed.
- Chapter 6: ANE-based magnetic domain imaging with an optical near-field is discussed. An enhanced optical-near field underneath a vibrating AFM tip is used to create a nanoscale temperature gradient. This enables magnetic domain imaging with nanoscale spatial resolution.
- Chapter 7: An analysis of the IP component of laser heating-induced temperature gradient is presented. We show the utility of such an IP gradient for the magnetic domain imaging of OOP magnetized material.
- Chapter 8: ANE-based study of Mn_3Sn thin films.

Chapter 2

Scientific background

We discuss various aspects of optical and magnetotransport response in magnetic materials. The goal is to qualitatively understand that Berry curvature associated with the nontrivial topology of the band structure can generate these responses. Two classes of magnetic materials of interest are FMs and NCAFs, whose magnetic properties can be described in terms of magnetic dipole and octupole moments, respectively. In the first Section, magnetic multipoles and different magnetic interactions responsible for the various types of magnetic ordering are discussed. The second Section briefly summarises three different classes of magnetic materials that were previously mentioned in the introduction Section; here, the focus is on NCAFs. In the last two Sections, we discuss the Berry curvature for the band structures and correlate optical and magnetotransport response with it. We also define a magnetic order parameter that drives these responses in NCAFs.

2.1 Magnetism

Magnetism is a class of physical attributes associated with magnetic fields. The magnetic field is generated by moving charged particles, and it can be defined in terms of magnetic multipoles, as we discuss in the next subsection.

2.1.1 Magnetic multipole

A moving electron having a finite current density $\mathbf{j}(\mathbf{r})$ produces a magnetic field ($\mathbf{B}$) that is given by the solution to the following Poisson equation:

$$\nabla^2 \mathbf{A}(\mathbf{r}) = -\frac{4\pi}{c}\mathbf{j}(\mathbf{r}) \tag{2.1}$$

Where $\mathbf{A}(\mathbf{r})$ is the magnetic vector potential so that $\mathbf{B}$ is given by the curl of $\mathbf{A}(\mathbf{r})$: $\mathbf{B} = \nabla \times \mathbf{A}(\mathbf{r})$. Consider a region of volume V that has a nonzero current density given by

$\mathbf{j}(\mathbf{r}')$. We show the solution to equation (2.1) at $\mathbf{r} = r\hat{\mathbf{r}}$ outside the volume V, which is given by the following;

$$\mathbf{A}(\mathbf{r}) = \frac{1}{c}\int_V \frac{\mathbf{j}(\mathbf{r}')\mathrm{d}\mathbf{r}'}{|\mathbf{r}-\mathbf{r}'|} \tag{2.2}$$

Using the multipole expansion of $\frac{1}{|\mathbf{r}-\mathbf{r}'|}$, we can express the vector potential as a sum of a series of multipole potentials as follows:

$$\mathbf{A}(\mathbf{r}) = \frac{1}{c}\sum_{p=0}^{\infty}\sum_{q=-p}^{p}\frac{4\pi}{2p+1}\left(\int_V r'^p \mathbf{j}(\mathbf{r}')Y_{pq}^*(\hat{\mathbf{r}})\mathrm{d}\mathbf{r}'\right)\frac{Y_{pq}(\hat{\mathbf{r}})}{r^{p+1}} \tag{2.3}$$

$$= \sum_{p=0}^{\infty}\sum_{q=-p}^{p}\sqrt{\frac{4\pi}{2p+1}}\mathbf{M}_{pq}\frac{Y_{pq}(\hat{\mathbf{r}})}{r^{p+1}} \tag{2.4}$$

Where $\mathbf{M}_{pq}$ is called the multipole moment of the order p, which is defined by the following:

$$\mathbf{M}_{pq} = \sqrt{\frac{4\pi}{2p+1}}\int_V r'^p \mathbf{j}(\mathbf{r}')Y_{pq}^*(\hat{\mathbf{r}})\mathrm{d}\mathbf{r}' \tag{2.5}$$

We discuss a few orders of the multipole moments that are of interest for understanding magnetism in FMs and NCAFs. The zeroth-order magnetic pole, as described by the equation (2.5) simplifies to $\mathbf{M}_{00} \propto \int_V \mathbf{j}(\mathbf{r}')\mathrm{d}\mathbf{r}' = 0$, since the total current density in a closed volume is zero. This result is famously known as the nonexistence of magnetic mono-poles. The first nonzero order of the multipoles is known as a dipole, 2nd as a quadrupole and 3rd as a magnetic octupole.

2.1.1.1 Magnetic dipole

The electrons in atoms undergo two types of motions: one around the nucleus, called orbital motion, and the second is the electron's spin around its own axis. These motions give rise to magnetic moments that contribute to the magnetic field. The current density associated with such motions is equivalent to a current in a loop. The magnetic field produced by such a loop of current can be described in terms of a magnetic dipole ($\mathbf{m}$), which can be expressed as follows:

$$\mathbf{m} = IA\hat{\mathbf{a}} \tag{2.6}$$

Where I is the current flowing in the loop, A is the area of the loop, and $\hat{\mathbf{a}}$ is a unit vector normal to plane of the loop. The net magnetic moment of an electron is obtained by adding orbital and spin magnetic moments, which are governed by laws of quantum mechanics . The magnetic moment of each electron is added to get net atomic moments. In the majority of cases, the individual moments cancel out so that there is no net moment. Some transition metal atoms possess a net moment on the atomic scale. Microscopically, the magnetic property of a material is characterized by magnetization ($\mathbf{M}$), which is an average of all the atomic moments. The relative orientation of atomic moments deter-

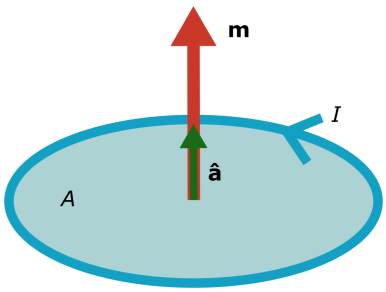

Figure 2.1: Schematic showing magnetic dipole moment of a current-carrying loop.

mines this average net moment, which depends on the type of magnetic interaction in the compound. We briefly discuss a few interactions of interest in the next subsection.

2.1.2 Magnetic interactions

Magnetic interaction refers to the magnetic force between atomic moments. The interaction energy depends on the angle between the net moment at each atom. The orientation of the moments on the neighboring atoms with respect to one another is aligned in a way to minimize the interaction energy.

2.1.2.1 Exchange interaction

The exchange describes inter-atomic Coulomb interaction in quantum mechanics. The intra-atomic exchange governed by the Pauli principle determines the size of the atomic moments. The long-range magnetic order is governed by inter-atomic exchange interaction. While there are many sources for inter-atomic exchange interaction, the results can be simplified in terms of an energy Hamiltonian that was formulated by Heisenberg in 1928; it can be expressed in the following mathematical form:

$$H_{\text{Heisenberg}} = -\lambda_{\text{ex}} \sum_{i \neq j} \mathbf{m}_i \cdot \mathbf{m}_j \tag{2.7}$$

Where λ_{ex} is the exchange constant that quantifies the strength of the interaction, and $\mathbf{m}_i$ is the magnetic moment at the i^{th} atom.

2.1.2.2 Dzyaloshinskii-Moriya interaction

Dzyaloshinskii-Moriya interaction (DMI), also known as the antisymmetric exchange interaction, favors noncollinear alignment of the magnetic moment at the neighboring atoms. This is in contrast to the exchange interaction that favors parallel or anti-parallel alignment of the neighboring moments. The interaction was originally identified by Igor Dzyaloshinskii in 1958 to explain the weak ferromagnetism in an antiferromagnetic iron-oxide crystal. He showed that the weak ferromagnetism results from an antisymmetric exchange originating from the canting of anti-parallelly aligned moments [64]. This antisymmetric exchange was attributed to the relativistic spin-lattice and the magnetic dipole

moment interaction. Two years later, Toru Moriya derived Dzyaloshinskii's antisymmetric exchange interaction by extending Anderson theory of superexchange to include spin-orbit-coupling (SOC). The energy Hamiltonian for the antisymmetric exchange is expressed mathematically by the following equation:

$$H = -\sum_{i \neq j} \mathbf{D}_{ij} \cdot (\mathbf{m}_i \times \mathbf{m}_j) \tag{2.8}$$

Where $\mathbf{D}_{ij}$ indicates the DMI interaction vector between the moments at the i^{th} and j^{th} atoms. Its strength is quantified in terms of the magnitude of the DMI vector (D_{ij}). In the absence of any other interactions, the energy of the Hamiltonian given by equation (2.8) is minimum for the orthogonal alignment of $\mathbf{m}_i$ and $\mathbf{m}_j$. Thus, the DMI favors noncollinear alignments, resulting in canting anti-parallelly aligned antiferromagnets.

2.1.2.3 Magnetocrystalline anisotropy

Magnetic anisotropy describes how the magnetic properties of a material are different in one direction than in another. A special case of it is magnetocrystalline anisotropy (MCA). It indicates that magnetizing the material along a specific direction $\mathbf{k}_i$ is favored due to a decrease of energy by magnetizing along $\mathbf{k}_i$. The corresponding Hamiltonian is given by the following:

$$H = K \sum_i (\mathbf{k}_i \cdot \mathbf{m}_i)^2 \tag{2.9}$$

Where K determines the strength of the anisotropy and $\mathbf{k}_i$ indicates the easy direction for the moments at the i^{th} atom.

2.1.2.4 Zeeman energy

Zeeman energy is the potential energy of a magnetized body in the presence of an applied magnetic field [65]. In terms of the net magnetization ($\mathbf{M}$) and the magnetic field $\mathbf{H}$, the Hamiltonian is given by,

$$H = -\mu_0 \mathbf{M} \cdot \mathbf{H} \tag{2.10}$$

The energy is minimum when the net moment is aligned parallel to the applied field. This provides a handle to control the net magnetization of a material by an external magnetic field.

2.2 Magnetic materials

The type of interactions in the material determines the long-range ordering of the atomic moments. This is reflected in the strength of the material's magnetization. We discuss a few types of magnetic materials in the next subsection.

2.2.1 Ferromagnets

Some transition elements such as Iron (Fe), cobalt (Co), Nickel (Ni), Boron (B) and their alloys, for example, Permalloy ($Fe_{80}Ni_{20}$) and CoFeB ($Co_{60}Fe_{20}B_{20}$) show a strong spontaneous magnetization in the absence of any magnetic field. This spontaneous magnetization results from the long-range ordering of the atomic moments. A major contribution to the energy Hamiltonian for a FM are the exchange and MCA. Therefore, their ordering is determined by minimizing the energy of the following Hamiltonian:

$$H = -\lambda_{\text{ex}} \sum_{i \neq j} \mathbf{m}_i \cdot \mathbf{m}_j + K \sum_i (\mathbf{k}_i \cdot \mathbf{m}_i)^2 \tag{2.11}$$

A positive λ_{ex} favors a parallel alignment of $\mathbf{m}_i$ and $\mathbf{m}_j$; this implies that the moments at each atom are aligned in the same direction. Assuming $\mathbf{k}_i = \mathbf{k}$ to be identical for each atom, all the moments are in one direction determined by $\mathbf{k}$. For PMA materials, the remanent magnetization points out-of-plane of the sample, while it is orientated in the plane of the sample for materials with in-plane anisotropy. Another anisotropy relevant to the discussion in this thesis is the shape anisotropy or magnetic dipole anisotropy [66]. It results from a long-range dipole interaction. As a result, the net contribution is shape-dependent. For rectangular-shaped microscale or nanoscale in-plane magnetized wire structures, the alignment of the magnetization along the wire length is favored. A large spontaneous magnetization in a FM allows its magnetic state to be manipulated by an external magnetic field. This is because the moments align in the direction of the applied field to minimize the Zeeman energy, and in the remanence, they reorient towards the nearest magnetic easy direction.

2.2.2 Collinear antiferromagnets

Similar to FMs, the magnetic ordering in a collinear AF is primarily determined by exchange and MCA interactions as given by the Hamiltonian in equation (2.11). In contrast to FMs, a negative λ_{ex} for an AF favors the anti-parallel alignment of the moments at the neighboring atoms. An AF consists of two equal but oppositely magnetized sub-lattices. This results in zero net magnetization. A related class of magnetic ordering is a ferrimagnet that has two unequal oppositely directed sub-lattices.

2.2.3 Noncollinear antiferromagnets

NCAF materials consist of coplanar, nonlinearly aligned magnetic sublattices. This thesis focuses on NCAFs of the type Mn_3X (X = Sn, Ge). They exhibit a hexagonal crystal structure with space group symmetry P63/mmc (Figure 2.2a). The projection of the structure on a-b plane can be viewed as a triangular arrangement of the Mn atoms forming a Kagome plane (Figure 2.2b). Each plane contains a triangular tube of Mn lattices, each lattice with a magnetic moment of $\approx 3\,\mu_{\text{B}}$ (μ_{B} denotes Bohr magnetron) [67]. The general-

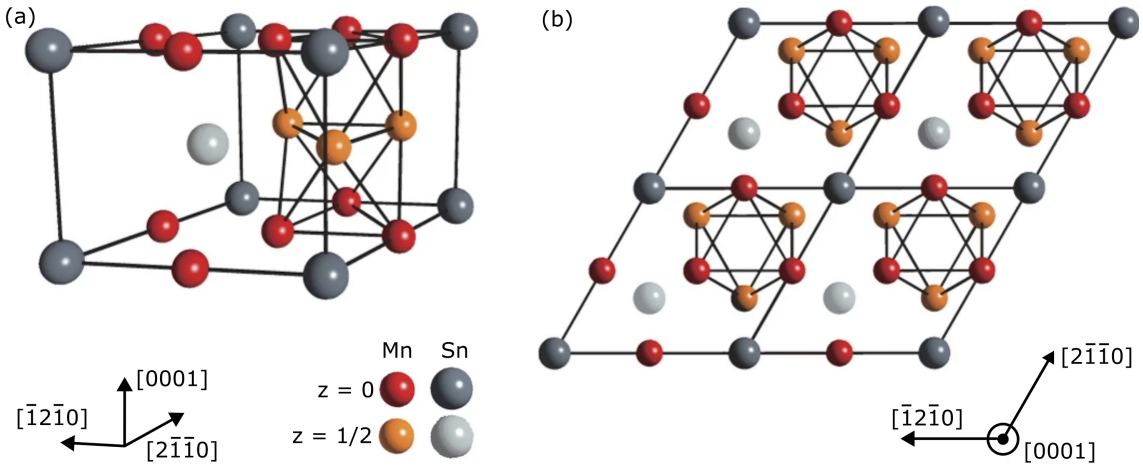

Figure 2.2: (a) A crystallographic unit cell illustrating the crystal structure of Mn_3Sn. Mn and Sn atoms located on two different planes at z=0 and z=1/2 are shown by different colours. (b) A top view of the unit shell showing the arrangement of the Mn atoms in the kagome plane. The figure is adopted from [27].

ized Hamiltonian describing the energy state of Mn_3X is given by the following equation:

$$H = -\lambda_{ex} \sum_{i \neq j} \mathbf{m}_i \cdot \mathbf{m}_j - \sum_{i \neq j} \mathbf{D}_{ij} \cdot (\mathbf{m}_i \times \mathbf{m}_j) + K \sum_i (\mathbf{k}_i \cdot \mathbf{m}_i)^2 \tag{2.12}$$

Similar to collinear antiferromagnets, a negative exchange energy in Mn_3X compounds favors anti-parallel alignment of the Mn moments on adjacent lattices. However, here, we have three Mn lattices. While the moments at the first two lattices can be aligned anti-parallel, an anti-parallel alignment of the moments between the first and third lattices would result in a parallel alignment of the moments between the second and third lattices or vice versa. Thus, the collinear alignment is energetically unfavorable. This problem is resolved by a noncollinear arrangement of Mn moments on the adjacent lattice sites so that they are oriented at an angle of 120° with respect to one another (Figure 2.3a). Such a magnetic ordering is referred to as noncollinear antiferromagnetism.

The DMI interaction determines chirality in a NCAF. Here, the chirality is defined by the sense of rotation of the Mn moment as one hops in a clockwise direction from one Mn lattice site to another. A positive value of the DMI constant $\mathbf{D}_{ij}$ stabilizes an inverse spin triangular structure in Mn_3X below the Néel temperature of $\approx$420 K [67, 68]. This means that hoping clockwise, for example, moving from atom 1 to atom 3 in Figure 2.3b would show 120° rotation of the Mn moment in the counter-clockwise direction (see the right panel in Figure 2.3b). In the absence of any other interactions, the magnetic moments of the Mn atoms form a perfect 120° triangular ordering that would result in a zero net moment. The single-ion-anisotropy, which is very small relative to the other two interactions, leads to a canting of the Mn moments, causing Mn moments to slightly bend in the kagome plane from their ideal 120° orientation (Figure 2.3c). This results in a small net moment of approximately 0.002 μ_B per formula unit in the Kagome plane.

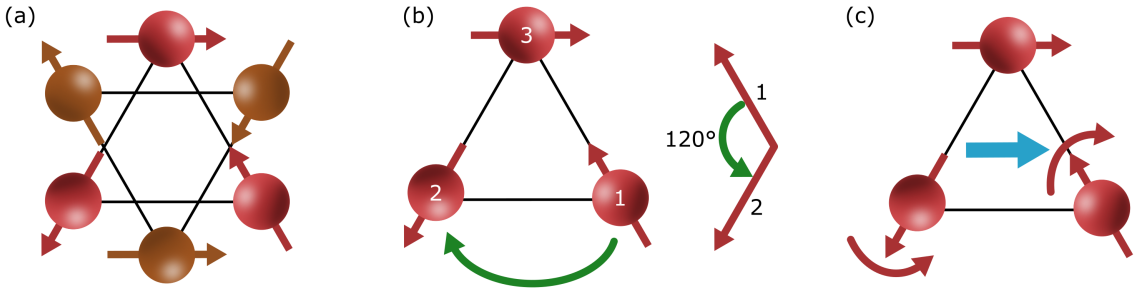

Figure 2.3: (a) Noncollinear alignment of the Mn atom's spin in the kagome plane. (b) Illustration of the inverse triangular spin arrangement. (c) Schematic showing the net moment (blue arrow) resulting from the canting of the Mn atom's spin.

The tiny net moment that can be coupled to an external applied magnetic field provides a handle to control the magnetic ordering. This is because, in the presence of an external field, the Mn moments would coherently rotate to align the net moment in the direction of the applied field (Figure 2.4a). This was shown by polarized-neutron diffraction experiments, where the inverse spin triangular structure of Mn_3X was shown to rotate following the applied magnetic field in the c-plane [68, 69]. In the absence of an external magnetic field, the magnetic ordering is determined by minimizing the energy given by the equation (2.12). It has been shown that the minimal energy state is six-fold degenerate [70] (Figure 2.4b). These six states correspond to the net moment pointing along the six different $\langle \bar{2}\bar{1}10 \rangle$ directions of Mn_3X. Thus, six remanent states are expected for Mn_3X, designated as MS1$\pm$, MS2$\pm$, and MS3$\pm$ (Figure 2.4c). Each such state possesses a net tiny moment lying in the Kagome plane, whose direction varies from one state to another.

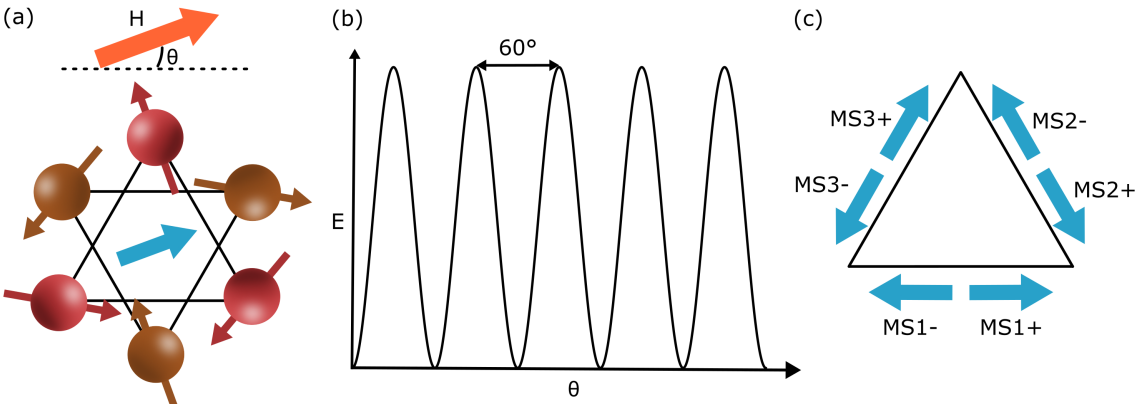

Figure 2.4: (a) Illustration of coherent rotation of Mn sub-lattices spins following an applied magnetic field. (b) The energy profile for the Hamiltonian, as given by equation (2.12) as a function of the angle of the net moment. (c) Direction of the net moment for six energetically degenerate ground states of Mn_3Sn.

2.3 Berry curvature-driven readout in a ferromagnet

Owing to a large stray field, the magnetic state of a ferromagnet can be readily detected by several experimental techniques, such as vibrating sample magnetometry (VSM) [71], and superconducting quantum interference device (SQUID) [72]. These techniques rely on a readout signal that scales with the stray field. Their magnetic domains are easily imaged with Kerr-based optical microscopes. In electrical devices consisting of a FM, the magnetic state can be detected with an electric signal based on magnetotransport response such as ANE and AHE. Some of these responses, such as MOKE, ANE, and AHE, are associated with the band structure. It can be quantified in terms of the Berry curvature of the band structure that acts as a fictitious magnetic field. Since the berry curvature relates to the magnetization, these responses can be used to probe the magnetic state of a material. In the next subsections, we discuss Berry curvature and qualitatively explain the origin of Berry curvature-driven optical and magnetotransport response.

2.3.1 Berry phase and Berry curvature

Berry phase refers to a geometrical phase acquired by the wave function of a quantum object under an adiabatic transformation. Consider a quantum system with a Hamiltonian $H[\mathbf{R}, \mathbf{P}]$. Where $\mathbf{R} = (R^1, R^2, R^3, R^4, ...)$ are the degrees of freedom for the quantum system such as position (x, y, z) and momentum (q_x, q_y, q_z) etc. and $\mathbf{P} = (P^1, P^2, P^3, P^4, ...)$ are the set of external parameters on which the Hamiltonian is dependent. For example, when an electron is placed in a magnetic field ($\mathbf{B}$), its Hamiltonian is $\mathbf{B} \cdot \sigma$, where σ denotes vector Pauli matrices. In this case, the components of the field B_x, B_y, and B_z are such external parameters. We define $(\psi^1(\mathbf{R},\mathbf{P}), \psi^2(\mathbf{R},\mathbf{P}), \psi^3(\mathbf{R},\mathbf{P}), ...)$ to be the Hamiltonian eigenstate with the eigenvalues $(E^1(\mathbf{P}), E^2(\mathbf{P}), E^3(\mathbf{P}), ...)$. We determine how a particular eigenstate $\psi^n(\mathbf{R},\mathbf{P})$ evolves when $\mathbf{P}$ undergoes a periodic adiabatic transformation so that $\mathbf{P}(t=0) = \mathbf{P}(t=T)$. The transformation is considered to be adiabatic if the rate of change of $\mathbf{P}$ is much smaller than $\frac{E^2 - E^1}{\hbar}$. It can be shown that such adiabatic transformation of $\mathbf{P}$ in a close path (C) imparts a phase shift apart from the dynamical phase factor,

$$\psi^n(\mathbf{P}(t=T)) = e^{-\frac{i}{\hbar}\int_0^T dt' E^n(t')} e^{i\gamma^n}(C)\psi^n(\mathbf{P}(t=0)) \tag{2.13}$$

The phase factor $\gamma^n(C)$ is referred to as the Berry phase and is given by the following:

$$\gamma^n(C) = i \oint_C d\mathbf{P}. \langle \psi^n | \nabla_{\mathbf{P}} | \psi^n \rangle \tag{2.14}$$

Here, the integration and the gradient $(\nabla_{\mathbf{P}})$ are performed in parameter space $\mathbf{P}$. The integration is carried out over the closed path C, through which the parameter vector $\mathbf{P}$

is transformed. Therefore, the Berry phase is dependent on C. The path integral in the equation (2.14) can be expressed in surface integral as follows:

$$\begin{aligned}\gamma^n(C) &= i \oint_C d\mathbf{P}.\langle\psi^n|\nabla_{\mathbf{P}}|\psi^n\rangle \\ &= \oint_C d\mathbf{P}.\mathbf{A}^n(\mathbf{P}) \\ &= \iint_{S_C} d\mathbf{S}.\nabla\times\mathbf{A}^n(\mathbf{P}) \\ &= \iint_{S_C} d\mathbf{S}.\Omega^n(\mathbf{P})\end{aligned}$$

Where $\Omega^n(\mathbf{P}) = i\nabla\times\mathbf{A}^n(\mathbf{P}) = i\nabla\times\langle\psi^n|\nabla_{\mathbf{P}}|\psi^n\rangle$ is called the Berry-curvature. It is a vector in the parameter space $\mathbf{P}$. We compute a component of it (Ω^n_{uv}) along the normal to the plane $P_u - P_v$,

$$\begin{aligned}\Omega^n_{uv} &= \delta_{P_u}A^n_v - \delta_{P_v}A^n_u \\ &= i\delta_{P_u}\langle\psi^n|\delta_{P_v}|\psi^n\rangle - i\delta_{P_v}\langle\psi^n|\delta_{P_u}|\psi^n\rangle\end{aligned}$$

The above equation can be solved to present Ω^n_{uv} in the following alternative form:

$$\Omega^n_{uv} = \mathrm{Im}\sum_{m\neq n}\frac{\langle\psi^n|\delta_{P_u}H(\mathbf{P})|\psi^m\rangle\times\langle\psi^m|\delta_{P_v}H(\mathbf{P})|\psi^n\rangle}{(E^n-E^m)^2} \tag{2.15}$$

2.3.2 Anomalous Hall effect

The Hall effect was described by Edwin Hall in 1879 [73]; it describes the transverse resistivity of a nonferromagnetic electric conductor placed in an external magnetic field ($\mathbf{B}$). Due to the Lorentz force acting on the charge carrier, they deflect in the direction transverse to the applied magnetic field and the current direction. This results in a potential difference (voltage signal) that is proportional to the field strength B. In ferromagnetic materials, a transverse voltage signal is observed in the absence of any external magnetic field that relates to the magnetization ($\mathbf{M}$) of the sample. This phenomenon is referred to as the the anomalous Hall effect. Accounting for AHE, the Hall resistivity can be expressed as $\rho^{\mathrm{Hall}}_{xy} = R_0B + R_1M$. Where R_0 and R_1 are ordinary and anomalous Hall coefficients, respectively. It was observed that $R_1 >> R_0$ [74]. Therefore, the AHE can not be explained by the Lorentz force due to the effective magnetization-induced magnetic field. Nevertheless, similar to the ordinary Hall effect, AHE stems from the deflection of the electrons in one direction when a charge current passes through a conducting material. The sources of such deflections are different in different material systems that exhibit AHE. A lot of insight into the source of such deflection in ferromagnets can be gained from a semi-classical transport theory that we describe in the next subsection.

2.3.2.1 Semi-classical transport theory

We discuss a semi-classical theory for the velocity of the electron transverse to an electric field and the magnetization; it helps us to understand the role of the Berry curvature in anomalous Hall conductivity (AHC). The AHE theory pioneered by Karplus and Luttinger in 1954 shows that spin splitting of bands in a ferromagnetic material together with the spin-orbital-coupling (SOC) can give rise to AHC [75]. For an electron in the periodic crystal, the Hamiltonian depends on the wave vector in the momentum space($\mathbf{k}$). As the electron traverses through the periodic lattice potential, its Hamiltonian can be thought of as undergoing adiabatic transformation through a closed path (Brillouin zone) in the momentum space parameters. Thus, it acquires a Berry phase as follows:

$$\gamma^n(\mathbf{k}) = i \oint_{BZ} d\mathbf{k}. \left\langle \psi^{n,k} \right| \nabla_{\mathbf{k}} \left| \psi^{n,k} \right\rangle \tag{2.16}$$

Where $\left|\psi^{n,k}\right\rangle$ is the bloch wave function. The corresponding Berry curvature is,

$$\Omega^n(\mathbf{k}) = i\nabla_{\mathbf{k}} \times \left\langle \psi^{n,k} \right| \nabla_{\mathbf{k}} \left| \psi^{n,k} \right\rangle \tag{2.17}$$

Under the adiabatic transformation of H through $\mathbf{k}$, an electron in an energy band n remains in the state $\left|\psi^{n,k}\right\rangle$. The wave vector $\mathbf{k}$ and position evolve in time according to semi-classical equations of motion [76] as follows:

$$\hbar\dot{\mathbf{k}} = -e(\mathbf{E} + \dot{\mathbf{r}} \times \mathbf{B}) \tag{2.18}$$

$$\hbar\dot{\mathbf{r}} = \nabla_{\mathbf{k}} E^n - \hbar\dot{\mathbf{k}} \times \Omega^n \tag{2.19}$$

For the consideration of AHE, we set $\mathbf{B} = 0$. Substituting equation (2.18) into equation (2.19) gives,

$$\hbar\dot{\mathbf{r}} = \nabla_{\mathbf{k}} E^n - e\mathbf{E} \times \Omega^n \tag{2.20}$$

Equation (2.20) shows that the velocity of the electron ($\dot{\mathbf{r}}$) has a second term dependent on the electric field and the Berry curvature. This term is analogous to the Lorentz force acting on an electron in the presence of an electric field and a magnetic field. Here, the Berry curvature replaces the magnetic field. Thus, the Berry curvature acts as a fictitious magnetic field. It imparts the electron a velocity in the direction transverse to the applied current ($\propto \mathbf{E}$) (see equation (2.20), providing an anomalous Hall conductivity. This simple analysis based on the semi-classical approach shows that the Berry curvature of the band structure gives an intrinsic contribution to AHC. We show this more explicitly with the Kubo formalism in the next subsection.

2.3.2.2 Kubo formula

The Kubo formula describes the linear response of an observable to a time-dependent perturbation [77,78]. Consider an electron in the eigenstate $\left|\psi^{n,\mathbf{k}}\right\rangle$ of the Block Hamiltonian

H. In the absence of any electric field, the average current is zero: $\left\langle \psi^{n,\mathbf{k}} \right| \mathbf{J} \left| \psi^{n,\mathbf{k}} \right\rangle = 0$. Applying a current in x-direction adds a perturbation $\Delta H = -\mathbf{J} \cdot \mathbf{A}$ to H. Where $\mathbf{A} = \delta_t \mathbf{E}$, and $\mathbf{E}$ is the electric field due to the applied current. We determine the effect of ΔH on the current in y-direction $\left\langle \psi^{n,\mathbf{k}} \right| J_y \left| \psi^{n,\mathbf{k}} \right\rangle$. Using the Kubo formula, we can deduce the following [15]:

$$< J_y >= \left\langle \psi^{n,\mathbf{k}} \right| J_y \left| \psi^{n,\mathbf{k}} \right\rangle = e^2\hbar \cdot \mathrm{Im} \sum_{m \neq n} \frac{\left\langle \psi^{n,\mathbf{k}} \right| v_x(\mathbf{k}) \left| \psi^{m,\mathbf{k}} \right\rangle \times \left\langle \psi^{m,\mathbf{k}} \right| v_y(\mathbf{k}) \left| \psi^{n,\mathbf{k}} \right\rangle}{(E^n - E^m)^2} E_x$$

Thus, the Hall conductivity $\sigma_{xy} = \frac{<J_y>}{E_x}$ can be expressed as following:

$$\sigma_{xy} = e^2\hbar \cdot \mathrm{Im} \sum_{m \neq n} \frac{\left\langle \psi^{n,\mathbf{k}} \right| v_x(\mathbf{k}) \left| \psi^{m,\mathbf{k}} \right\rangle \times \left\langle \psi^{m,\mathbf{k}} \right| v_y(\mathbf{k}) \left| \psi^{n,\mathbf{k}} \right\rangle}{(E^n - E^m)^2} \tag{2.21}$$

Where the velocity operator $\mathbf{v}(\mathbf{k})$ is defined by $\mathbf{v}(\mathbf{k}) = \frac{1}{i\hbar}[r, H(\mathbf{k})] = \frac{1}{\hbar}\nabla_{\mathbf{k}} H(\mathbf{k})$. Substituting this into equation (2.21) gives the following:

$$\sigma_{xy} = \frac{e^2}{\hbar} \cdot \mathrm{Im} \sum_{m \neq n} \frac{\left\langle \psi^{n,\mathbf{k}} \right| \nabla_{k_x} H(\mathbf{k}) \left| \psi^{m,\mathbf{k}} \right\rangle \times \left\langle \psi^{m,\mathbf{k}} \right| \nabla_{k_x} H(\mathbf{k}) \left| \psi^{n,\mathbf{k}} \right\rangle}{(E^n - E^m)^2} \tag{2.22}$$

The summation term in equation (2.22) is the same as the Berry curvature (Ω_{k_x,k_y}) given by equation (2.15) in the momentum space $\mathbf{k}$. This simplifies equation (2.21),

$$\sigma_{xy} = \frac{e^2}{\hbar} \Omega_{k_x,k_y} \tag{2.23}$$

Accounting for all the bands n and $\mathbf{k}$ vector, the total contribution to the AHC is given by the following equation:

$$\sigma_{xy} = \frac{e^2}{\hbar} \sum_n \int_{BZ} \frac{d\mathbf{k}}{(2\pi)^3} f(E^{n,\mathbf{k}}) \Omega^n_{k_x,k_y}(\mathbf{k}) \tag{2.24}$$

Where f is energy density function.

2.3.3 Anomalous Nernst effect

The Nernst effect is a thermal analog of the Hall effect. Nernst and Ettingshausen discovered in 1886 that applying a temperature gradient in bismuth transverse to an applied magnetic field gives a voltage in the direction perpendicular to both the field and the gradient [79]. Here, the thermal current due to the temperature gradient works analogously to the applied electrical current in the case of the Hall effect. As discussed in the previous subsection, the materials with a nonzero Berry curvature possess a fictitious magnetic field. Therefore, they exhibit the Nernst effect in the absence of any applied magnetic field [80–85]. This phenomenon is referred to as anomalous Nernst effect. However, the dependence of the anomalous Nernst conductivity (ANC) on the Berry curvature is not

the same as that of AHC [86–88]. The ANC (α_{xy}) is related to AHC by the following equation:

$$\alpha_{xy} = -\frac{1}{e}\int \frac{\partial f}{\partial \mu}\sigma_{xy}(\varepsilon)\frac{\varepsilon-\mu}{T} \tag{2.25}$$

Where $f = \frac{1}{\exp(\frac{\varepsilon-\mu}{k_B T})+1}$ is the Fermi distribution function, and μ is the chemical potential. This shows a nontrivial relation between the two, and the presence of AHC in a material does not imply the same for the ANC. Following the Boltzmann transport theory, a simpler relation arises in the lower temperature regime as follows:

$$\alpha_{xy} = -\frac{\pi^2 k_B^2 T}{3e}\frac{\mathrm{d}\sigma_{xy}}{\mathrm{d}\varepsilon}\bigg|_{\varepsilon=\mu} \tag{2.26}$$

In the low-temperature regime, the ANC is proportional to the derivative of AHC at the Fermi level. Importantly, the equation (2.25) and (2.26) pronounce that ANC depends of the Berry curvature Ω_{k_x,k_y} through the dependence of $\sigma_{x,y}$ on Ω_{k_x,k_y} by equation (2.24). Thus, Ω_{k_x,k_y} has a key role in the anomalous Nernst response.

2.3.4 Magneto-optical effects

The magneto-optical (MO) effects refer to the phenomena in which an electromagnetic wave propagating through a magnetic material is altered [89]. It originates from the differential dielectric permittivity for the left and right circularly polarized lights. Depending upon the measurement geometry and the observable being measured, the phenomena is known in terms of three major MO effects. The rotation of the plane of polarization of the light after transmitting through a magnetic medium is referred to as the Faraday effect [90]. The other two MO effects, which are the subject of discussion in this thesis, are the Kerr and the magnetic circular dichroism effects. In the Kerr effect, the ellipticity and polarization angle of light reflected from a magnetized material are modified. The MCD effect results in a differential absorption of the left-circularly-polarized (LCP) and right-circularly-polarized (RCP) light that relates to the magnetization of the material. Here, we briefly discuss the origin of these MO effects.

The electric displacement vector $\mathbf{D}$ in a magnetic medium relates to the dielectric permeability tensor ($\varepsilon(\mathbf{M})$) and the electric field of the propagating electromagnetic wave as follows:

$$\begin{pmatrix} D_x \\ D_y \\ D_z \end{pmatrix} = \varepsilon_0 \varepsilon(\mathbf{M}).\mathbf{E} = \varepsilon_0 \begin{pmatrix} \varepsilon_{xx} & \varepsilon_{xy} & 0 \\ -\varepsilon_{xy} & \varepsilon_{yy} & 0 \\ 0 & 0 & \varepsilon_{zz} \end{pmatrix} \begin{pmatrix} E_x \\ E_y \\ E_z \end{pmatrix} \tag{2.27}$$

Where ε_0 is the dielectric permeability in a vacuum. We consider a plane electromagnetic wave propagating in z-direction. They are characterized by the following forms of the electric and magnetic fields:

$$\mathbf{E} = (E_x\hat{\mathbf{x}} + E_y\hat{\mathbf{y}})\exp^{i(\mathbf{k}.\mathbf{r}-\omega t)} \tag{2.28}$$

$$\mathbf{H} = \mathbf{H}_0 \exp^{i(\mathbf{k}.\mathbf{r}-\omega t)} \tag{2.29}$$

Solving Maxwell's equations for the above form of $\mathbf{E}$ and $\mathbf{H}$ gives the following relation between the wave propagation vector $\mathbf{k}$ and $\mathbf{E}$:

$$(\mathbf{k}.\mathbf{E})\mathbf{k} - k^2\mathbf{E} + \varepsilon_0\mu_0\omega^2\varepsilon.\mathbf{E} = 0 \tag{2.30}$$

This can be written in the matrix form as follows:

$$\begin{pmatrix} k^2/k_0^2 - \varepsilon_{xx} & -\varepsilon_{xy} & 0 \\ \varepsilon_{xy} & k^2/k_0^2 - \varepsilon_{xx} & 0 \\ 0 & 0 & k^2/k_0^2 - \varepsilon_{zz} \end{pmatrix} \begin{pmatrix} E_x \\ E_y \\ 0 \end{pmatrix} = 0 \tag{2.31}$$

Where $k_0^2 = \varepsilon_0\mu_0\omega^2$ and k is the magnitude of the wave propagation vector $\mathbf{k}$. The normal mode solutions are the nontrivial solution of equation (2.31). They are given by the following equations:

$$k_\pm^2 = k_0^2(\varepsilon_{xx} \pm i\varepsilon_{xy}) \tag{2.32}$$

$$E_y = \pm iE_x \tag{2.33}$$

These two solutions, given by equation (2.33) describe a LCP and RCP light with wave propagation vector given by equation (2.32). In a magnetic material, the off-diagonal component (ε_{xy}) of the dielectric permeability tensor is nonzero. This gives a complex value of $k_\pm$ that results in MO effects.

2.3.4.1 Kerr effect

A linearly polarized light reflected from a magnetized material undergoes rotation of the polarization by an angle θ_K and acquires ellipticity (η_K) due to the Kerr effect. We consider an incident light polarized along the x-direction ($\mathbf{E} = (E_0, 0, 0)$). It can be written as a linear summation of LCP and RCP lights, for which we have already deduced k. Using the Fresnel equation, the reflection coefficient for LCP (r_-) and RCP (r_+)can be calculated as follows:

$$r_\pm = \frac{\frac{k_\pm}{k_0} - 1}{\frac{k_\pm}{k_0} + 1} = \frac{\sqrt{\varepsilon_{xx} \pm i\varepsilon_{xy}} - 1}{\sqrt{\varepsilon_{xx} \pm i\varepsilon_{xy}} + 1} \tag{2.34}$$

The incident $\mathbf{E}_{\text{in}} = E_0\hat{\mathbf{x}}$ can be expressed in terms of a LCP ($\mathbf{E}_-$) and a RCP ($\mathbf{E}_+$) light as follows:

$$\mathbf{E}_{\text{in}} = \frac{E_0\hat{\mathbf{x}} + iE_0\hat{\mathbf{y}}}{2} + \frac{E_0\hat{\mathbf{x}} - iE_0\hat{\mathbf{y}}}{2} = \mathbf{E}_- + \mathbf{E}_+ \tag{2.35}$$

The reflected light is described by $\mathbf{E}_{\text{ref}}$,

$$\mathbf{E}_{\text{ref}} = r_-\mathbf{E}_- + r_+\mathbf{E}_+ = \frac{r_+ + r_-}{2}E_0\hat{\mathbf{x}} - i\frac{r_+ - r_-}{2}E_0\hat{\mathbf{y}} \tag{2.36}$$

The polarization of the reflected light is rotated by a complex angle $\phi_K = i\frac{r_+ - r_-}{r_+ + r_-}$, implying an elliptical polarization. θ_K specifies the angle of the ellipse's major axis with respect to

$\mathbf{E}_{\text{in}}$, and the ellipticity η_{K} is defined as the ratio of ellipse's major and minor axes. They can be calculated in terms of ε_{xy} as follows:

$$\theta_{\text{K}} = -\text{Im}\frac{k_+k_0 - k_-k_0}{k_+k_- - k_0^2} \tag{2.37}$$

$$\eta_{\text{K}} = \text{Re}\frac{k_+k_0 - k_-k_0}{k_+k_- - k_0^2} \tag{2.38}$$

They are dependent on ε_{xy} through the dependence of $k_\pm$ on ε_{xy} given by equation (2.32).

2.3.4.2 Magnetic circular dichroism

The intensity of light is attenuated due to absorption as it traverses through a magnetic material. Due to the difference in wave propagation vector amplitude k_+ and k_- for RCP and LCP lights, they are attenuated to a different extent. Thus, the absorption is different for RCP and LCP lights. This difference depends on $k_+ - k_-$ that relates to ε_{xy}.

2.3.4.3 Magneto-optical conductivity

Similar to AHC, Magneto-optical conductivity can be expressed in terms of the band structure properties using the Kubo formula. It is given by the following equation [91,92]:

$$\sigma_{xy}^{\text{MO}} = \hbar e^2 \int_{BZ} \frac{d\mathbf{k}}{(2\pi)^3} \sum_{m\neq n} (f^{n,\mathbf{k}} - f^{m,\mathbf{k}}) \times \text{Im}\frac{\left\langle \psi^{n,\mathbf{k}} \right| \nabla_{k_x} H(\mathbf{k}) \left| \psi^{m,\mathbf{k}} \right\rangle \times \left\langle \psi^{m,\mathbf{k}} \right| \nabla_{k_x} H(\mathbf{k}) \left| \psi^{n,\mathbf{k}} \right\rangle}{(E^n - E^m)^2 - (\hbar\omega + i\eta)^2} \tag{2.39}$$

Where f is the Fermi distribution, andη is an adjustable smearing parameter. The complex Kerr rotation angle for a normal Polar Kerr geometry relates to σ_{xy}^{MO} as follows:

$$\theta_{\text{K}} + i\eta_{\text{K}} = -\frac{\sigma_{xy}^{\text{MO}}}{\sigma_{xx}^{\text{MO}}\sqrt{1 + i(4\pi/\omega)\sigma_{xx}^{\text{MO}}}} \tag{2.40}$$

This shows that the Kerr response relates to the band structure. Therefore, a large MOKE response can be expected from the magnetic materials with a nontrivial topology of the band structure.

2.4 Electrical and optical readout in noncollinear antiferromagnets

The tiny net moment in a NCAF results in small readout signals in stray field-based measurement techniques such as VSM and SQUID. The magnetic states of NCAF are probed by large optical and magnetotransport responses generated by the off-diagonal component of the Berry curvature associated with the nontrivial topology of their band structure. Unlike FMs, the magnitude of large optical and magnetotransport responses in NCAFs is not justified by their tiny net magnetization. Instead, these responses emerge from the Berry curvature that relates to their AF ordering. Similar to FMs, where the net magnetization

is a macroscopic parameter, we find an equivalent parameter describing the optical and magnetotransport properties of NCAFs.

2.4.1 Cluster multipole moments

The inverse triangular arrangement of the spin texture in Mn_3Sn is regarded as a ferroic order consisting of clusters of magnetic octupole moments. Mn_3Sn contains two clusters of Mn atoms that determine its magnetic properties. In terms of magnetic dipole moment at the i^{th} sub-lattice ($\mathbf{m}^i$), p^{th} order multipole given by equation (2.5) can be expressed as follows:

$$\mathbf{M}^i_{pq} = \sqrt{\frac{4\pi}{2p+1}}\mathbf{m}^i \cdot \nabla_i (r_i^p Y^*_{pq}(\hat{\mathbf{r}}_i)). \tag{2.41}$$

For the octupole moments, $p = 3$ and $q = \{-3,-2,-1,0,1,2,3\}$. The total contribution of each sub-lattice to the μ^{th} cluster octupole moment (COM) is given by summing the contribution from all the sub-lattices in the cluster (Figure 2.5),

$$\mathbf{M}^{\mu}_{3q} = \sum_{i=1}^{6} \mathbf{M}^i_{3q} \tag{2.42}$$

The macroscopic contribution of the cluster octupole moment ($\mathbf{M}_{3q}$) is defined by summing the contribution from both clusters (Figure 2.5),

$$\mathbf{M}_{3q} = \frac{1}{2V}\sum_{\mu=1}^{2} \mathbf{M}^{\mu}_{\mathbf{3q}} \tag{2.43}$$

Assuming the Mn moments to be identical at each sub-lattice, the magnitude of the COM is shown to be proportional to the moment of the Mn atoms [93]. For Mn moment of $3\mu_B$, its magnitude is $\approx 25\mathring{A}^2\mu_B$ [93].

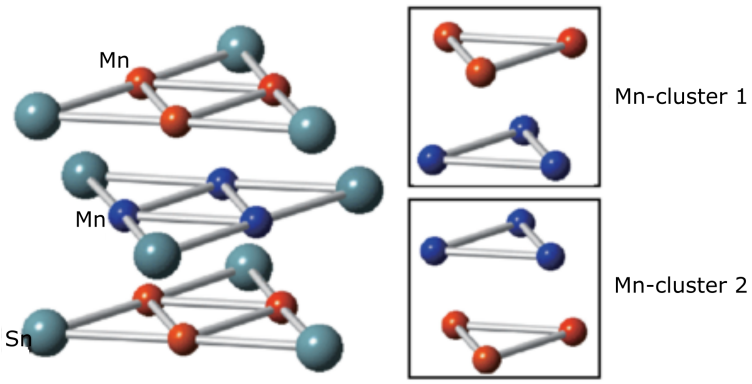

Figure 2.5: Clusters of magnetic atoms that contribute to the magnetic octupole moment. The figure is adopted from [93].

2.4.2 Magnetic octupole order parameter

Optical and magnetotransport responses of a NCAF are dependent on the magnitude and direction of COM ($\mathbf{M}_{3q}$) as defined in the previous subsection. For Mn_3Sn with COM magnitude of $\approx 25 \mathring{A}^2 \mu_B$, AHC is theoretically predicted to be 200 S/cm, which is comparable to the AHC of the bcc Fe [93]. Moreover, the irreducible magnetic space group for MS1+ with the net moment pointing along $+\hat{\mathbf{x}}$ is the same as that for a FM with the magnetization pointing along $+\hat{\mathbf{x}}$ [93]. Therefore, their optical and magnetotransport responses are expected to be identical to that of a FM magnetized along $+\hat{\mathbf{x}}$. Based on these, we define a magnetic octupole order parameter (MOOP) for NCAFs. We denote it by the same symbol, $\mathbf{M}$, as that of magnetization. Its direction is the same as that of the net moment. However, its magnitude is to be calculated using equation (2.43).

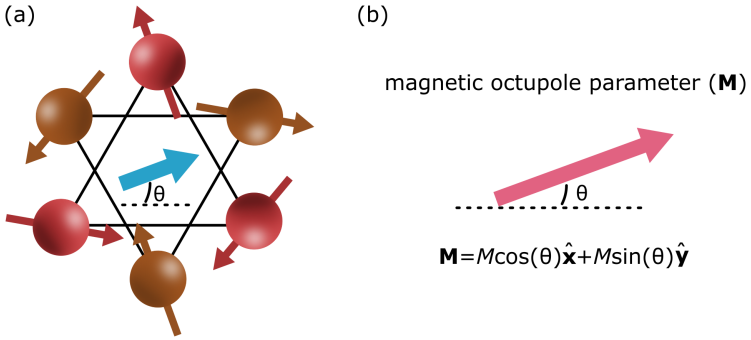

Figure 2.6: Magnetic octupole order parameter for NCAFs.

Chapter 3

Methods

This Chapter discusses details of the sample preparation, opto-electrical measurement setups, and simulations. As highlighted in the introductory Chapter 1, the thesis aims to develop opto-electrical methods to visualize the magnetic states of chiral antiferromagnets; emphasis has been placed on these measurement methods. Standard FM and NCAF materials are used for which the growth conditions had previously been optimized. Therefore, only a brief discussion about sample preparation and device fabrication is provided. The first two Sections briefly mention thin film deposition parameters and device fabrication details. The third Section is devoted to the technical details of the opto-electrical measurements that rely on laser heating. In the next Section, we discuss the model for heating produced by the absorption of the laser beam and the technical details of the COMSOL simulations for laser heating. The last two Sections contain brief details of micromagnetic simulations and XRD measurements.

3.1 Film deposition

All the thin films utilized for the measurements in this thesis were deposited using the dc-magnetron sputtering technique. This is a widely used deposition technique for research and industrial use due to its flexibility, speed, and efficiency in depositing multilayer films. The deposition procedure involves removing atoms from a target material, a 1 to 3-inch wide round disc structure made of elemental metals or alloys. The atom removal is done by bombarding the target with the ions of a working gas (usually Ar). Ionization of the gas is achieved by applying a d.c. voltage between the anode at the substrate and the cathode at the target. A magnetron-based source consisting of several permanent magnets placed behind the target helps to trap the Ar ion close to the target. The deposition chamber is evacuated to an ultrahigh vacuum at a base pressure on the order of 1×10^{-9} mbar before the deposition to remove the contamination from the chamber. Subsequently, Ar gas is released into the chamber using a mass flow controller; this increases the chamber pressure to the process Ar gas pressure on the order of 1×10^{-3} mbar. In the presence of the flowing Ar gas, a d.c. voltage between the cathode and the anode generates the

plasma that injects the film particulate from the target to the substrate. A schematic of this process is shown in Figure 3.1.

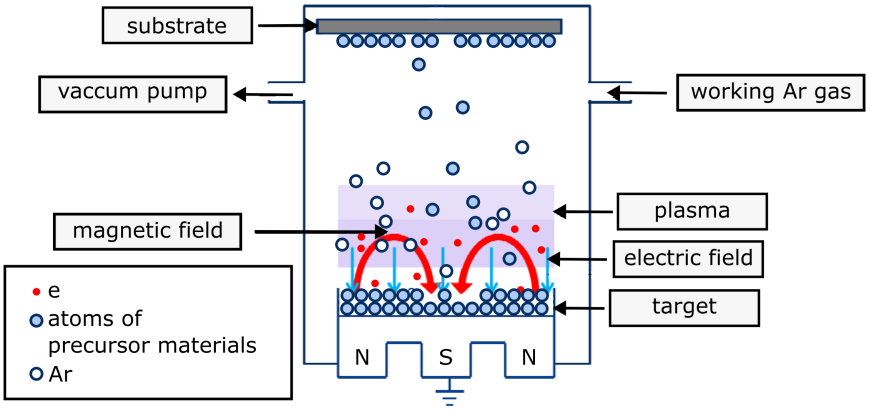

Figure 3.1: Schematic illustration of the magnetron sputtering process adopted from [94].

The deposition of the films used in the thesis was performed by four different people and three different home-made deposition systems were utilized. Ferromagnetic films with perpendicular magnetic anisotropy (PMA) were deposited at the Max Planck Institute of Microstructure Physics (MPI), Halle, using a Multi-source Atomic engineered Next Generation allOys and compounds (MANGO) system. Dr Binoy Krishna Hazra deposited the film used for the HDP measurements, and Dr Jiho Yoon made the PMA sample for the racetrack nanowire. I deposited the IP-magnetized films of CoFeB at Martin Luther University, Halle. We obtained the noncollinear antiferromagnet film of Mn_3Sn from MPI for Chemical Physics of Solids, Dresden. This sample was prepared by Dr Edouard Lesne and followed a recipe similar to the sample discussed in reference [55]. An additional Mn_3Sn sample discussed in Appendix B2 was deposited in the MANGO system by Prajwal Rigvedi at MPI, Halle. The samples are assigned an ID, as listed in Table 3.1.

Table 3.1: Sample IDs for the different kinds of prepared samples

Sample ID	Used for	Substrate	Layer structure	Capping layer
PMA1	HDP measurements in Chapter 4	MgO (001)	Pt/Co/Ni/Co (30/3/7/3 Å)	TaN (3 nm)
CoFeB	ANE measurements in Chapters 5&6	MgO (001)	$Co_{60}Fe_{20}B_{20}$	Au (2 nm)
PMA2	ANE measurements in Chapter 7	Al_2O_3 (001)	TaN/Pt/$(Co/Ni/Co)_3$Co (50/12/(3/7/2)/2 Å)	TaN (3 nm)
NCAF1	Studying a NCAF in Chapter 8	MgO (111)	Ru/Mn_3Sn (3/60 nm)	Si (5 nm)
NCAF2	Appendix B	Al_2O_3 (001)	Ru/Mn_3Sn/MgO (4/60/3 nm)	TaN (3 nm)

The deposition parameters of the films are mentioned in Table 3.2.

Table 3.2: Deposition parameters of the sputter-deposited thin films

Sample ID	**Layer**	**Deposition rate (Å/s)**	**Deposition temperature (°C)**	**Annealing temperature (°C)**	**Process Ar gas pressure (10^{-3} mbar)**	**Base pressure (10^{-9} mbar)**
PMA1	Pt	0.82	room temperature (RT)	NA	3	1
PMA1	Co	0.21	RT	NA	3	1
PMA1	Ni	0.22	RT	NA	3	1
PMA1	TaN	0.17	RT	NA	3	1
PMA2	Pt	0.75	RT	NA	3	3
PMA2	Co	0.25	RT	NA	3	3
PMA2	Ni	0.3	RT	NA	3	3
PMA2	TaN	0.2	RT	NA	3	3
CoFeB	CoFeB	0.1	RT	NA	4.5	30
CoFeB	Au	0.3	RT	NA	4.5	30
NCAF1	Ru	0.32	500	430	4	4
NCAF1	Mn_3Sn	0.68	RT	430	4	4
NCAF1	Si	0.1	RT	430	4	4
NCAF2	Ru	0.2	500	430	3	1
NCAF2	Mn_3Sn	0.3	RT	430	3	1
NCAF2	TaN	0.16	RT	430	3	1

3.2 Device fabrication

The sputter-deposited thin films were shaped into device structures by lithography in combination with the lift-off or dry etching processes. The device structures were defined using a resist that was exposed to either an electron beam (E-beam) or an UV light beam in a scanning fashion. The choice was made based on the length of the smallest feature in the device structure. The smallest feature writable by the focused UV laser beam is limited by its spot size, which is given by the Rayleigh criteria ($0.61\frac{\lambda}{\beta}$) [95]. Where $\lambda = 375\,\text{nm}$ is the wavelength of the UV laser beam, and β is the semi-angle of light collected by the lens. Typically, $\beta \approx 0.5$ so that the spot size is on the order of 500 nm. Technical limitations further increase the smallest writable feature to 2.5 times the Rayleigh criteria limit ($\approx$1 µm). We used a UV laser beam to write the structures larger than one micrometer. For the smaller structures, we used an E-beam that has a smaller spot size due to the smaller wavelength.

A thin film (a few hundred nanometers) of polymethyl methacrylate (PMMA) based positive resist was coated on the substrate for the lift-off process. Here, the positive resist infers that a developer can not dissolve it. Exposing the resist in the region of interest to an E-beam or an UV laser beam alters the chemical properties of the resist in the exposed region. This allows the selective removal of the resist from the exposed area by washing the sample in the developer. Subsequently, the film of magnetic materials is deposited by sputtering. The film sticks directly to the substrate in the exposed regions with no resist.

In the unexposed regions, the film is deposited on the resist. Post deposition, washing the substrate with acetone removes the film together with the resist so that the film of the magnetic materials is left only in the exposed region.

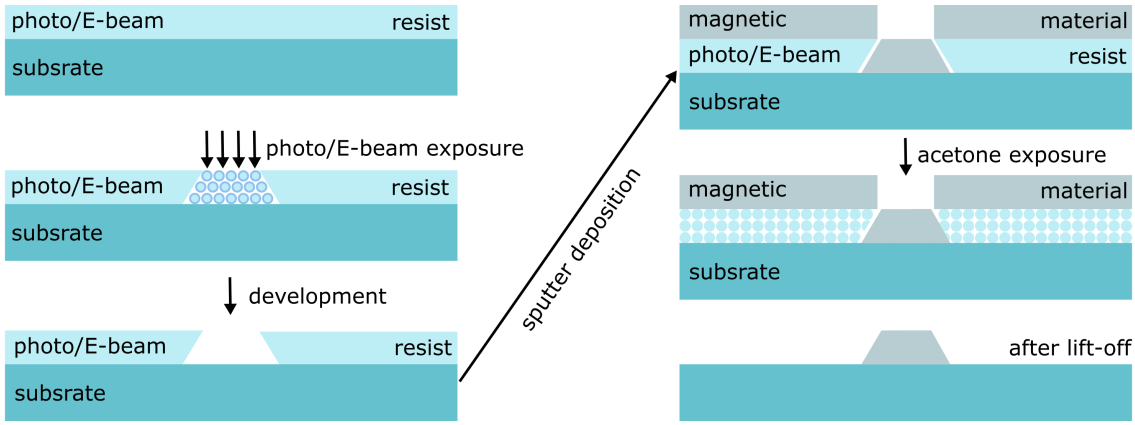

Figure 3.2: Schematic showing major steps involved for the device fabrication by the lift-off process.

For the etching process, we first deposit the film of magnetic materials by sputtering and then coat it with a negative resist. Negative resist implies that it can be dissolved by the developer. Here also, the region of interest is exposed to an E-beam or an UV laser beam. The change in the chemical property in the exposed region doesn't let it get dissolved by the developer. This allows the selective retention of the resist in the exposed region. Subsequently, the film is bombarded by Ar plasma for the ion milling etching procedure. This process removes the magnetic material in all areas except the exposed region, which the resist protects. After the etching procedure, we wash the sample with acetone that removes the resist, and we are left with the magnetic materials in the exposed region.

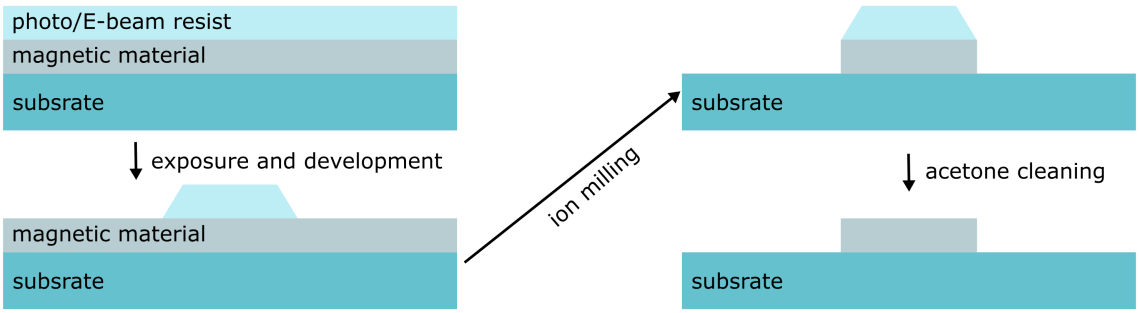

Figure 3.3: Illustration of the device fabrication following the etching process.

All the devices consisting of PMA ferromagnetic films were prepared by an E-beam lithography and etching procedure. Dr Saban Tripancy at Martin Luther University, Halle fabricated the sample for HDP measurements (PMA1), and the PMA sample for the ANE measurements (PMA2) was fabricated by Dr Jiho Yoon at MPI, Halle. The CoFeB device structures were made using lithography and lift-off processes. The devices containing smaller structures ($< 1\,\mu m$) were defined by an E-beam lithography by me at Martin

Luther University, Halle, and devices with larger structures were made by Jitul Deka at MPI, Halle by the means of an UV laser beam. All the Mn_3Sn devices were patterned using lithography and etching procedures. Jitul Deka prepared larger devices with an UV laser beam, and Dr Jiho Yoon utilized an E-beam for the nanowires.

3.3 Opto-electrical measurements

This Section discusses experimental setups built for carrying out magnetic domain imaging measurements. We measure Berry curvature-driven optical or magnetotransport signal in response to laser-induced heating. The technical aspects of the two methods relying on HDP and ANE signals are described here. The scientific background of these signals and the exemplary measurements are discussed in Chapters 4-8.

3.3.1 Helicity-dependent photoconductivity

First, we discuss the method based on an optical signal for imaging magnetic domain structure. Specifically, we chose the MCD effect, which refers to a differential absorption for LCP and RCP lights. To measure such a signal, we illuminate the sample with a circularly polarized laser beam whose helicity is modulated. The differential absorption is measured electrically in terms of a HDP voltage. Thus, the magnetic domain imaging based on HDP measurements discussed in Chapter 4 requires a helicity-modulated circularly polarized laser beam. For this, a linear polarizer and a photo-elastic modulator (PEM) have been used to modulate the polarisation of a laser beam with a wavelength of 532 nm. We briefly discuss the PEM in the next subsection.

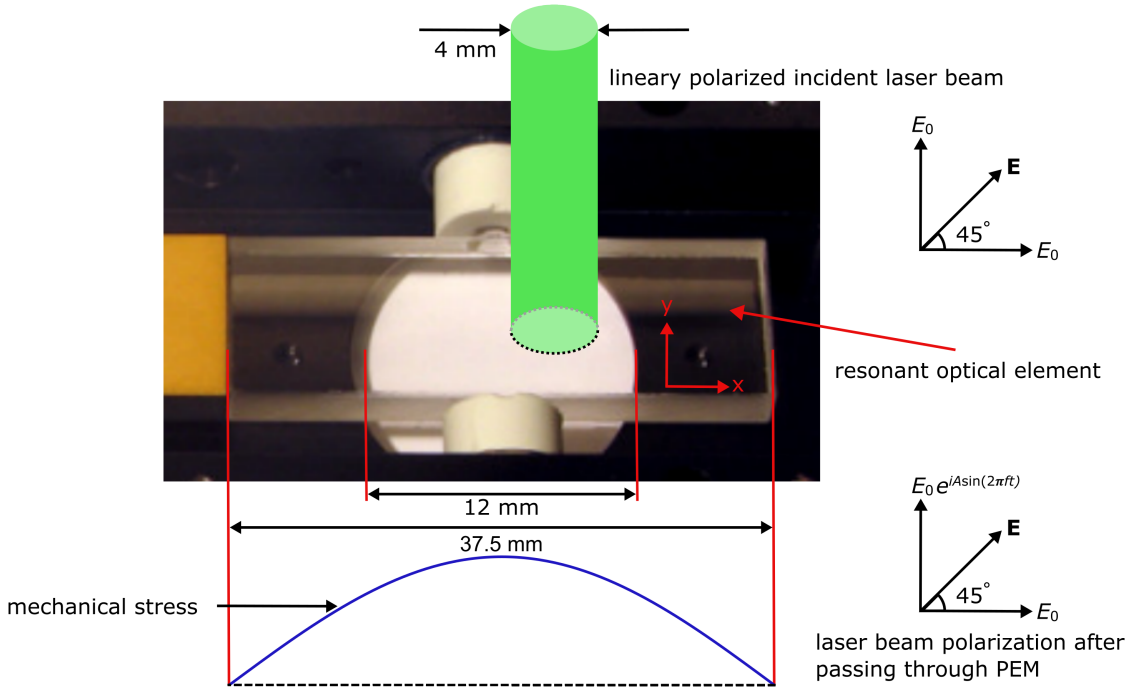

Figure 3.4: The optical head of the PEM is illuminated with a linearly polarized laser beam. After passing through the PEM, the phase of the x-component of the electric field is retarded by an amplitude A.

3.3.1.1 Photo-elastic modulator

We employ a commercially available PEM from Hinds Instruments Inc. (model number: E-310-c). The device consists of a rectangular slab of a resonant optical element with a natural oscillation frequency of $f = 50\,\text{kHz}$ (Figure 3.4). A transducer is attached to the optical element that causes vibration through stretching and compression. The resulting strain leads to birefringence due to the photo-elastic effect [96]. Meaning that the phase of the electric field along the PEM axis (here, x-axis) is retarded by an amplitude of A, which is modulated at the PEM vibration frequency $f = 50\,\text{kHz}$. A retardation amplitude of $A = 90°$ converts incident linearly polarized (at 45° with respect to the PEM axis) light into a circularly polarized state. Modulation of the retardation amplitude between $-90°$ and 90° results in polarisation modulation between the LCP and RCP states. We note that the standing wave generated for the vibration provides spatially nonuniform strain across the length of the PEM optical element due to the sinusoidal profile of the wave. Thus, the retardation amplitude also varies across the PEM axis. We use $\approx$10 mm wide center region, where the amplitude is maximum and the variation is small (see Figure 3.4).

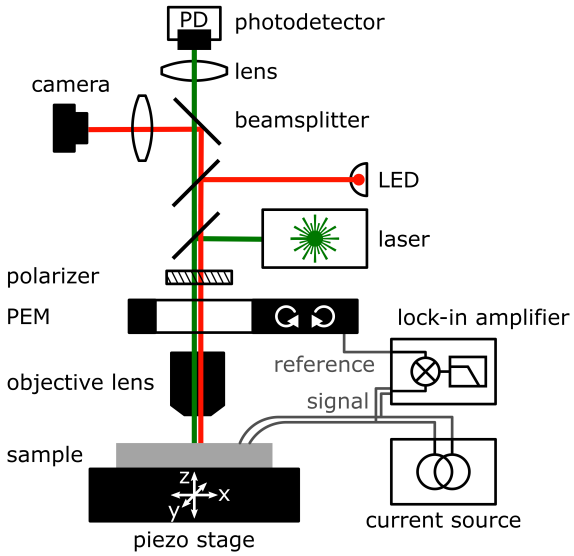

Figure 3.5: Schematic representation of the setup utilized for the spatially resolved HDP measurements. The figure is adopted from the original graphics created by Chris Koerner for our publication [97].

3.3.1.2 Scanning HDP measurement setup

HDP setup consists of a helicity-modulated laser beam, as described above. We use a laser source from Laser Quantum (Torus 532) that could generate a laser beam with a wavelength of 532 nm and with a power of up to 1 W. After passing through the PEM, the laser beam is focused on the sample using an objective lens from Nikon with a numerical aperture 0.7 (60×). The sample is mounted on a piezo stage that allows it to be scanned underneath the laser beam focal spot. For the scanning measurements shown in Chapter 4, the scan was performed in a step size of 150 nm, which is much smaller than the

laser beam focal spot size (≈700 nm, see Chapter 5). In a scanning measurement like here, a step size smaller than the probe size ensures that all the points in the measured region are probed. Using a current source from Keithley (model: 2401), a current is applied (in constant current mode) to measure the helicity-dependent resistance of the sample (by measuring the voltage). The measured voltage is demodulated at the helicity modulation frequency of 50 kHz using a MFLI lock-in amplifier from Zurich Instruments. A time constant of 300 ms and fourth order filter was used. A higher order filter and a larger time constant help to reduce electrical noise, which was ≈50 nV at 50 kHz. The integration time of each measurement was ≈5 seconds, and the average HDP signal was considered. The sample was illuminated with a light-emitting diode (LED) light source, and the reflected light captured through a camera allowed us to visualize the sample and the position of the laser focal spot on the sample. The intensity of the reflected laser beam was measured with a photodetector (PD). The majority of the work for the construction of this setup was done by Palvan Seyidov, who utilized it to investigate the HDP edge signals [97].

3.3.2 Scanning ANE microscopy

Here, we describe the method based on a magnetotransport response. We use an ANE signal that is generated by laser heating-induced heat gradient. Thus, magnetic domain imaging with spatially resolved scanning ANE (SANE) measurements requires a focused laser beam. This was achieved by slightly modifying the HDP setup discussed in the previous subsection. PEM was removed from the path of the laser beam since the polarisation modulation is not required for the ANE measurement (Figure 3.6). The focused laser

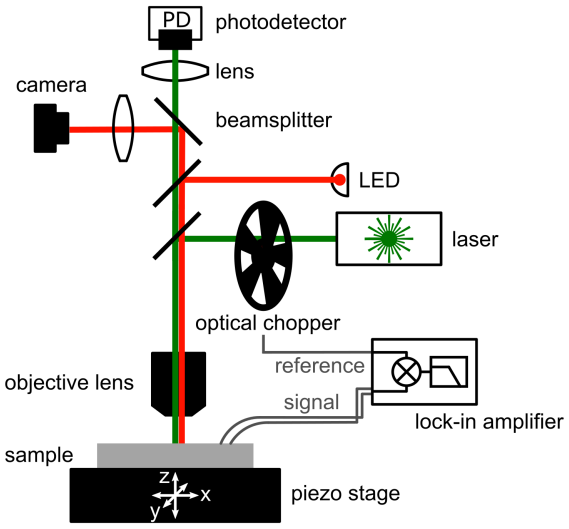

Figure 3.6: Schematic representation of the SANE microscope setup.

beam is partially absorbed, creating a temperature gradient in the sample. This temperature gradient generates an ANE-induced voltage signal. Therefore, no current source is required to generate the ANE voltage. However, to measure the small ANE signal on the order of 1 µV, a lock-in detection technique is used. For this, the intensity of the incident

laser beam is modulated at a frequency of 600 Hz using an optical chopper from Thorlabs (model: MC2000B-EC). Consequently, the laser heating generated ANE-induced signal is also modulated at the same frequency. The ANE signal is measured by demodulating the resulting voltage at 600 Hz using the MFLI lock-in amplifier. Here also, a time constant of 300 ms and fourth order filter was used. The electrical noise is frequency dependent; at 600 Hz, the noise was 100 nV for this set of the lock-in parameters. This gives a signal-to-noise ratio (SNR) of 10 for an ANE signal of 1 µV.

A home-made electromagnet was used that could provide a magnetic field of up to 900 mT during the SANE measurements. A current of up to 10 A was applied to the magnet in the constant current mode using a power supply from Kepco Inc. Since the magnetic field is proportional to the current in the coil, a constant current is required for a stable magnetic field. The operation in constant voltage mode leads to current fluctuation due to the heating of the magnetic coil, which changes its resistance. As a result, the magnitude of the magnetic field fluctuates in the constant voltage mode. Specially designed magnetic pole pieces were utilized that could concentrate the magnetic field near the objective lens (Figure 3.7a). This was required because the working distance for the high *NA* objective lenses is fairly low (≈1 mm in our case). In order to perform such a scan at an elevated temperature, a resistive heater was embedded inside a home-made sample holder. This allowed for SANE measurements at up to 135 °C. The temperature could be controlled by controlling the flowing current in the resistive coil. A calibration between the sample temperature and the current was performed by sticking a temperature sensor at the place of the sample. The sample mounted on a chip carrier was clamped to the sample holder (Figure 3.7b). The electrical contact with the chip carrier was made through the metallic pins underneath the chip carrier.

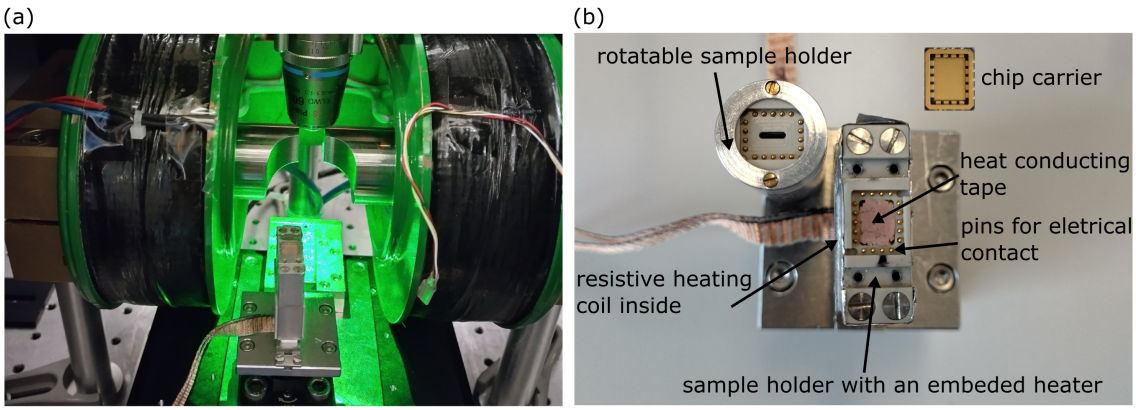

Figure 3.7: (a) Experimental setup for SANE microscopy. (b) Sample holders utilized for SANE measurements.

3.3.3 Near-field scanning ANE microscopy

To perform scanning ANE measurements using optical near-field (NF-SANE), we employ a commercial scanning near-field optical microscope (SNOM) from Neaspec. We briefly discuss the SNOM method in the next subsection.

3.3.3.1 Scanning near-field optical microscope

SNOM utilizes optical near-field to probe the optical properties of a sample. The near-field of a laser beam refers to the evanescent waves in the vicinity of a scattering source. Since the intensity of such an evanescent field decays exponentially within a few nanometers, the sample must be kept in close proximity to the scattering source. In practice, this is done by focusing a laser beam on the sample underneath the tip of an atomic force microscope (AFM) (Figure 3.8). The near-field of the laser beam scattered from the apex of the tip works as an optical probe. The intensity of such a near-field being reflected from the sample is measured, which allows the absorption and reflection properties of the sample to be mapped. A mechanical detector monitoring the height of the tip apex provides information about the sample topography. Since both the intensity of the reflected near-field laser beam and the topography are measured simultaneously, the obtained map of the sample's optical properties can be compared with its topographical structure.

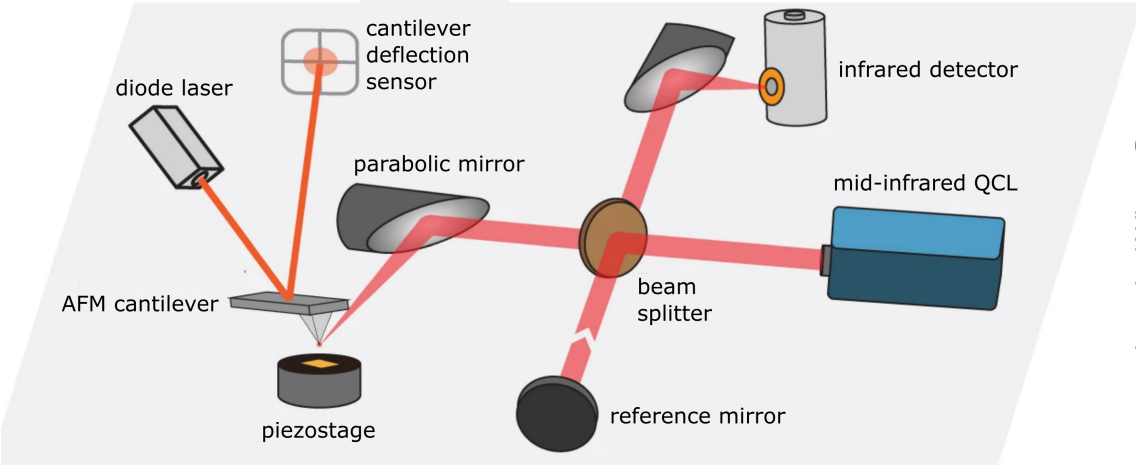

Figure 3.8: Schematic of the experimental setup for the scanning near-field optical microscope. The figure is adopted from [98].

3.3.3.2 NF-SANE with SNOM

We utilized the SNOM discussed in the previous subsection to perform NF-SANE measurements. For this, the films of magnetic materials were patterned into device structures consisting of nanometer/micrometer-wide wire structures. A top view of the SNOM tip in approach with the device structure is shown in Figure 3.9. A laser beam with a wavelength of 8 µm and a power of 25 mW is focused at the tip apex that lies underneath the tip cantilever. For this, we used a QCL laser from Thorlabs (model ITC4002QCL). The optical near-field underneath the tip apex was used to heat the wire locally. The ANE signal generated by this heat gradient is measured electrically through the bonding wires bonded to the contact pads. In order for the AFM tip to be able to approach the micro/nano wire, it is crucial to maintain a sufficiently large gap between the tip and bonding wires (see Figure 3.9). As the bonding wires move away from the pads to the sample holder, they are

lifted in height and collide with the mounting base of the tip. This collision prevents the tip from approaching the sample. To avoid such collisions, the bonding wires are directed in the direction opposite to the tip cantilever (Figure 3.9). The samples were mounted on

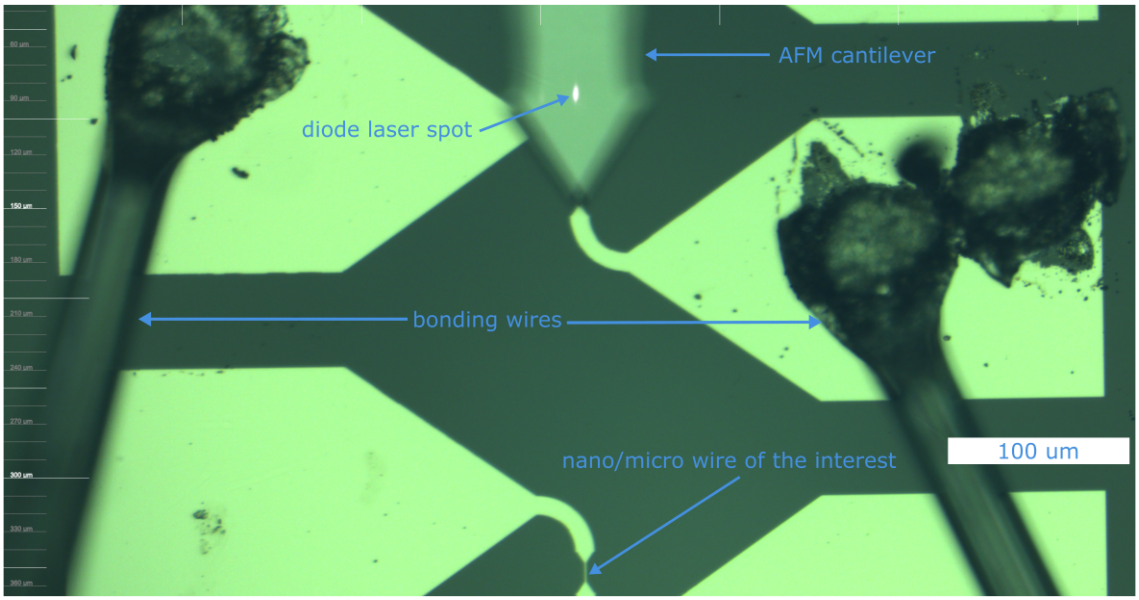

Figure 3.9: A top view of the SNOM tip in contact with the sample utilized for NF-SANE scans.

two different kinds of home-made sample holders. Bonding wires were attached to the larger contact pads on these sample holders (Figure 3.10). The first set of sample holders consisted of a magnetic coil wrapped to iron bars near the sample. This could provide a small IP magnetic field of up to 10 mT during the NF-SANE scans (Figure 3.10a). This set of sample holders was used for the scans requiring a magnetic field during the measurements. The second set of sample holders consisted of a small removable chip carrier to which the samples were mounted (Figure 3.10b). The samples mounted on these chip carriers could be moved to external magnets with a heater for field-cooling. Additionally, they were also used for polar Kerr imaging. The movability of these chip carriers allowed to perform the subsequent NF-SANE scan of the same magnetic structure as the one observed with the polar Kerr microscope.

The generated ANE signal was fed directly to the lock-in through the attached shielded cables; no additional preamplifier was used. The ANE signal generated by the optical near-field was detected by demodulating the measured voltage signal at the second harmonic of the tip vibration frequency using a MFLI lock-in amplifier. For the majority of the experiments, a time constant of 300 ms and a third order filter were used. An integration time of 900 ms was used so that the measurement time was ≈1 s/pixel. At this set of parameters, the lock-in noise was ≈10 nV at ≈550 kHz. We also tried these experiments with another lock-in amplifier (HF2LI) from the Zurich instruments that provides higher band width of up to 50 MHz in comparison to 1 MHz for MFLI. We observed a higher noise with HF2LI in the lower frequency regime of the interest (≈550 kHz). The MFLI band width of 1 MHz sufficed for the NF-SANE measurements and was preferred due to a smaller noise.

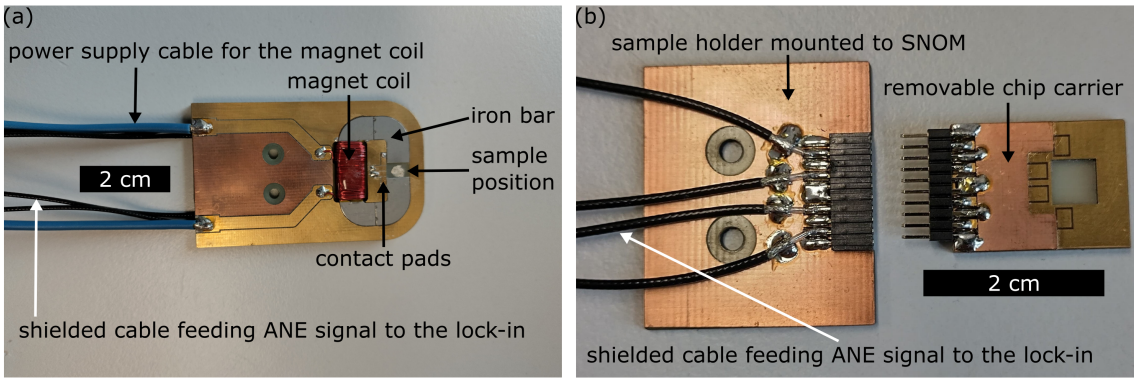

Figure 3.10: Sample holders for NF-SANE experiments. (a) With a small magnet coil. This sample holder was originally designed by Chris Koerner. The one shown here is a modified version that was adopted for NF-SANE measurements. (b) With a removable chip carrier.

3.4 COMSOL simulations

We used COMSOL multiphysics to simulate the temporal and spatial distribution of the temperature inside a 15 nm thick CoFeB film subjected to a laser-induced heating [99]. The radial distribution of the laser intensity was assumed to be Gaussian,

$$I(r) = \frac{P}{2\pi \cdot \sigma^2} \cdot e^{-\left(\frac{r^2}{2\sigma^2}\right)} \qquad [\mathrm{W/m^2}] \tag{3.1}$$

The total incident laser power obtained by integrating equation (3.1) over the entire 2D space comes out to be P. The full width at the half maxima (FWHM) is $2\sqrt{2\ln(2)}\sigma \approx 2.355\sigma$. A fraction α of the incident laser beam passes through the film, where $1-\alpha$ is the reflection coefficient of the CoFeB film. Due to the absorption in the film, laser power is attenuated exponentially inside the film,

$$I(r,z) = \frac{\alpha \cdot P}{2\pi \cdot \sigma^2} \cdot e^{-\left(\frac{r^2}{2\sigma^2}+\frac{z}{z_0}\right)} \qquad [\mathrm{W/m^2}] \tag{3.2}$$

Where $Z_0 \approx 10\,\mathrm{nm}$ is the attenuation depth of the CoFeB film. Absorbed energy within a unit length along z is $\frac{\mathrm{d}i}{\mathrm{d}z}$, this gives energy density of the laser heating,

$$Q(r,z) = \frac{dI}{dz} = \frac{\alpha \cdot P}{2\pi \cdot \sigma^2 z_0} \cdot e^{-\left(\frac{r^2}{2\sigma^2}+\frac{z}{z_0}\right)} \qquad [\mathrm{W/m^3}] \tag{3.3}$$

Modulation of the laser beam can be modelled as sinusoidal time dependence of the laser intensity,

$$Q(r,z,t) = \frac{\alpha \cdot P}{2\pi \cdot \sigma^2 \cdot z_0} \cdot e^{-\left(\frac{r^2}{2\sigma^2}+\frac{z}{z_0}\right)} \cdot \sin^2\left(\frac{2\pi t}{T}\right) \qquad [\mathrm{W/m^3}] \tag{3.4}$$

Where $T = \frac{1}{f}$, and f is laser intensity modulation frequency. The heat energy described by equation (3.4) alters the CoFeB temperature. The absorbed heat is subsequently dif-

fused through the MgO substrate underneath the film. The heat conduction module in COMSOL was used to perform finite element modeling simulation to solve the heat diffusion problem numerically.

Since the heat source is axis symmetric, a 2D axis-symmetric coordinate system (r,z) was used. To reduce the computational time, The dimension of the MgO substrate was reduced to 100 µm in both the r, and z directions. This provides a sufficiently large heat sink to diffuse the laser heat absorbed within the nanoscale region. The real space was discretized using a free triangular mesh. In the vicinity of the laser spot, an extremely fine mesh was used. Along the z-direction, with only 15 nm thick CoFeB film, a manual mesh size (smaller than a nm) was used so that the film region contained several nodes. A time-dependent study was performed for a duration of $1.25T$ with a total of 500 equally spaced points.

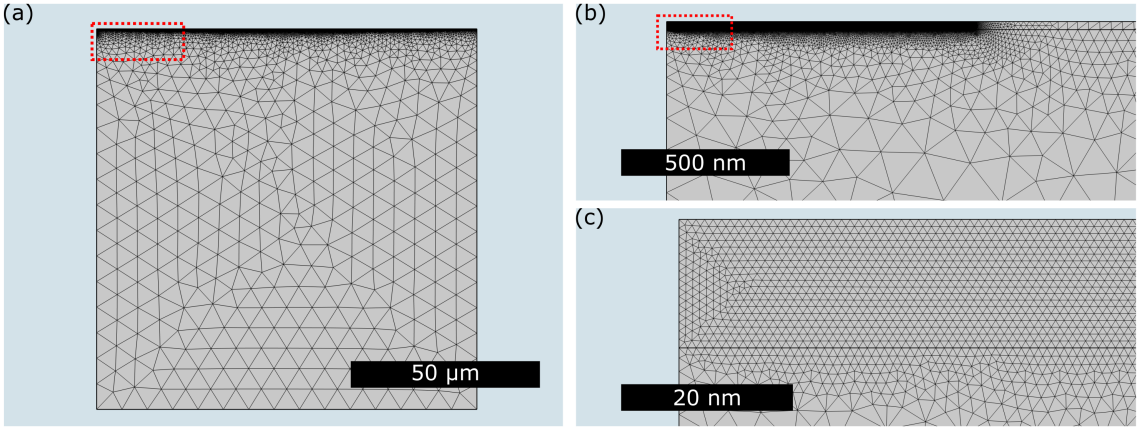

Figure 3.11: Free triangular mesh in COMSOL simulations. (a) Full structure. (b) In the region near the laser spot, as indicated by the dotted square in (a). (c) In the region near the CoFeB film, as indicated by the dotted square in (b).

The CoFeB film consisted of 60% cobalt and 20% Boran, which have similar physical parameters such as density and heat capacity. For this reason, physical parameters for CoFeB were assumed to be that of Co. The following table summarizes these parameters for CoFeB as well as the MgO substrate:

Table 3.3: List of physical parameters for the COMSOL simulations

Material	Heat capacity (J/(kg.K))	Density (kg/m^3)	Thermal conductivity (W/(m.K))
CoFeB	430	21450	70
MgO	877	3580	42

3.5 Micromagnetic simulations

We used MuMax3 to simulate magnetic structures in the CoFeB film [100]. Considering the exchange length ($\lambda_{exc}\approx$8.6 nm) for the CoFeB film, we discretized the structure into the cubes of the size 512 nm^3 so that the step size was of 8 nm was smaller than λ_{exc}.

The magnetic state was initially randomized, and then a decaying a.c. magnetic field was applied to simulate the vortex ground state. The relaxation process was done following the Runge-Kutta (RK45) method [101].These simulations were performed by Jitul Deka, who assumed the following set of parameters for the CoFeB film [102]:

- IP magnetic anisotropy constant K: 2.02 kJm^{-3}
- Exchange constant A: 20 pJm^{-1}
- Saturated magnetization M_S: 65 kAm^{-1}
- Damping coefficient α: 0.03

3.6 X-ray diffraction

We used X-ray diffraction (XRD) to determine the crystallographic properties of our sputter-deposited Mn_3Sn film. XRD is a well-established and powerful tool that enables the analysis of crystal structures of solids [103, 104]. It works by shining an X-ray beam on the sample and measuring the intensity of the reflected beam that relates to the crystal structure of the sample. The incident beam is shined at an angle θ with respect to the sample surface (-$\hat{\mathbf{a}}$ in Figure 3.12), the reflected beam is directed at an angle θ with respect to $\hat{\mathbf{a}}$. Thus, the diffracted beam is diverted with respect to the incident beam by an angle of 2θ (Figure 3.12). The intensity of the diffracted beam for a given incident angle is de-

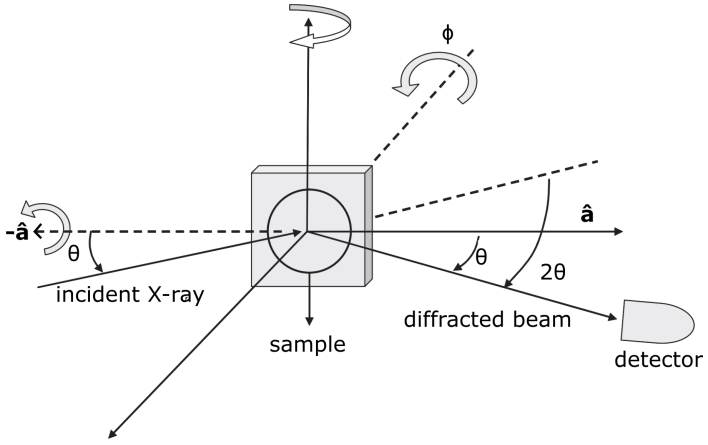

Figure 3.12: Schematic showing 2θ- and ϕ-scan geometry of the XRD measurements. The figure is adopted from [105].

pendent on the crystal orientation of the sample. We perform such a 2θ scan for different incident angle θ. The value of θ for which the intensity shows a maxima characterizes the crystal orientation of the sample. For a well-ordered epitaxially grown film having a crystal orientation $\mathbf{d}$, we observe a large peak at an angle $\theta_{\mathbf{d}}$ in a 2θ scan. Observation of such peaks confirms the epitaxial growth of the film. However, even a well-epitaxially grown film can have any random orientation around the z-axis of the sample. A ϕ-scan

allows the differentiation of these different orientations around the z-axis of the sample. Here, an XRD scan at a fixed incident angle $\theta = \theta_{\mathbf{d}}$ but at a different sample rotation angles (ϕ) is performed (Figure 3.12). If all the grains have a fixed specific orientation around the z-axis, then the Mn_3Sn film having a hexagonal crystal structure would have a six-fold symmetric ϕ scan. This symmetry would be lifted if the grains are randomly oriented. The XRD measurements of the Mn_3Sn film were performed by Prajwal Rigvedi using a Bruker D8 discover system that is capable of performing both the 2θ- as well as the ϕ-scans.

Part II

Magnetic domain imaging

Chapter 4

Magnetic domain imaging with helicity-dependent photoconductivity

In this Chapter, we demonstrate the utility of helicity-dependent photoconductivity for probing the magnetization of an OOP-magnetized sample. We rely on the HDP signal originating from the magnetic circular dichroism effect [106]. MCD effect refers to differential absorption of the left- and right-circularly polarized lights in magnetized materials. The X-ray-based MCD (XMCD) effect is widely used to probe the magnetic properties of a sample [107]. Here, we utilize a MCD signal generated by a tabletop available visible laser with a wavelength of 532 nm. The spatially resolved scanning measurement allows for imaging of the magnetic domain structure of the sample.

4.1 Helicity-dependent photo-voltage

To study the optical MCD effect, a magnetic sample is illuminated with a circularly polarized laser beam (Figure 4.1a). The helicity of the polarization is modulated between LCP and RCP using a PEM and a linear polarizer (see methods for the details). A part of the incident laser beam is absorbed by the sample. Due to the MCD effect, the absorption (A) is modulated at the helicity modulation frequency (ω), as shown in Figure 4.1b. Since the absorption modulation amplitude (ΔA^{ω}) depends on the magnetization, we can image the magnetic domain structure of the sample by performing spatially resolved measurements of ΔA^{ω}. In the experiments, ΔA^{ω} is measured electrically. Such an electrical measurement is possible because the resistance of the sample changes due to laser-induced heating that depends on the absorption A. Consequently, modulation of A leads to modulation of the sample resistance (R) with a modulation amplitude of R^{ω} (Figure 4.1c). To measure the modulated R^{ω} (on the order of 100 $\mu\Omega$), a constant amplitude current is applied through the sample patterned into the wire structure (see Figure 4.1a). The applied current of the constant amplitude gives a modulated voltage signal ($V^{\omega}_{\mathrm{HDP}}$) due to the resistance modulation. Thus, the illumination of the sample with a helicity-modulated beam and applying a current of constant amplitude gives a helicity-dependent voltage.

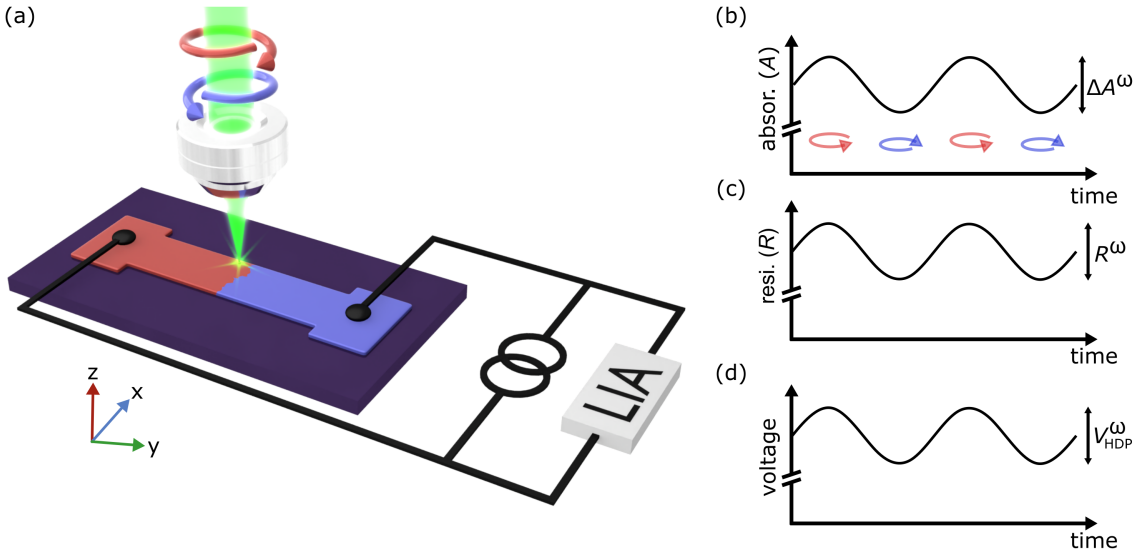

Figure 4.1: (a) Schematic showing a magnetic wire with a multi-domain state is illuminated with a circularly polarized laser beam. The helicity of the polarization is modulated between LCP and RCP. The resulting HDP signal is measured by applying a d.c. current and demodulating the voltage with a MFLI lock-in amplifier. This graphic was prepared by Chris Koerner for our publication [97].(b) Helicity modulation leading to the absorption modulation. (c) Modulation of the wire resistance due to MCD effect. (d) Voltage modulation due to HDP.

4.2 Sample characterization

We demonstrate the HDP voltage-based magnetic imaging method in a sample with a perpendicular magnetic anisotropy. PMA materials give out-of-plane polarized magnetic domain structures that provide a large MCD-induced absorption. The sample consists of a Co/Ni/Co stack [108, 109] deposited on a MgO(001) substrate by a sputtering method (see methods for details). A Pt under-layer was used, whose interface with Co provides a PMA anisotropy, and the film was capped with a 3 nm thick TaN layer to prevent it from oxidation. A hysteresis measurement based on the polar Kerr effect verifies that the film provides an OOP polarization in the remanence (Figure 4.2).

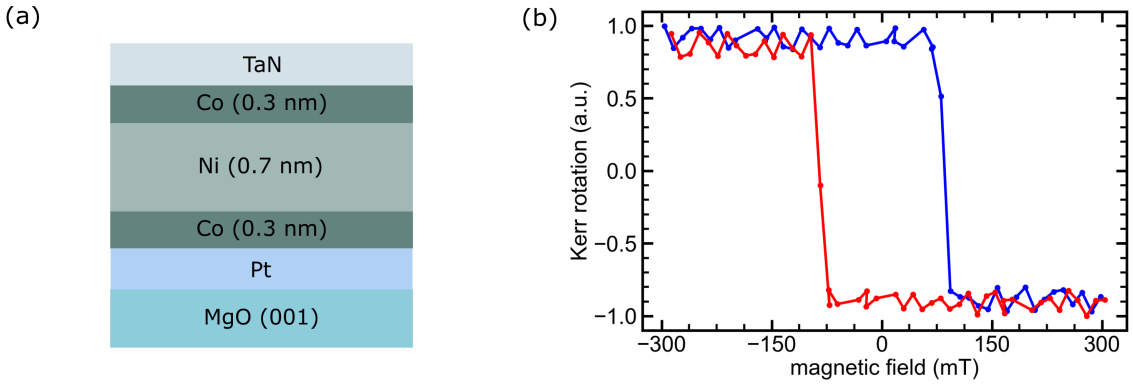

Figure 4.2: (a) Schematic showing the layered structure of the Co/Ni/Co stack. (b) The polar Kerr-based hysteresis measurement of the sample utilized for the HDP measurements.

4.3 Magnetic domain imaging

In order to perform the HDP-based electrical measurements, the film is patterned into a 10 µm × 15 µm wire structure sandwiched between the contact pads made of the same material (Figure 4.3a). The magnetic domain structure of the device is manipulated by applying a small magnetic field. The remanence state contains a domain wall trapped in the wire Section of the device, as shown by the polar Kerr microscopy (Figure 4.3b). Subsequently, the same magnetic structure is investigated with the scanning HDP measurements. While illuminating the wire with the helicity-modulated circularly polarized laser beam, a d.c. current of 2.5 mA is applied to measure the resulting photo-resistance. This is done by demodulating the resulting voltage drop across the sample at the helicity modulation frequency. Spatially resolved measurement of $V^{\omega}_{\mathrm{HDP}}$ reveals the same contrast as that from the Kerr microscope (Figure 4.3c).

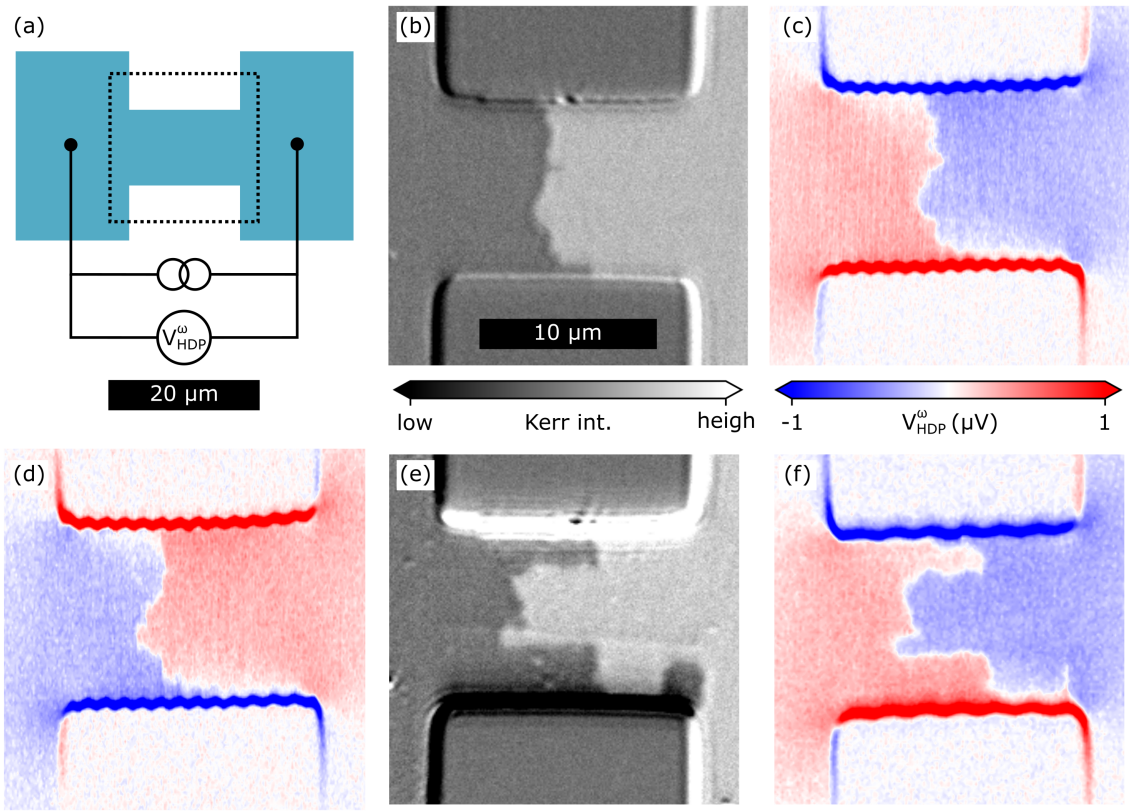

Figure 4.3: (a) Schematics of the device structure utilized for the HDP measurement. A 10 µm × 15 µm wire structure is attached to 150 µm × 150 µm contact pads from the two sides. A d.c. current is applied, and the resulting voltage is measured by a lock-in amplifier through the contact pads. (b) Polar Kerr microscope image of the device showing a magnetic domain wall in the wire Section of the structure. (c) The same magnetic structure investigated with scanning HDP measurement by applying a 2.5 mA current. (d) HDP measurement repeated with an applied current of −2.5 mA. (e) An altered magnetic domain structure in the device shown by the Kerr microscope. (f) Magnetic domain structure in (e) investigated with the HDP measurement.

The scanning measurement is repeated with an applied current of −2.5 mA; this also reproduces the magnetic domain contrast with a reversed sign of $V^{\omega}_{\mathrm{HDP}}$ (Figure 4.3d). The

dependence of the HDP voltage on the current confirms that it is induced by the applied current. Since the applied current has constant magnitude, observation of the HDP voltage at ω implies modulation of the wire resistance at the helicity modulation frequency. To further confirm that the resistance modulation results from the MCD effect induced by the wire magnetization, we create a different domain structure in the wire (Figure 4.3e). Subsequent HDP measurements reveal the new magnetic domain structure (Figure 4.3f).

We also perform the HDP domain imaging in a different $10\,\mu m \times 5\,\mu m$ wire structure. Here also, HDP-based domain imaging reproduces magnetic contrast obtained by Kerr microscope. Domain images for the two different domain structures in this device are shown in Figure 4.4.

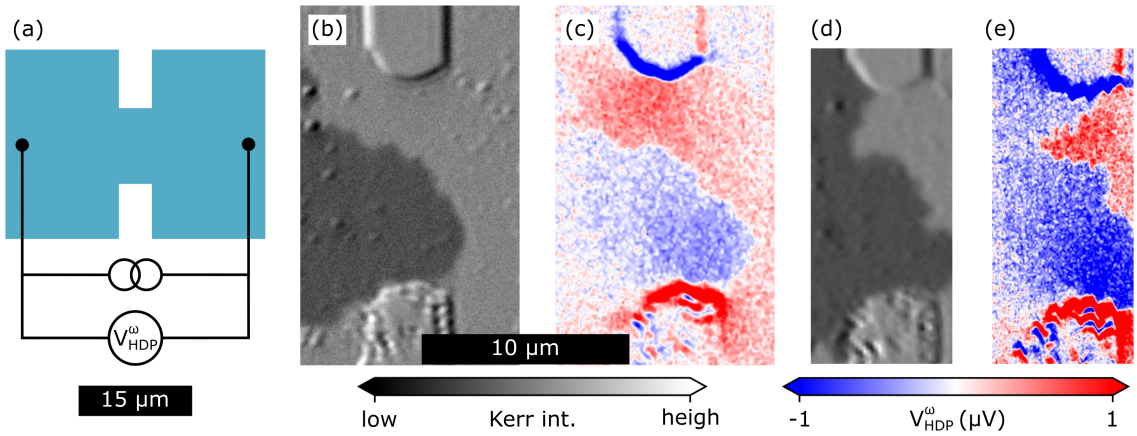

Figure 4.4: HDP-based magnetic domain imaging performed for a different a $10\,\mu m \times 5\,\mu m$ wire structure. (a) Schematic of the device structure. (b,d) Magnetic domain structure observed by the polar Kerr microscope. (c,e) HDP-based magnetic domain structures in (c) and (e) reproduce Kerr contrast in (b) and (d), respectively.

4.4 Origin of the HDP signal

To verify if the observed HDP signal originates from the MCD effect, we investigate the dependence of the HDP signal amplitude on the polarization state of the incident laser beam. For this, the amplitude of the retardation (α) between E_x and E_y is varied between $0°$ and $310°$. Retardation modulation with an amplitude of $0°$ corresponds to a constant linearly polarized laser beam. The amplitude of $90°$ and $270°$ leads to circular polarization with a helicity modulation between LCP and RCP. The helicity modulation would be out of phase between the two cases of $90°$ and $270°$. Any other intermediate amplitude results in helicity-modulated elliptical polarization. We measure the HDP signal for the domain structure shown in Figure 4.4b at the different retardation amplitude. HDP signal measured at a point in the region with $m_z > 0$ vs retardation amplitude α is shown in Figure 4.5. We see a negligible signal for the linearly polarized laser beam ($\alpha \approx 0$). The maximum signal is observed for the helicity-modulated circular polarization ($\alpha = 90°, 270°$). The signal polarity for $\alpha = 90°$ is opposite to that for $\alpha = 270°$. This difference in polarity is due to a $180°$ phase gap in helicity modulation for these two cases. This confirms

that the HDP signal correlates with the polarization state of the incident laser beam. Ideally, we expect a purely periodic signal as a function of α. However, as α is increased beyond 90°, the light undergoes multiple RCP to LCP transitions within one modulation cycle, reducing the detectable HDP signal. This decreases the overall signal amplitude and results in a damped periodic signal as a function of α.

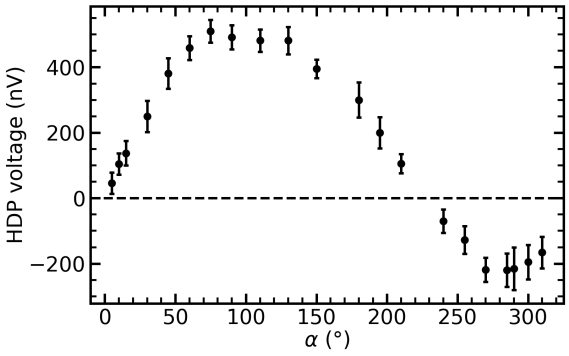

Figure 4.5: The measured HDP single magnitude as the function of the amplitude of the retardation. The error bar of 20 nV corresponds to the RMS noise of the signal averaged over 30 seconds.

4.5 HDP signal near the edges of the wire structures

In addition to the magnetic domain contrast, we also observe a relatively larger signal ($\approx$1 μV) at the edges of the magnetic wire (Figure 4.3c). Previously, such a HDP signal has also been observed at the wire edges of nonmagnetic materials such as topological insulators $BiSbTeSe_2$ [110], Bi_2Se_3 [111], a heavy metal Pt [111, 112], and a noncollinear antiferromagnet Mn_3Ir [113]. They are attributed to spin Hall effect (SHE) induced spin accumulation [114], resulting in HDP signals of opposite signs at the two edges (Figure 4.6a,b). In our measurements, this could arise due to SHE from Pt under-layer in the Co/Ni/Co stack. However, the magnitude of such a SHE-induced HDP signal is intriguing, as it is higher than the HDP signal from the magnetic moment in a ferromagnet. This implies that the total SHE-induced magnetic moment at the edges must be larger than that in a ferromagnet. In typical ferromagnets, a magnetic moment of 1 μB per atom is expected. On the other hand, based on previous experiments and theoretical considerations, the SHE-induced moment is expected to be 1×10^{-5} μB per atom only [115, 116]. This is in contradiction to over observations.

HDP signal arises from the wire's periodic heating due to differential absorption during the helicity modulation. Near the edges of the wire, periodic heating can occur due to the wobbling of the focused laser beam (Figure 4.6c). This periodic heating would modulate the wire resistance, resulting in a voltage signal for an applied current of fixed amplitude. We show that PEM induces a focal spot shift of a few nanometers at the helicity modulation frequency [97]. The periodic heating from this focal shift results in a voltage signal at the same frequency [97]. Another contemporary work also supported

this explanation of the HDP edge signal [117]. This artifact signal was previously falsely attributed to SHE-induced HDP signal [110, 111, 113].

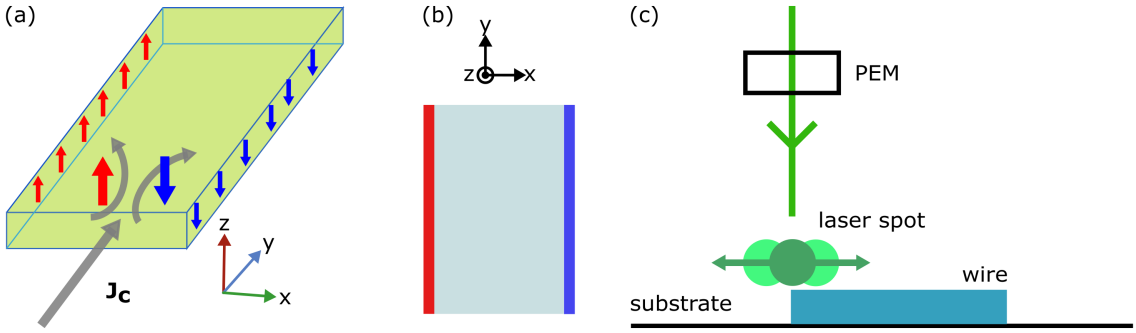

Figure 4.6: (a) Illustration of SHE-induced spin accumulation near the wire edges of a heavy metal. (b) Schematic illustration of expected HDP signal due to SHE induced spin accumulation. (c) A laser beam passing through the PEM is focused near the edge of a wire deposited on a transparent substrate. Due to the different absorption of the wire and the substrate, wobbling caused by the PEM results in periodic heating of the wire.

Thus, we observe an artifact near the edges of the wire structures. Here, the wobbling of the laser spot induced by the PEM causes periodic heating of the sample, resulting in a voltage signal at the helicity modulation frequency. Since the laser beam focal spot wobbles in a specific direction, such an artifact can be avoided by orienting the wire structure along the laser spot wobbling direction [97, 117].

4.6 Conclusion

We have shown that MCD-driven helicity-dependent absorption in a magnetic material can be converted to an electrical read-out signal related to the material's magnetic state. Spatially resolved scanning measurements of such a signal allow magnetic domain imaging. Since the read-out signal relies on the MCD effect present in a wide range of magnetic materials, the obtained results are significant for all such classes of magnetic materials. Of particular interest are noncollinear antiferromagnets, which have been shown to exhibit Berry curvature-driven Kerr [35–40] and MCD [41, 42] responses that correlate to their antiferromagnetic ordering.

Chapter 5

SANE microscopy for IP magnetization

Here, we discuss magnetic readout signals based on magnetotransport response. One such example is the anomalous Hall effect (AHE), which arises from a Berry curvature-induced effective field. AHE also emerges in noncollinear antiferromagnets with chiral spin texture, making this phenomenon interesting for antiferromagnetic spintronics. AHE generates a voltage orthogonal to an applied current in the plane of magnetic thin films, making it sensitive to the out-of-plane components of magnetization. An analogous phenomenon is the anomalous Nernst effect (ANE), which is also generated by Berry curvature in ferromagnetic and noncollinear antiferromagnetic material. ANE generates an electric field (**E**) transverse to both magnetization **M** and an applied temperature gradient (∇T). This has the advantage that because a temperature gradient can be applied IP and OOP in thin film devices, both IP and OOP components of magnetization can be measured. In addition, by using laser heating to generate a spatially confined ∇T, spatially resolved scanning measurements of ANE enable magnetic domain imaging.

This method of scanning ANE microscopy has previously been utilized to image the magnetic domain structures of IP-magnetized thin films with a spatial resolution of a few micrometers [54–57]. More recently, the spatial resolution has been improved by using an optical-near-field [58–60]. In this Chapter and Chapter 6, we study a ferromagnetic film with well-understood magnetic structures to deduce the magnitude and spatial distribution of the temperature gradient that is required for an ANE signal. The obtained results are supported by the finite element modeling simulation of the laser heating (Section 1-5,8), and the magnetic contrast observed by the ANE microscopy is verified by that with the Kerr microscopy (Section 4). Finally, we study the influence of various measurement geometrical factors on the magnitude of the measured ANE signal (Section 6).

5.1 Scanning ANE microscope principle

We employ a scanning confocal optical microscope for ANE-based magnetic domain imaging. A laser beam is focused on the sample by an objective lens (Figure 5.1a). A fraction of the laser beam is reflected, while the rest is exponentially attenuated as it passes through the sample. This means that the laser beam is absorbed more at the film's

top surface than at the bottom surface. The heating caused by the absorbed laser beam energy creates an OOP temperature gradient ($\nabla_z T$) underneath the focal spot. Here, $\nabla_z T$ denotes the z component of the temperature gradient. This gradient results in an ANE response transverse to $\hat{\mathbf{z}}$ and the magnetization ($\mathbf{M}$). Measuring this ANE response allows us to deduce the IP magnetization underneath the laser focal spot. By performing scanning measurements of such an ANE signal, a map of the IP magnetization of the sample can be constructed. This provides us with a magnetic domain image of an IP-magnetized material.

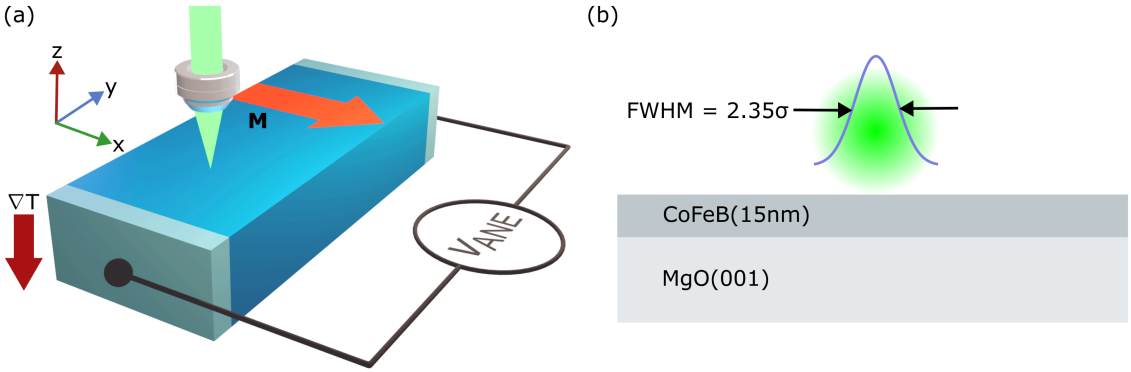

Figure 5.1: (a) Schematic illustration of the ANE imaging method. A laser beam focused by the objective lens creates a temperature gradient with a nonzero OOP component (red arrow). This gradient generates a V_{ANE} related to the transverse component of the magnetization (the orange arrow). (b) Schematic showing the radial intensity distribution of the focused laser beam.

5.2 Laser heating induced OOP temperature gradient

In order to understand the characteristics of laser heating-induced ANE signal, it is important to study the magnitude and spatial distribution of ∇T. Here, we systematically study the laser heating-induced temperature gradient generated out-of-plane of the sample. A laser beam with a wavelength of 532 nm is focused by an objective lens with a numerical aperture (*NA*) of 0.7 (Nikon ELWD 60X) onto a magnetic thin film sample. We study an IP magnetized 15 nm thick film of $Co_{60}Fe_{20}B_{20}$ deposited on a MgO (001) substrate by sputtering (see methods for details). The laser beam intensity on the CoFeB sample underneath the focal spot is expected to be spatially nonuniform (Figure 5.1b).

5.2.1 Intensity distribution of the focused laser beam

The laser heating-induced temperature increment depends on power density, which depends on the laser power and the radial intensity distribution of the laser beam at the focal spot. The laser power behind the objective lens was measured using a power meter from Thorlabs (model: PM100D). The intensity distribution was obtained by scanning an edge of a 100 nm thick Au film underneath the laser focal spot (Figure 5.2a). The intensity of

the reflected beam (I_{ref}) is measured as a function of edge position (x). It can be written as:

$$I_{\text{ref}}(x) = \int_{-\infty}^{x} r_1 I(r)dr + \int_{x}^{\infty} r_2 I(r)dr$$

Where r_1 and r_2 denote the reflection coefficient for the substrate and the film, respectively. Defining $\int I(r)dr = I^{\text{int}}(r)$, we have,

$$I_{\text{ref}}(x) = (r_1 - r_2) \cdot I^{\text{int}}(x) + constant$$

Taking the derivative of above equation gives,

$$\frac{\mathrm{d}Ref(x)}{\mathrm{d}x} = (r_1 - r_2) \cdot \frac{\mathrm{d}I^{\text{int}}(x)}{\mathrm{d}x} = (r_1 - r_2) \cdot I(x) \tag{5.1}$$

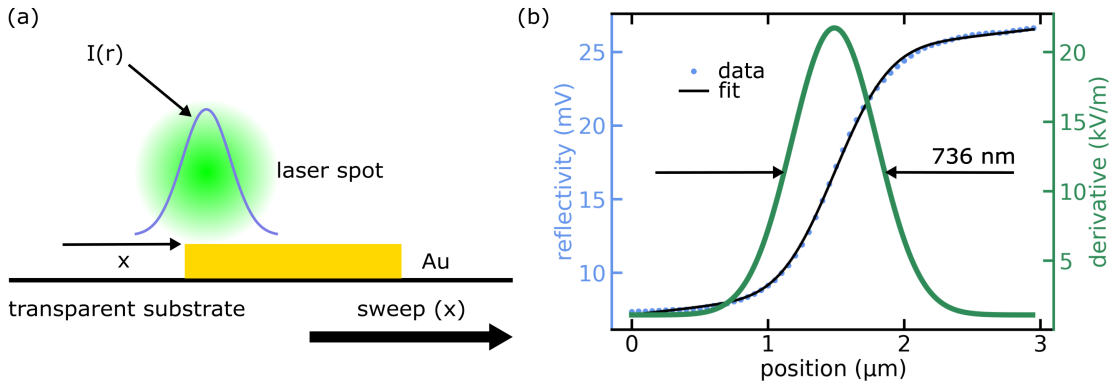

Figure 5.2: (a) Schematic showing a laser beam focused near the edge of a gold film on a transparent substrate. The film is scanned underneath the laser spot, and the intensity of the reflected beam is measured as the function of edge position (x). (b) Plot of reflectivity line scan against x, and fit of the line scan to an error function (blue, left axis). The spatial derivative of the fit to the reflectivity line scan is shown on the green, right axis.

Equation (5.1) shows that laser intensity distribution $I(x)$ is proportional to the derivative of the reflectivity line scan. The intensity line scan measurement is shown in (Figure 5.2b); it is well described by an error function, as shown with the fitted black curve. The radial distribution of the laser intensity is determined by taking the derivative of this line scan, which is a Gaussian distribution with FWHM = 736 ± 22 nm.

5.2.2 Magnitude of the OOP temperature gradient

The laser beam underneath the focal spot provides a Gaussian heat source with FWHM ≈750 nm ($\sigma \approx 320$ nm). In our experiments, the incident laser power on the CoFeB film is 5 mW. Assuming the reflection coefficient of CoFeB to be 0.65 for the laser wavelength of 532 nm [118], the power of the laser beam passing through the film would be 1.75 mW. The absorbed part of the beam acts as a heat source with spatially nonuniform energy density. Due to modulation of the laser beam, the heat source varies sinusoidal in time at the optical chopper frequency $f = 600$ Hz. The energy density distribution (at $t = T/4$) is shown in Figure 5.3a. This heat source alters the film temperature, which varies in space and time. The spatial and temporal dependence of the film is simulated using the COMSOL multi-physics heat transfer module (see methods for details). The obtained temperature distribution at $t = T/4$ is shown in Figure 5.3b.

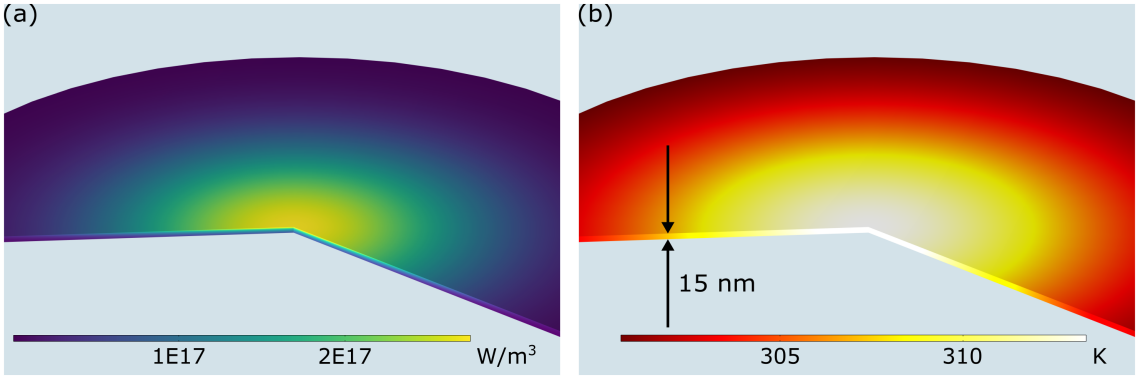

Figure 5.3: Heat source energy density and temperature distribution subjected to heating by a modulated laser beam at $t = T/4$. (a) Spatial distribution of the energy density of the absorbed laser beam in the CoFeB film. (b) The temperature distribution in the film.

A line graph of the temperature along the film thickness at the center of the laser spot is shown in Figure 5.4a. This shows a monotonous decrease in the temperature from the top surface to the bottom. A higher temperature at the top surface is expected as the laser heating is higher at the upper surface than at the lower surface. The average temperature gradient along the z-direction is defined as,

$$\nabla_z T = \frac{T_{\text{top}} - T_{\text{bottom}}}{t} \tag{5.2}$$

Where t is the film thickness. The simulated results indicate a temperature difference of 0.13 K across the 15 nm film. This amounts to a temperature gradient of $\nabla_z T \approx 9 \times 10^6$ K/m. The time dependence of $\nabla_z T$ shown in Figure 5.4b indicates that heat diffusion is fast enough to allow the temperature gradient to be modulated at the optical chopper frequency $f = 600$ Hz.

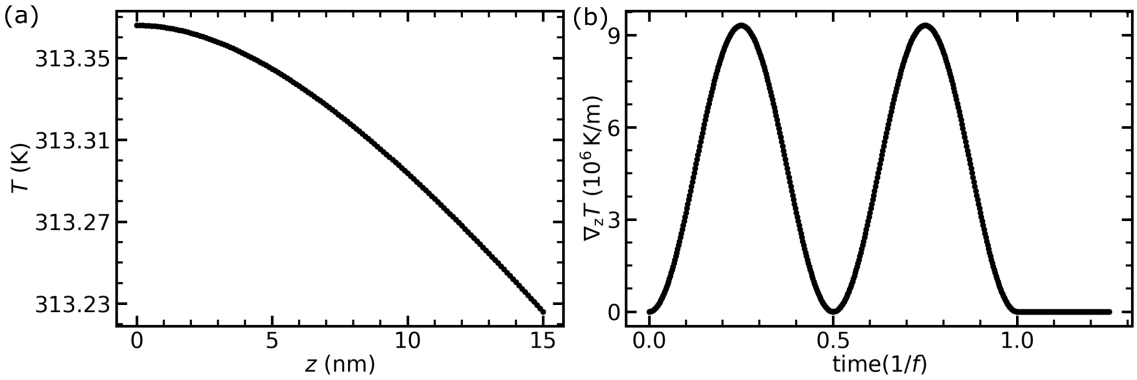

Figure 5.4: (a)) Line graph of the temperature across that film thickness. (b) Time dependence of the OOP temperature gradient ($\nabla_z T$).

5.3 Laser heating-induced ANE signal in IP-magnetized wire

Here, we consider laser heating-induced ANE signal in an IP-magnetized ($\mathbf{M} = M_x\hat{\mathbf{x}} + M_y\hat{\mathbf{y}}$) magnetic wire structure. For IP-magnetized sample, IP component of the ANE-induced electrical response is generated by $\nabla_z T$ and can be written as follows:

$$\mathbf{E}_{\mathrm{ANE}} = \mu_0 S_{\mathrm{ANE}} \nabla T \times \mathbf{M} \tag{5.3}$$

$$= \mu_0 S_{\mathrm{ANE}} \nabla_z T \cdot M_y \hat{\mathbf{x}} + \mu_0 S_{\mathrm{ANE}} \nabla_z T \cdot M_x \hat{\mathbf{y}} \tag{5.4}$$

Where μ_0 is the vacuum permeability, S_{ANE} indicates the ANE coefficient, and $\mathbf{M}$ is the unit vector of the magnetization. The measured ANE voltage along the wire length (y-direction) is given by,

$$V_{\mathrm{ANE}} = E^y_{\mathrm{ANE}} \cdot l_{\mathrm{spot}} \tag{5.5}$$

$$= \mu_0 \cdot S_{\mathrm{ANE}} \cdot \nabla_z T \cdot M_x \cdot l_{\mathrm{spot}} \tag{5.6}$$

Here, l_{spot} is the dimension of the spot over which the heat gradient is present. We measure V_{ANE} to deduce information about M_x. For this, the CoFeB film is patterned into a 10 µm wide wire, as shown schematically in the inset of Figure 5.5a. The wire is scanned with the focused laser beam while a ±40 mT magnetic field is applied along the wire width (x-direction) to saturate the magnetization. We observe an ANE signal of ≈4 µV as the laser beam hits the wire. The signal is of magnetic origin as its polarity changes when the magnetic field is reversed in direction (Figure 5.5a). The magnitude of the signal scales linearly with the laser power (Appendix A.1), confirming that it is generated by the laser heating-induced temperature gradient. We now demonstrate that this ANE signal can be utilized to characterize magnetic properties. By scanning the laser over a 15 µm × 5 µm area and averaging V_{ANE} at different applied field strengths, we build up a magnetic hysteresis loop, as shown in Figure 5.5b. For this measurement, a device with width $w =$ 14 µm (wire length = 25 µm) is chosen because the wider wire reduces shape anisotropy and provides a reasonable coercive field to observe a hysteresis.

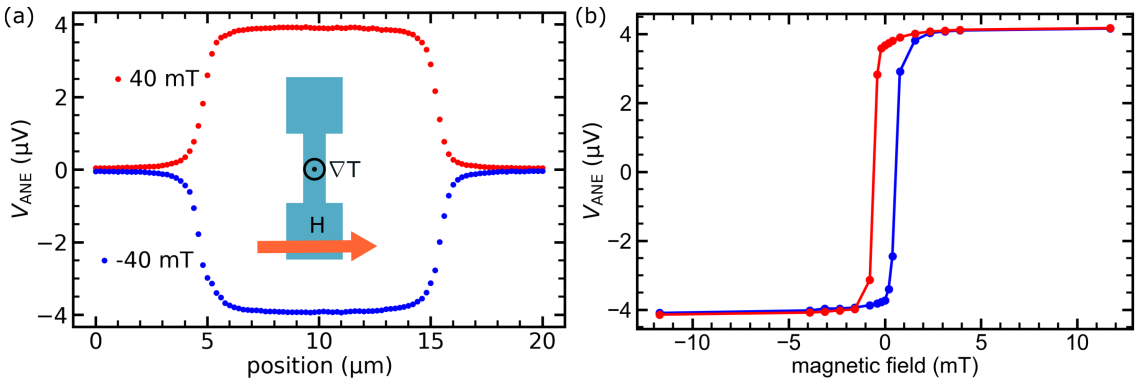

Figure 5.5: (a) ANE line scan of a 10 μm wide wire. The inset shows the device structure schematically. (b) ANE-based hysteresis loop measurement in a 14 μm × 25 μm wire structure.

5.4 ANE-based magnetic domain imaging

In the next step, we show that spatially resolved ANE measurements can be utilized to image the magnetic domain structure of a sample. Due to the shape anisotropy, magnetic moment orient along the wire length in the absence of the field. As a result, a multi-domain state in the remanence has negligible M_x component. However, to observe an ANE signal in our measurement geometry, a nonzero M_x is required (see equation (5.6)). To overcome this problem, we use CoFeB wire structures with branches, as shown in Figure 5.6. These branches stabilize a multi-domain remanent state. Such multi-domain magnetic structures provide nonzero M_x, as confirmed by longitudinal static Kerr microscopy. The same magnetic structures are subsequently transferred to the SANE microscope. The magnetic domain imaged by the ANE method reveals similar magnetic structures. The slight discrepancy in domain structures observed by the SANE and the Kerr microscopy is attributed to the instability of the domain structures. Since the coercivity field is very small on the order of a mT, the domain structures are altered during the sample transfer from one experimental setup to another.

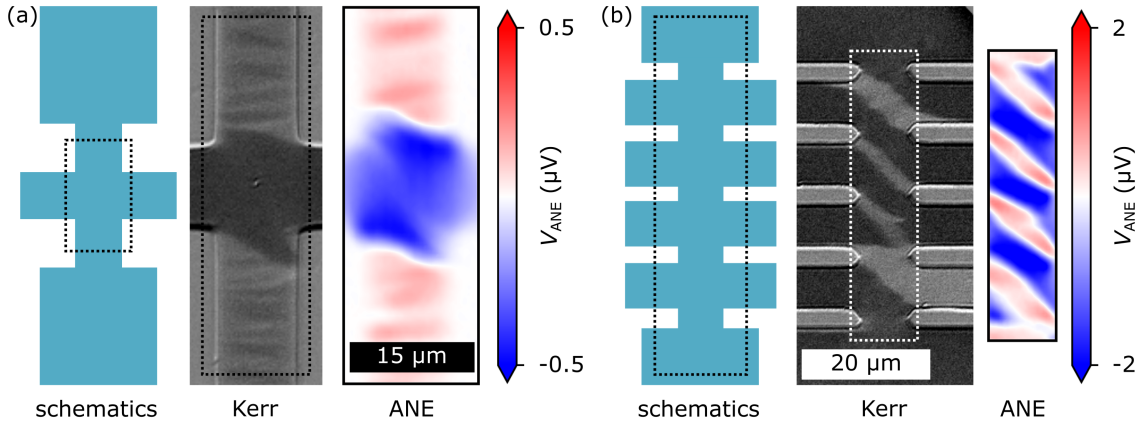

Figure 5.6: CoFeB wire structure with branches as shown by Schematic on the left. The middle part shows domain images observed by a longitudinal Kerr microscope; the same magnetic structure investigated with the SANE microscope is demonstrated in the right section. (a) A wire structure with one branch. (b) Same as (a) for the device with four branches.

5.5 Radial distribution of OOP temperature gradient

We demonstrated that SANE microscopy can image magnetic domain structures. Next, we find the spatial resolution of the ANE microscope. Since the spatial resolution in a scanning microscope is defined to be the FWHM of its probe, it is required to determine the spatial distribution of the OOP temperature gradient $\nabla_z T$.

5.5.1 Based on COMSOL simulation

We extract a line graph from the simulated temperature distribution in Figure 5.3b. This shows temperature spread in the radial direction at the top and bottom surface of the CoFeB film Figure (5.7a), the same is compared with the laser intensity distribution. We see that the temperature increment at both surfaces spreads beyond the laser focal spot. However, the gradient that is proportional to the difference in temperature at the two surfaces follows the laser intensity distribution very closely (Figure 5.7b). The FWHM of $\nabla_z T$ is 786 nm, which is only 3% higher relative to the FWHM of the laser intensity distribution (=750 nm).

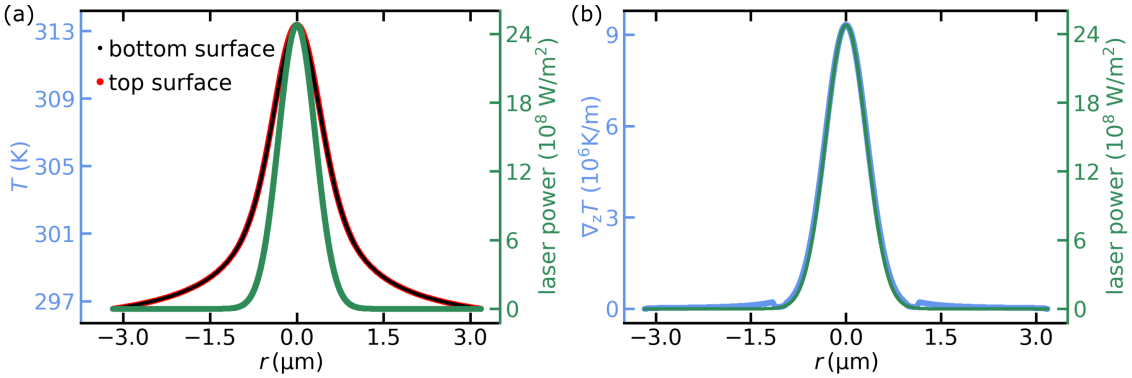

Figure 5.7: (a) Line graph in radial direction for the simulated temperature distribution at the top and bottom surface of the CoFeB film (blue, left axis). The laser intensity distribution is shown on the green right axis. (b) The radial distribution of $\nabla_z T$ (blue, left axis) is compared with the laser intensity distribution (green, right axis).

5.5.2 Based on experimental results

From the COMSOL simulation results, we expect the spatial distribution of $\nabla_z T$ in the SANE microscope to be nearly identical to the FWHM of the laser focal spot. To verify this claim, we determine the spatial distribution of $\nabla_z T$ experimentally. This can be done by scanning a magnetic domain wall across the heat gradient spot. For this, we require a stable multi-domain magnetic state with sharp transition (on a spatial scale much smaller than the spot size) between one domain state to another.

5.5.2.1 Landau pattern surrounding a magnetic vortex core

We realize such a magnetic structure in a nanoscale spin texture of a magnetic vortex [119]. This pattern is obtained in an 8 µm × 8 µm slab of a CoFeB film with a thickness of 45 nm. The slab is connected with a 1 µm contact wire at the top and the bottom, as shown in Figure 5.8. The ANE signal is measured using these contact wires. The micro-magnetic simulation shows that this structure hosts the Landau pattern with a magnetic vortex at the core Figure 5.8a. As one goes from top to bottom across the vortex, the IP magnetization rotates very rapidly from along the positive x-direction to the negative x-direction. This is because the magnetic vortex has a width of only a few nm [62, 63]. To create such a Landau pattern, the slab is demagnetized in a decaying a.c. magnetic field Figure 5.8b. A longitudinal differential Kerr microscope reveals this pattern experimentally. To observe the pattern with the SANE microscope, the structure was saturated with a 50 mT magnetic field, and then the field was reduced to zero. The remanence state forms a Landau pattern, as shown by the SANE microscopy image (Figure 5.8c). The magnetic structure of the Landau pattern can be tuned by changing the direction of the applied field, as discussed in Appendix A.3. We note that the ANE signal is larger near the connecting wires. This is due to the spread of the current generated by the ANE voltage. When the ANE voltage is generated away from the wires, the spread of the current leads to partial detection of the generated ANE signal.

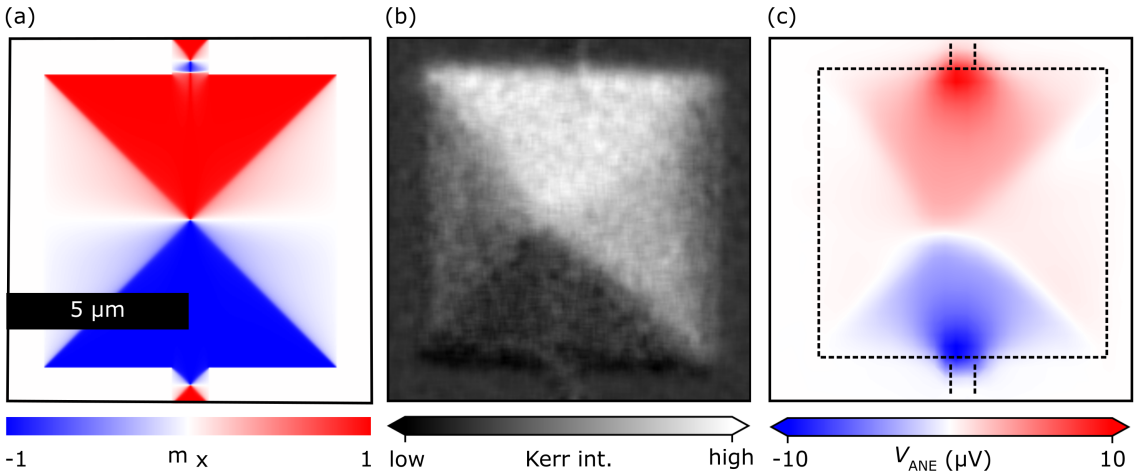

Figure 5.8: (a) The micro-magnetic simulation for a CoFeB slab with dimension 8 µm × 8 µm × 45 nm. The slab is connected with 1 µm contact electrodes at the top and bottom. (b) Longitudinal Kerr microscope image that maps M_x in the slab. (c) Landau pattern in the slab imaged by SANE microscope. The dotted lines indicate the slab outlines.

5.5.2.2 Scanning a magnetic domain wall underneath the focal spot

We show that similar to the laser intensity distribution measurements, the radial distribution of $\nabla_z T$ can be obtained by scanning a magnetic domain wall under the heat gradient

spot. In this case, we measure the ANE signal $V_{\mathrm{ANE}}(x)$ as the function of domain wall position (x). Following a similar analysis, one can show the following:

$$\frac{\mathrm{d}V_{\mathrm{ANE}}(x)}{\mathrm{d}x} = (m_1 - m_2) \cdot \nabla_z T(x) \tag{5.7}$$

Thus, $\nabla_z T(x)$ is directly proportional to the derivative of such an ANE line scan. We scan the magnetic vortex shown in Figure 5.8 underneath the laser focal spot. The line scan is shown in Figure 5.9; its derivative is well described by a Gaussian with FWHM = 760 nm. This reveals that $\nabla_z T(x)$ is Gaussian. Its FWHM (= 760 nm) is close to the value expected from the simulation results (786 nm).

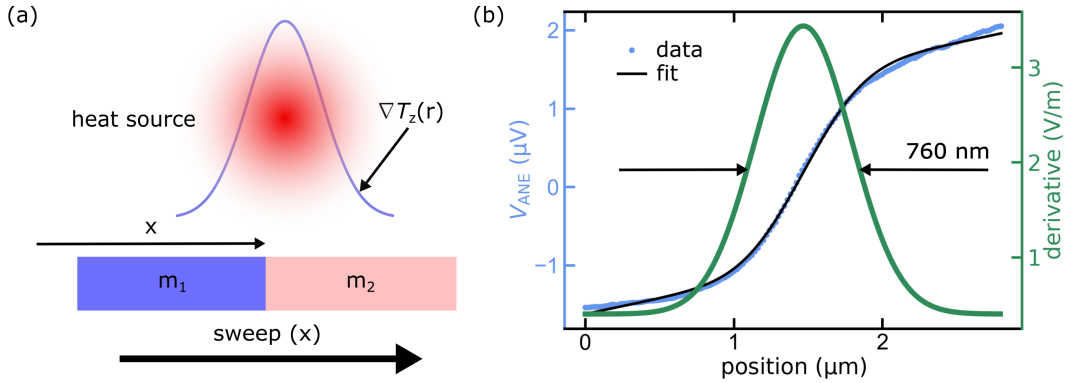

Figure 5.9: (a) Schematic showing a magnetic domain wall underneath a laser spot that generates an OOP temperature gradient $\nabla_z T(x)$. The domain wall is scanned, and the ANE signal is measured as the function of the domain wall position (x). (b) An ANE line scan across the magnetic vortex and the fit to an error function (left, blue axis), and the derivative of the fitted line (right, green axis).

5.6 Influence of geometrical factors on measured ANE signal

We analyze the effect of several geometric factors on the magnitude of the measured ANE signal. We consider the experimental geometry shown in Figure 5.1. A magnetic wire with a width of w is illuminated by a focused laser beam. The illumination generates an OOP temperature gradient over a region of dimension $L_x \times L_y$ (Figure 5.10a). We analyze the dependence of ANE voltage on w, and L_x, L_y.

5.6.1 Wire width dependence

First, we study wire width dependence while keeping other experimental parameters constant. An analytical model is developed that is then verified with the experimental data. The illuminated area ($L_x \times L_y$) acts as a battery due to the ANE-induced voltage (V_{gen}). The finite resistance of the illuminated area results in an internal resistance of the battery (R_{int}). The part of the wire shown in green provides a conducting path with resistance R_c (see Figure 5.10a). The remaining part of the magnetic wire adds to the contact wire resistance (R_{wire}). The equivalent circuit diagram is shown in Figure 5.10b. we determine

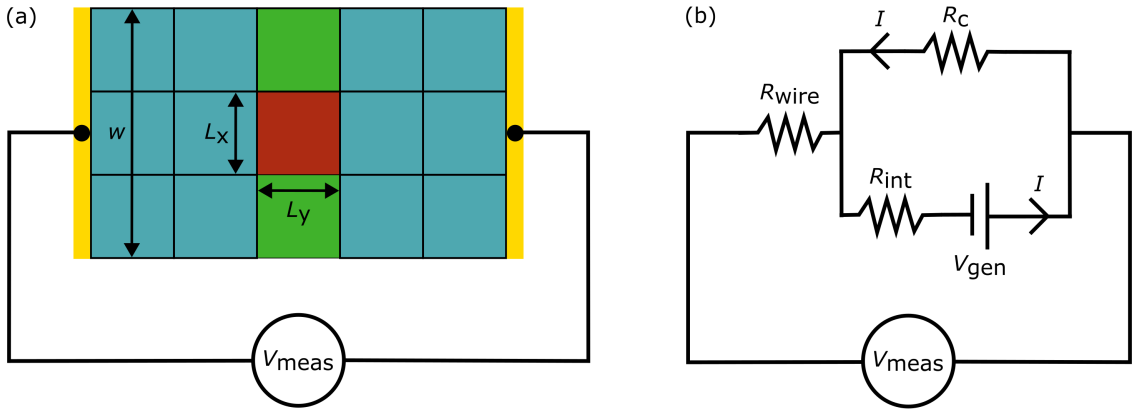

Figure 5.10: (a) Schematic showing a magnetic wire illuminated by a laser beam across the dimension $L_x \times L_y$. (b) An equivalent circuit diagram for the structure is shown in (a).

influence of R_c and R_{int} on the measured voltage V_{meas}. Since R_{wire} ($\approx 1\,k\Omega$) is much smaller than the lock-in impedance ($\approx 1\,M\Omega$), its role can be ignored. Therefore, V_{meas} is simply the potential across R_c, which is equal to $I \cdot R_c$, where I is the current flowing in the circuit.

$$\begin{aligned} V_{meas} &= I \cdot R_c \\ &= \frac{V_{gen}}{R_c + R_{int}} \cdot R_c \\ &= \frac{R_c}{R_c + R_{int}} \cdot V_{gen} \end{aligned}$$

Since $R_c \propto \frac{1}{w-L_x}$ and $R_{int} \propto \frac{1}{L_x}$

$$V_{meas} = \frac{\frac{1}{w-L_x}}{\frac{1}{w-L_x}+\frac{1}{L_x}} \cdot V_{gen} \tag{5.8}$$

$$= \frac{L_x}{w} \cdot V_{gen} \tag{5.9}$$

Equation (5.9) indicates that the measured ANE signal is inversely proportional to the wire width. To verify it experimentally, we measure ANE line scans across the CoFeB devices with different widths. The Magnitude of the ANE signal is clearly smaller in the wider wires (Figure 5.11a). The inverse dependence is shown by plotting the average ANE signal across the wire vs w. Equation (5.9) is verified by a linear fit of $1/V_{ANE}$ with w (Figure 5.11b).

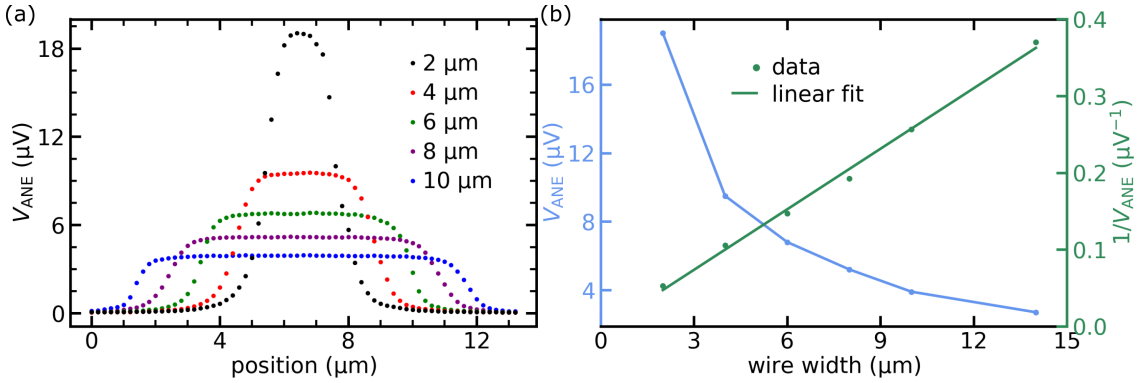

Figure 5.11: (a) ANE line scans across magnetic wires of different widths. (b) The plot of V_{ANE} vs w (blue, left axis), plot of $1/V_{ANE}$ against w, as well as the linear fit(green, right axis).

5.6.2 Dependence on illumination area

We analyze the effect of L_x and L_x on the measured ANE signal. V_{ANE} indicated in Figure 5.12a is the measured ANE signal along the y-direction. From equation (5.9), we have,

$$V_{ANE} = V^y_{meas} \tag{5.10}$$

$$= \frac{L_x}{w} \cdot V^y_{gen} \tag{5.11}$$

$$= \frac{L_x}{w} \cdot E^y_{ANE} \cdot L_y \tag{5.12}$$

$$= \frac{L_x}{w} \cdot \mu_0 \cdot S_{ANE} \cdot \nabla_z T \cdot L_y \tag{5.13}$$

Assuming $\nabla_z T \propto \frac{P}{L_x \cdot L_y}$, where P is the incident laser power,

$$V_{ANE} \propto \frac{L_x}{w} \cdot \mu_0 \cdot S_{ANE} \cdot \frac{P}{L_x \cdot L_y} \cdot L_y \tag{5.14}$$

$$\propto \frac{\mu_0 \cdot S_{ANE} \cdot P}{w} \tag{5.15}$$

Thus, we expect the magnitude of the measured ANE signal to be independent of the heat flux area. To verify this experimentally, we illuminate the magnetic wire with a laser beam with a power of 5 mW. The beam is focused using objective lenses with two different numerical apertures (*NA*) of 0.4 and 0.7. Because the spot size is inversely proportional to *NA*, the heat flux area in the two cases would be different, as indicated in the inset of 5.12b. ANE line scan by these two objective lenses shows that the magnitude of the ANE signal is identical within the experimental errors, confirming our analytical model.

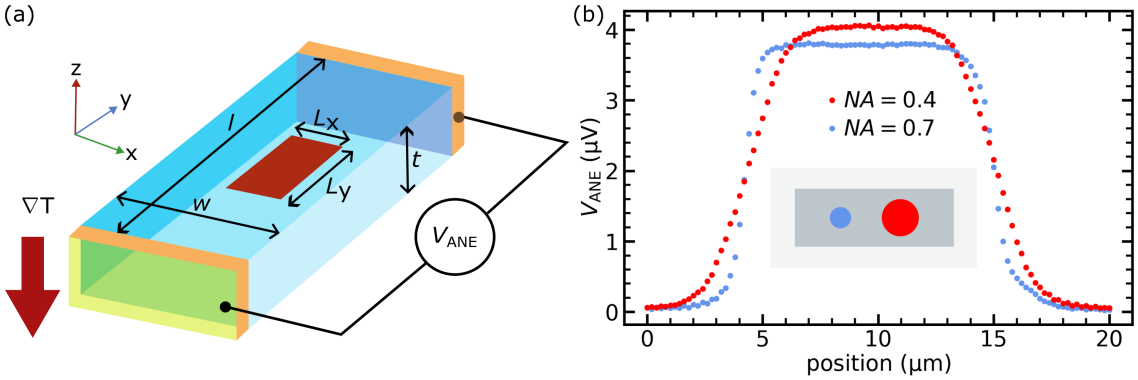

Figure 5.12: (a) Schematic of the measurement geometry. (b) ANE line scan of a magnetic wire by the objective lenses of NA 0.7 and 0.4. The inset schematically shows the relative spot size of the focused laser beam in two cases.

5.7 Generalized expression for ANE Signal in ANE microscope

In the previous Section, we showed that the magnitude of the measured ANE signal, resulting from a uniform $\nabla_z T$ over a dimension of $L_x \times L_y$ is given by equation (5.13). In the SANE microscopy, $\nabla_z T$ underneath the focal spot is a Gaussian distribution. For the case of a nonuniform $\nabla_z T$ like this, we can divide the slab into small parts so that within each part, $\nabla_z T$ is uniform. The net ANE signal would be a summation of the contribution from each part. Consider a magnetic slab of the dimension $l \times w \times t$ (Figure 5.12a) illuminated by a laser beam. We consider a general case of magnetization with both IP (m_x, m_y) and OOP (m_z) components. A temperature gradient $\nabla_x T$ and $\nabla_z T$ induces an electrical response along the slab length (y-direction) due to ANE,

$$E_{\mathrm{ANE}} = \mu \cdot S_{\mathrm{ANE}} \cdot (m_x \nabla_z T + m_z \nabla_x T)\,.$$

We divide the slab region into cubes of dimension $dx \times dy \times dz$ in which the gradient can be assumed constant. The resulting voltage is,

$$V_{\mathrm{ANE}} = E_{\mathrm{ANE}}\, dy = \mu \cdot S_{\mathrm{ANE}} \cdot (m_x \nabla_z T + m_z \nabla_x T)\, dy.$$

These stacks of cubes act as batteries conducting in parallel along the x and z direction and in series along the y direction. The net voltage averages out in x and z directions and adds up in y-direction, giving,

$$V_{\mathrm{ANE}} = \frac{\mu \cdot S_{\mathrm{ANE}}}{w \cdot t} \cdot \left(\int_0^w \int_0^l \int_o^t m_{\mathrm{x}} \nabla_{\mathrm{z}} T \, dxdydz + \int_0^w \int_0^l \int_o^t m_{\mathrm{z}} \nabla_{\mathrm{x}} T \, dxdydz \right).$$

Assuming m_{x} and m_{z} to be uniform across the film thickness of a few nanometers, we have,

$$\int_0^t m_{\mathrm{x}} \nabla_{\mathrm{z}} T \, dz = m_{\mathrm{x}} \int_0^t \nabla_{\mathrm{z}} T \, dz = m_{\mathrm{x}} \cdot (T_{\mathrm{top}} - T_{\mathrm{bottom}}).$$

The temperature across the film thickness is nearly identical, for example, 313.35 K and 313.23 K in Figure 5.4a. $\nabla_{\mathrm{x}} T$ can be assumed to be nearly constant across the film thickness, giving $\int_0^t m_{\mathrm{z}} \nabla_{\mathrm{x}} T \, dz = m_{\mathrm{z}} \nabla_{\mathrm{x}} T t$. Therefore,

$$V_{\mathrm{ANE}} = \frac{\mu \cdot S_{\mathrm{ANE}}}{w} \cdot \left(\frac{1}{t} \cdot \int_0^w \int_0^l m_{\mathrm{x}} \cdot (T_{\mathrm{top}} - T_{\mathrm{bottom}}) \, dxdy + \int_0^w \int_0^l m_{\mathrm{z}} \nabla_{\mathrm{x}} T \, dxdy \right) \quad (5.16)$$

5.8 Estimate of OOP temperature gradient based on ANE

We compute the magnitude of OOP temperature gradient $\nabla_{\mathrm{z}} T$ based on V_{ANE} in a saturated IP magnetized CoFeB film ($m_{\mathrm{x}} = 1, m_{\mathrm{z}} = 0$). Assuming the ANE coefficient to be that of a typical ferromagnet ($\mu S_{\mathrm{ANE}} = 1\,\mu\mathrm{V/K}$), equation (5.16) simplifies to the following:

$$V_{\mathrm{ANE}} = \frac{1\,\mu\mathrm{V/K}}{w} \int_0^w \int_0^l \nabla_{\mathrm{z}} T \, dxdy$$

As we demonstrated previously, $\nabla_{\mathrm{z}} T$ is a Gaussian function of x, y with standard deviation of σ related to FWHM by $\sigma = \frac{FWHM}{2.35}$. Defining to $\nabla_{\mathrm{z}} T^0$ to be the gradient at the center of the of the laser spot,

$$V_{\mathrm{ANE}} = \frac{1\,\mu\mathrm{V/K}}{w} \nabla_{\mathrm{z}} T^0 \int_0^w \int_0^l e^{\frac{-(x^2+y^2)}{2\sigma^2}} \, dxdy$$

Since l, w are much larger than σ, limits in the integration can be considered as $-\infty$ to ∞. Then the value of the integral is $2\pi\sigma^2$,

$$V_{\mathrm{ANE}} = \frac{1\,\mu\mathrm{V/K}}{w} \cdot \nabla_{\mathrm{z}} T^0 \cdot 2\pi\sigma^2 \quad (5.17)$$

In our experiments, we have $V_{\mathrm{ANE}} = 4\,\mu\mathrm{V}$ in a $10\,\mu\mathrm{m}$ wide wire (Figure 5.5a), and $\sigma = \frac{FWHM}{2.35} = \frac{760\,\mathrm{nm}}{2.35} \approx 324\,\mathrm{nm}$ (Figure 5.9). Substituting these values in equation (5.17) gives $\nabla_{\mathrm{z}} T^0 \approx 6 \times 10^6\,\mathrm{K/m}$. We note that the obtained value of $\nabla_{\mathrm{z}} T^0$ based on the experiments (6×10^6 K/m) differs from that obtained from COMSOL simulation (9×10^6 K/m) by a factor of 1.5. This discrepancy is attributed to an error in several parameters, such as ANE (S_{ANE}) and reflection (α) coefficients of the CoFeB film.

5.9 Discussion

Finally, we point out the underlying mechanisms that make ANE microscopy advantageous when studying magnetic materials on the nanoscale. Equation (5.15) indicates that the magnitude of the ANE voltage in a given magnetic wire is proportional to $\frac{P}{w}$. It is independent of all other geometric factors. This result suggests that the laser-based heating utilized in SANE microscopy has two advantages. First, since the voltage is inversely proportional to the wire width, studying narrower wires with ANE microscopy gives rise to larger signals. Second, the entire absorbed energy is utilized to directly heat the wire, in contrast to resistive-heating methods where a majority of the heat energy is dissipated elsewhere [120–122].

5.10 Conclusion

We have demonstrated that laser heating-induced ANE signal can be utilized to characterize the magnetic properties of IP-magnetized materials. Scanning measurements of such an ANE signal provide magnetic domain images. The radial distribution of the OOP temperature gradient follows the intensity distribution of the focused laser beam. This is in contrast to the temperature distribution of the film, which spreads beyond the laser focal spot. For a laser beam having a Gaussian radial intensity distribution with a FWHM of $\approx$735 nm, the OOP temperature gradient is also a Gaussian with a FWHM of $\approx$760 nm. For the wavelength of 532 nm and incident laser power of 5 mW, the amplitude of the OOP temperature gradient Gaussian distribution $\nabla_z T^0$ is $\approx 6 \times 10^6\,\mathrm{K/m}$. We note that laser heating-based ANE studies, in addition to being convenient, have a distinct advantage over resistive heating-based ANE studies.

Chapter 6

SANE imaging with optical near-field

The spatial resolution of the SANE microscopy is constrained by the size of the laser beam focal spot. When an objective lens is utilized, the spot size can not be reduced beyond the diffraction limit of $\lambda/2NA$. For a typical optical microscope, this limit is a few hundred nanometers. An optical probe with nanoscale dimension is required to image the magnetic domains with the SANE microscope at the nanoscale. For that, we utilize an enhanced optical near-field underneath a vibrating metallic tip that is a few nanometers in diameter [51, 52]. In practice, this is achieved by focusing a laser beam to the apex of an atomic force microscope (AFM) tip. The intensity of the enhanced optical near-field depends nonlinearly on the tip-sample distance, which is modulated due to the vibration of the tip. Such modulation and the nonlinear dependence result in higher harmonic components of the near-field enhanced laser beam intensity. In contrast, the non enhanced laser beam away from the tip has only d.c. and the first harmonic component. This allows us to to detect purely nanoscale near-field component by demodulating the signal at higher harmonics of the tip vibration frequency (ω).

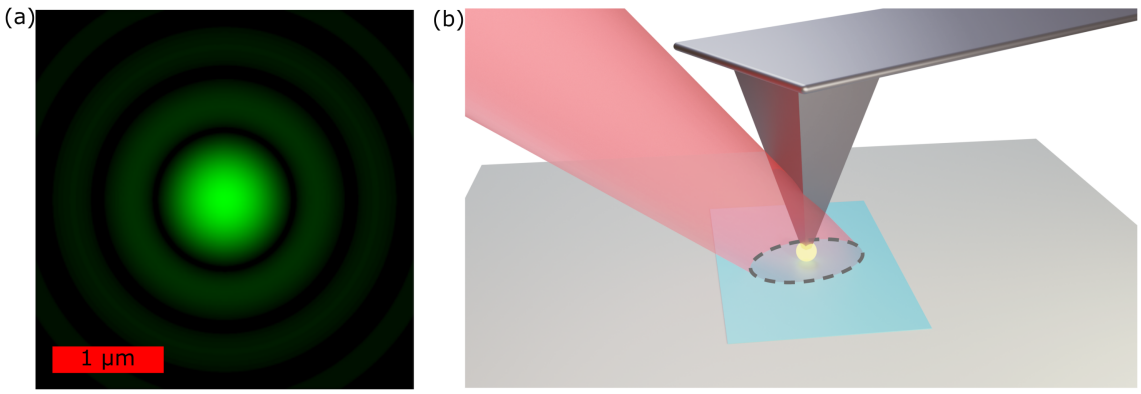

Figure 6.1: (a) The intensity distribution of a laser beam with a wavelength of 532 nm focused by an objective lens with a numerical aperture of 0.9. (b) Illustration of the optical near-field enhancement underneath a vibrating AFM tip.

6.1 Scanning optical near-field microscope

6.1.1 Optical topography

We demonstrate near-field optical imaging with an AFM scan of 5 µm × 5 µm area of a sample consisting of 1.5 µm × 1.5 µm square structures of 20 nm thick SiO_2 deposited on a Si wafer (Figure 6.2a). Simultaneously, the apex of the tip is applied with a laser beam with a wavelength of 8 µm and power of 25 mW. The beam is focused on the sample by a parabolic mirror with a numerical aperture of 0.4. The intensity of the reflected laser beam is measured to construct the optical topography of the structure. The diffraction-limited spot of the focused laser beam is expected to be at least 10 µm. Map of the d.c. reflectivity, probing the optical topography with this 10 µm wide laser spot is not able to resolve 1.5 µm wide structures (Figure 6.2b). The structures are visible with better contrast with the first harmonic reflectivity map (Figure 6.2c). It shows the optical-topography probed by the nanoscale-enhanced optical near-field. However, it also contains additional background noises. The vibration of the tip partially modulates the intensity of the laser beam because the tip lies in the path of the laser beam. This shadowing effect adds to the first harmonic reflectivity in addition to the enhanced optical near-field reflected signal. To get rid of this, we detect reflectivity at the second harmonic of the tip vibration frequency. This signal contains the purely nanoscale near-field component, enabling us to construct well-resolved optical topography of the structures (Figure 6.2d).

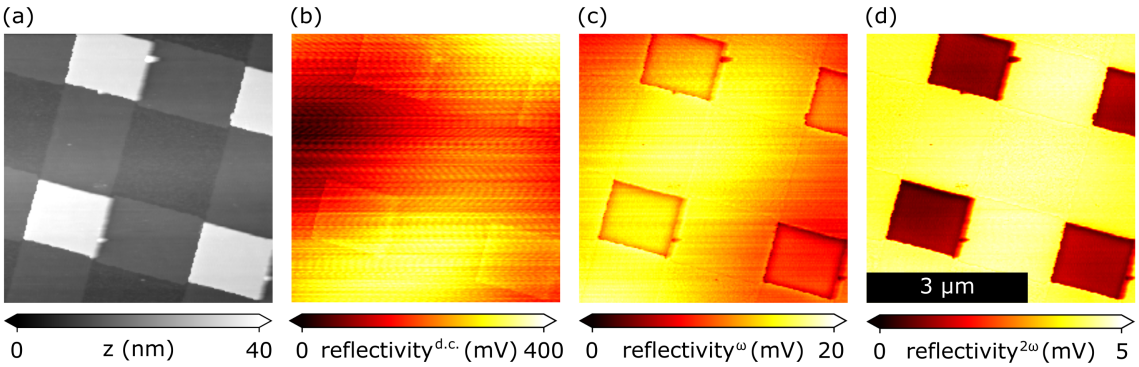

Figure 6.2: (a) AFM scan of 20 nm thick SiO_2 consisting of 1.5 µm × 1.5 µm square structures. (b-d) The optical topography of the same structure constructed with d.c., first and second harmonics component of the reflected laser beam, respectively.

6.1.2 Lateral size of the nanoscale optical near-field enhancement

To estimate the lateral size of the AFM tip apex and the nanoscale near-field, we take a line scan near an edge of 20 nm thick SiO_2. The derivative of the line scan reveals the FWHM of the tip apex to be 30 nm (Figure 6.3). The nanoscale optical near-field enhancement is spread across similar length (≈31 nm).

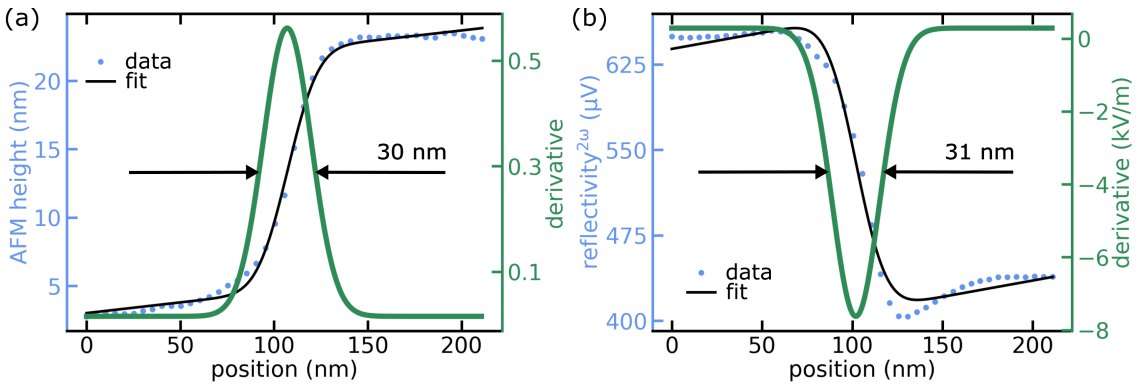

Figure 6.3: (a) AFM line scan near an edge of 20 nm thick SiO_2, a fit to an error function (blue, left axis), and the derivative of the fit to the line scan (right, green axis). (b) Same as in (a) for the simultaneously measured reflectivity at the second harmonics of the tip vibration frequency.

6.2 Laser heating-induced temperature gradient at the nanoscale

We again use COMSOL multi-physics to estimate the spatial and temporal temperature distribution in a CoFeB film subjected to illumination by a nanoscale-sized laser beam. In this case, the laser intensity is modeled as a Gaussian distribution with a FWHM of 30 nm (lateral size of the enhanced optical near-field). The energy density for an absorbed laser power of 3.5 μW is shown in Figure 6.4a. Simulated results show that the nanoscale heating increases the film temperature by ≈0.5 K(Figure 6.4b).

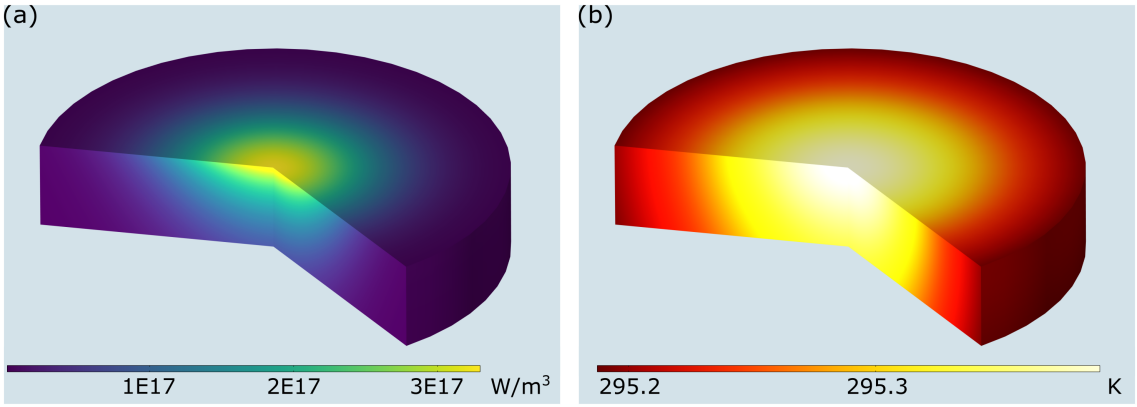

Figure 6.4: (a) Energy density distribution in the CoFeB film from the absorption of 3.5 μw Gaussian laser beam with a FWHM of 30 nm. The distribution is shown for $t = T/4$. (b) The film temperature at $t = T/4$.

6.2.1 Magnitude and time dependence of the nanoscale OOP temperature gradient

We extract a line graph along the film thickness that shows a temperature difference of ≈0.05 K across the 15 nm thick film (Figure 6.5a). This amounts to an OOP temperature gradient of $\nabla_z T = 4 \times 10^6\,\mathrm{K/m}$ at the center of the nanoscale optical near-field. The second harmonics of typical AFM tip vibration frequency is ≈580 KHz. To confirm if modulation of the temperature gradient at this frequency is possible, we show the time

dependence of $\nabla_z T$(Figure 6.5a). It follows laser intensity modulation at ≈580 KHz, implying that heat diffusion is fast enough to modulate the temperature gradient at the second harmonics of the tip vibration frequency.

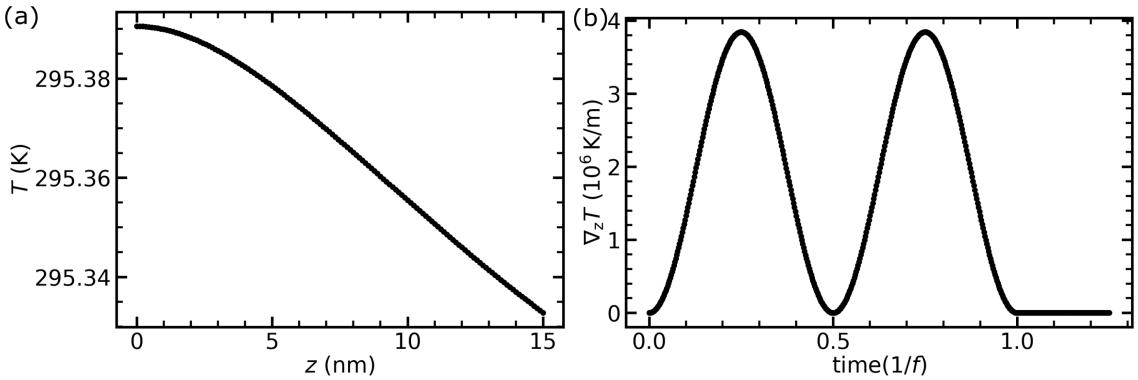

Figure 6.5: (a) Line graph of CoFeB film temperature subjected to laser-induced heating at the nanoscale. (b) Time dependence of OPP temperature gradient $\nabla_z T$.

6.2.2 ANE signal from the near-field induced OOP temperature gradient

We utilize near-field induced OOP temperature gradient for scanning ANE (NF-SANE) measurements. We use a 15 nm CoFeB film patterned into a 2 µm wide wire for this. Since the spatial extent of $\nabla_z T$ in NF-SANE is smaller (nanoscale) relative to that in SANE (micro-scale), the resulting ANE voltage is also expected to be smaller. A narrower wire is utilized to increase the magnitude of the measured ANE voltage (see equation (5.9)). A magnetic field of ±5 mT is applied to saturate the magnetization along the wire

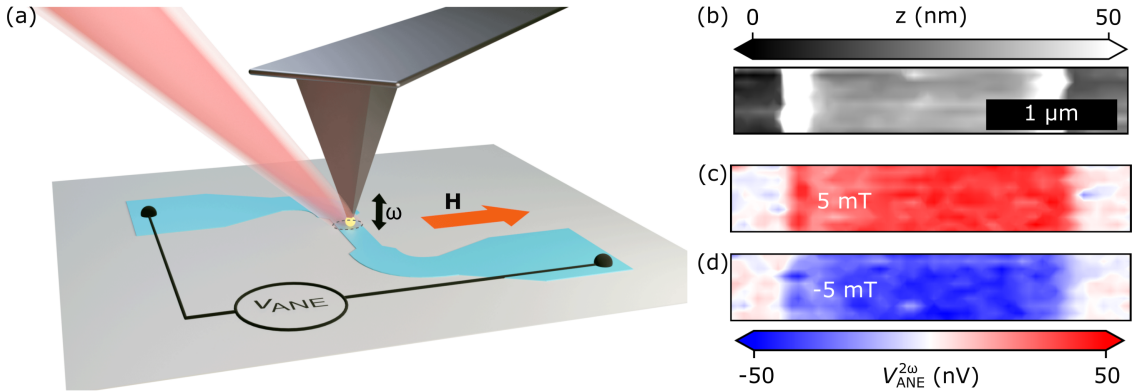

Figure 6.6: (a) Schematic illustration of the NF-SANE method. (b) AFM topographic scan of the CoFeB device showing 2 µm wide wire structure. (c,d) ANE signal is demodulated at the second harmonics of the tip vibration frequency. The two images show scans under the application of a transverse 5 mT and −5 mT magnetic field, respectively.

width (Figure 6.6a). An AFM scan reveals the topography of the device near the wire structure (Figure 6.6b). Simultaneously measured ANE voltage is demodulated at the second harmonics of the tip vibration frequency. The resulting map is shown in Figure 6.6c,d. An ANE signal of ≈40 nV is generated when the tip hits the wire structure. The

magnetic origin of the signal is confirmed by its sign reversal with respect to the direction change of the applied 5 mT magnetic field.

6.3 Radial distribution of nanoscale OOP temperature gradient

6.3.1 Based on the COMSOL simulation

A line graph of the simulated temperature at the two surfaces of the CoFeB film is shown in Figure 6.7a. The radial spread of the temperature is larger than the near-field laser intensity distribution. This is similar to the SANE case. Moreover, the OOP temperature gradient has a FWHM of 38 nm (Figure 6.7b); this is 26% larger than the FWHM of the laser intensity distribution. This result is in contrast to the SANE case, where the difference between the two was only 3%.

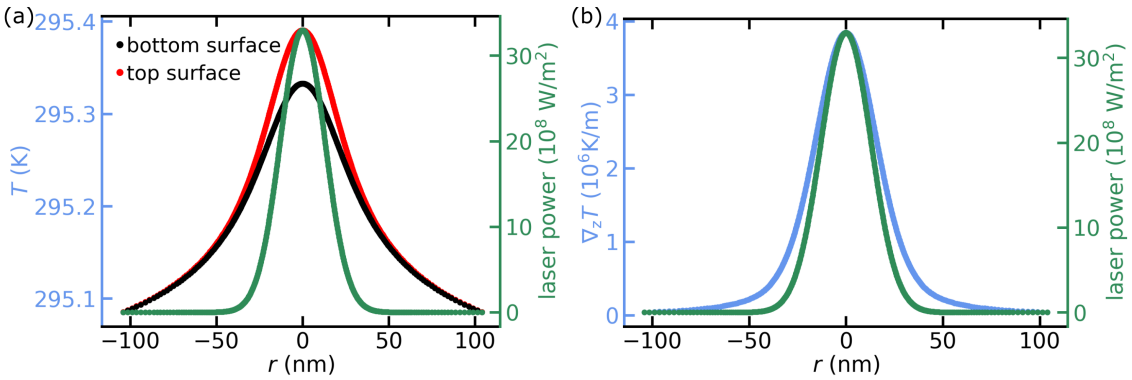

Figure 6.7: (a) Line graph of the simulated temperature distribution in radial direction. The left blue axis shows the temperature at the top and bottom surfaces of the CoFeB film. The right green axis shows the near-field laser intensity distribution in the radial direction. (b) Line graph of OOP temperature gradient in the radial direction (blue, left axis), and laser intensity distribution (green, right axis).

6.3.2 Based on the experimental results

We experimentally determine the radial distribution of nanoscale $\nabla_z T$ by imaging a magnetic structure of the Landau pattern with NF-SANE. For this, we use a $3\,\mu m \times 3\,\mu m$ slab of CoFeB film with a thickness of 45 nm. 500 nm wide contact wire at the top and bottom allows to detect the ANE signal. In comparison to the SANE case, a smaller structure is used here to maximize the magnitude of the measured ANE signal. This structure forms a Landau pattern in the remanent state as shown with the micro-magnetic simulation (Appendix A.5)

6.3.2.1 Imaging magnetic vortex with NF-SANE microscopy

In order to perform NF-SANE-based magnetic domain imaging of the remanent state of the sample, it was mounted to a removable chip carrier (see methods). The chip carrier

was placed near a Neodymium board magnet to saturate the CoFeB slab magnetization along the device width. Removal of the magnet creates the Landau pattern in remanence. Subsequently, the chip carrier was mounted to the AFM stage for the NF-SANE scanning measurement. An AFM scan performed in the step size of 100 nm shows the topography of the CoFeB device structure (Figure 6.8a). The simultaneously measured second harmonics ANE Signal reveals the Landau pattern (Figure 6.8b). A higher pixel density scan (in the smaller step size of 12 nm) surrounding the vortex shows the pattern with better spatial resolution (Figure 6.8c). Here, the magnitude of the ANE signal (≈25 nV) is smaller relative to ≈40 nV in Figure 6.6. This is due to smaller magnetization in the remanent state relative to that of the saturated case in the presence of 5 mT applied magnetic field. The lock-in noise at the detection frequency of ≈580 kHz is 10 nV. Though the SNR of ≈ 2 is low, we have been able to reproduce the observed magnetic patterns. Repetition of the NF-SANE scan surrounding the vortex core (Figure 6.9a) reveals the same pattern as that in Figure 6.8c. Further supporting NF-SANE scans of the Landau pattern are shown in Appendix A.5.

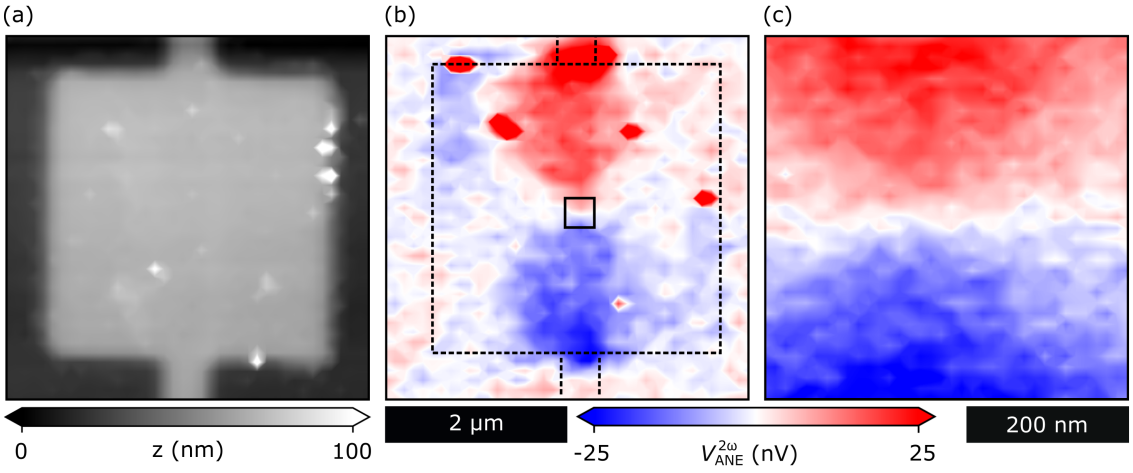

Figure 6.8: (a) AFM height scan of 3 µm × 3 µm CoFeB slab film with a thickness of 45 nm. The slab is fashioned with 500 nm wide contact wires at the top and bottom. (b) Simultaneously measured second harmonic ANE signal, revealing the landau pattern. The outline of the device structure is shown with the dotted lines. (c) A higher resolution NF-SANE scan in the region is shown by the inner square in (b).

6.3.3 NF-SANE line scan across the magnetic vortex

To determine the radial distribution of $\nabla_z T$, we take an ANE line scan through the vortex core along the y-direction. The line scan is then fitted to an error function, following the same procedure as in Figure 5.9. The derivative of the line scan reveals the distribution of $\nabla_z T$ to be a Gaussian with a FWHM of 76 nm. A line extract from the different sets of measurements reveals a similar FWHM of 74 nm (see Appendix A.5), confirming the reproducibility of the results. Thus, we conclude that the radial distribution nanoscale $\nabla_z T$ to be a Gaussian with FWHM of ≈75 nm. This is larger than the expected value of 38 nm from the simulation results (Figure 6.7). The simulation was performed for a new

AFM tip that had an apex with a FWHM of 30 nm. As the tip is utilized for the AFM measurements, it gets broader. The higher FWHM of $\nabla_z T$ is attributed to the broadening of the tip.

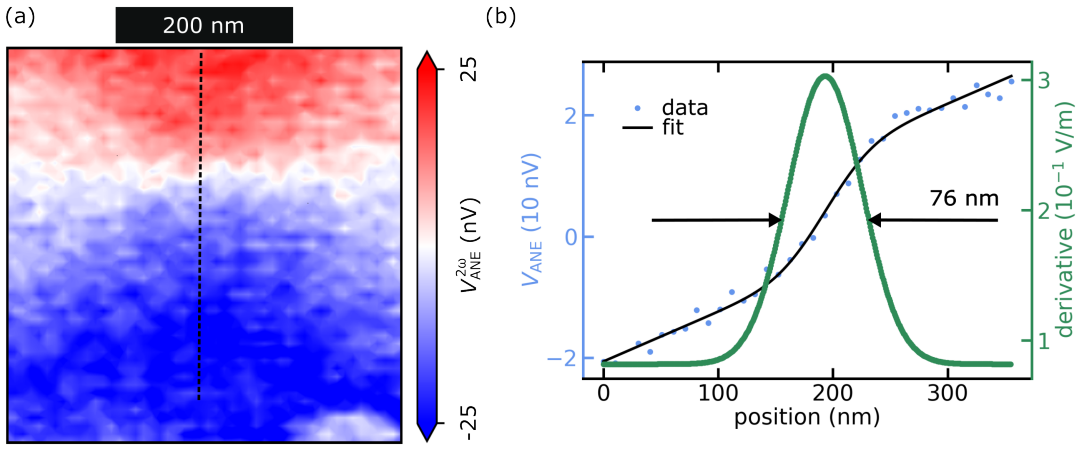

Figure 6.9: (a) Repetition of the NF-SANE scan around the vortex core of the landau pattern shown in Figure 6.8c. A line graph extracted along the dotted line in (a), a fit of the line scan to an error function (blue, left axis), and the derivative of the fit to the line scan(right, green axis).

6.4 Conclusion

We demonstrated the magnetic origin of the optical near-field heating-induced ANE signal and imaged a well-known magnetic texture of a Landau pattern with the nanoscale spatial resolution. Based on COMSOL simulation, we expect the lateral size of the OOP temperature gradient to be only 25% higher than that of the optical near-field. In our measurements, we find the radial distribution of the nanoscale OOP temperature gradient to be a Gaussian with a FWHM of ≈75 nm.

Chapter 7

SANE imaging for OOP magnetization

In the previous two Chapters, we showed that ANE voltage generated by an OOP temperature gradient can be utilized to probe the IP-magnetization of a magnetic sample. Optical near-field induced laser heating allows to perform spatially resolved ANE measurements at the nanoscale. ANE signal has also been used to characterize the OOP-magnetized samples by measuring the ANE voltage generated by the IP temperature gradient (Figure 7.1). However, reports on spatially resolved ANE measurement in OOP-magnetized material are very limited [56, 58, 61]. Some reports suggest that the ANE response of laser heating-induced IP temperature gradient is negligible [60]. Here, we systematically study the nature of laser heating-induced IP temperature gradient and show that it can be utilized to image magnetic domains in OOP-magnetized magnetic nanowires.

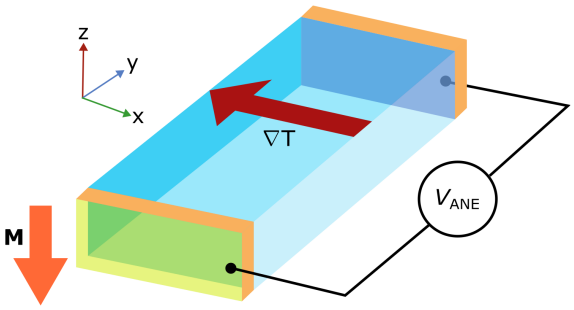

Figure 7.1: Schematic illustration of the ANE method for OOP-magnetized samples: The sample is magnetized OOP, as shown by the orange arrow. An IP temperature gradient is created along the wire width (shown by the red arrow). The ANE response generated transverse to both the gradient and the magnetization is measured along the wire length.

7.1 Laser heating-induced IP temperature gradient

We demonstrated that radial intensity distribution at the laser focal spot is a Gaussian. That would mean that laser heating is higher at the focal spot center that decays away from the center. This would result in an IP temperature gradient.

7.1.1 Spatial distribution of the IP gradient

To understand the nature of the IP gradient, we show the simulated results for the radial distribution of the temperature subjected to near-field heating (Figure 7.2a). Its spatial derivative gives us the radial distribution of the IP temperature gradient ($\nabla_x T$) (Figure 7.2b). The gradient is spatially nonuniform and asymmetric about the laser spot center.

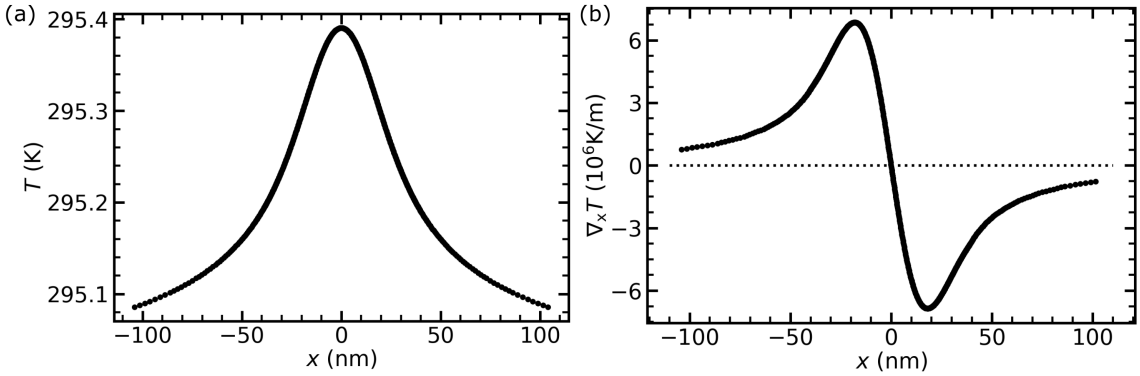

Figure 7.2: (a) Line extract from Figure 6.4b showing the film temperature in the x-direction. (b) The IP temperature gradient in the x-direction obtained by numerically computing the spatial derivative of the film temperature in (a).

7.1.2 Magnitude of the IP gradient

Since $\nabla_x T$ is an odd function of x, the average IP temperature gradient is expected to be zero. However, the maximum value of the IP gradient is $\approx 7 \times 10^6$ K/m, which is larger than the average OPP temperature gradient (Figure 6.5).

7.2 ANE signal from laser heating-induced IP temperature gradient

We use the generalized equation (5.16) to deduce the expression for the ANE signal that is generated by a spatially nonuniform IP temperature gradient. For OOP-magnetized sample M_x is zero, this leaves with only one term in equation (5.16) as follows:

$$V_{\mathrm{ANE}} = \frac{\mu \cdot S_{\mathrm{ANE}}}{w} \int_0^w \int_0^l m_z \nabla_x T(x,y)\, dxdy \tag{7.1}$$

While $\nabla_x T(x,y)$ is an odd function of x with respect to the laser spot center, it's an even function of y that decreases in magnitude when moving away from the center, similar to the radial distribution of $\nabla_z T$. For the simplification and qualitative analysis, we assume $\nabla_x T(x,y)$ is nonzero only over a distance of l_{spot} in the y-direction, with a constant value of $\nabla_x T(x)$, simplifying equation (7.1) as follows:

$$V_{\mathrm{ANE}} = \frac{\mu_0 \cdot S_{\mathrm{ANE}} \cdot l_{\mathrm{spot}}}{w} \int_0^w m_z \nabla_x T(x)\, dx \tag{7.2}$$

For the further analysis we consider two separate cases as following:

1. **Uniform m_z underneath the laser spot**: In this case, equation (7.2) can be further simplified,

$$V_{ANE} = \mu_0 \cdot S_{ANE} \cdot l_{spot} \cdot m_z \cdot \nabla_x^{avg} T \tag{7.3}$$

   Where $\nabla_x^{avg} T = \int_0^w \frac{\nabla_x T}{w} dx$ is the average IP temperature in the x-direction across the wire width. When the laser spot completely illuminates the magnetic film, $\nabla_x^{avg} T$ is zero (Figure 7.3a). In this case, no ANE signal is expected. However, partially illuminating the film at the edges gives nonzero $\nabla_x^{avg} T$ with an opposite sign at the two edges (Figure 7.3b). Here, we expect a nonzero ANE signal that is proportional to m_z.

2. **A magnetic domain wall underneath the laser spot:** When m_z underneath the laser spot is nonuniform, the ANE signal depends on the spatial distribution of m_z. It is to be calculated using equation (7.2). For the qualitative analysis, we consider the simpler case when the middle of the laser spot lies on a domain wall. behavior the spot with $\nabla_x^{avg} T = DT$ illuminates the magnetic region with $m_z = 1$, and the right half of the spot with $\nabla_x^{avg} T = -DT$ illuminates the magnetic region with $m_z = -1$ (Figure 7.3c). In this case, the net ANE signal would be an average of the ANE signal generated by two regions:

$$V_{ANE} = \frac{\mu_0 \cdot S_{ANE} \cdot l_{spot} \cdot 1 \cdot DT + \mu_0 \cdot S_{ANE} \cdot l_{spot} \cdot -1 \cdot -DT}{2} \tag{7.4}$$

$$= \mu_0 \cdot S_{ANE} \cdot l_{spot} \cdot DT \tag{7.5}$$

   From Equation (7.5), we expect a positive ANE signal in this case. Similarly, for the case in Figure 7.3d, $V_{ANE} = -\mu_0 \cdot S_{ANE} \cdot l_{spot} \cdot DT$ would be negative.

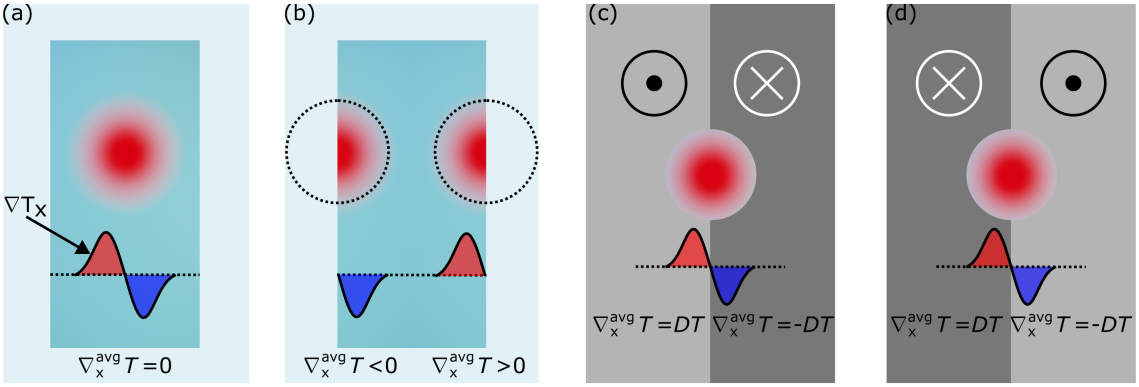

Figure 7.3: (a) Schematics showing a laser beam illuminates the middle region of a magnetic thin film. (b) The beam illuminates the film partially at the two edges. (c,d) The center of the laser spot lies on a magnetic domain wall. behavior the laser spot illuminates the magnetic region with $m_z = 1$ in (c) and with $m_z = -1$ in (d).

7.3 NF-SANE imaging of an OOP-magnetized sample

To verify the assertions in section 7.2, we study an OOP-magnetized film with the NF-SANE microscopy.

7.3.1 Sample characterization

We use a Co/Ni multi-stack film sputter deposited on a sapphire substrate (see methods for details). The film has a perpendicular magneto anisotropy, as shown by the magnetic characterization using vibrating sample magnetometry. It shows hysteresis behaviour in an OOP-applied magnetic field with a coercivity of ≈8 mT (Figure 7.4b).

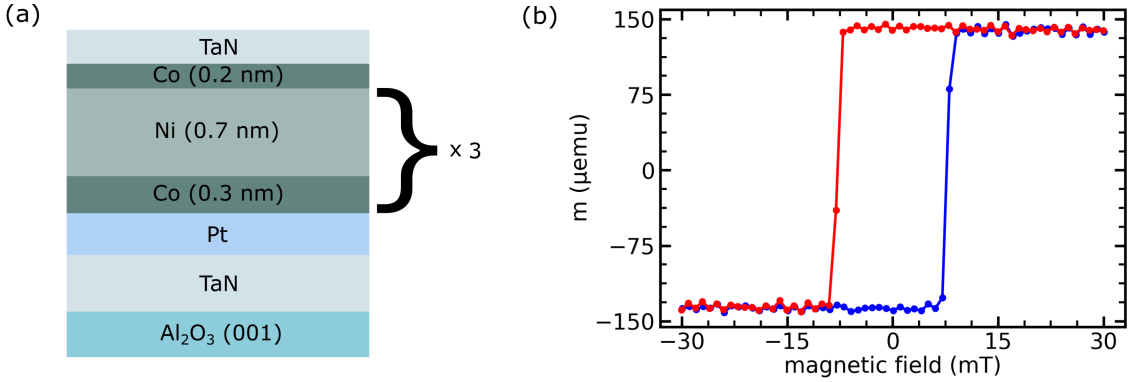

Figure 7.4: (a) Schematic of the Co/Ni multi-stack. (b) VSM measurements of the Co/Ni multi-stack film in an OOP applied magnetic field.

7.3.2 NF-SANE scanning measurements

In order to perform electrical measurements, the film is patterned into a device structure having a 700 nm wide nanowire structure. Applying a decaying a.c. magnetic field creates a multi-domain state in the remanence. The nanowire section of the device contains four domain walls, as shown by the polar Kerr microscope (Figure 7.5a). Subsequently, the same magnetic structure is investigated with the NF-SANE microscopy. First, we analyze the region surrounding the domain wall #2, as shown schematically in Figure 7.5c. Different regions of interest are marked as R1-R6. R1 and R3 are characterized by magnetic regions with the magnetization pointing upwards. This gives a negative ANE voltage due to a negative $\nabla_x^{avg} T$ in R1 that lies at the left edge, and a positive ANE voltage due to a positive $\nabla_x^{avg} T$ in R3 at the right edge (Figure 7.5c). The magnetization points downwards in R2 and R4. The sign of the ANE signal in the region R4 is opposite to that in the region R3 due to the opposite sign of the magnetization, the same is the case between the region R1 and the region R2. This shows that we observe an ANE signal at the edges of the OOP-magnetized nanowires that is proportional to the magnetization. Region R6 contains a magnetic domain wall; here, the left part of the laser spot with a positive $\nabla_x^{avg} T$ partially illuminates the region with the magnetization pointing upwards, and the right

part of the spot with a negative $\nabla_x^{avg} T$ illuminates the region with downward magnetization. This is similar to the scenario depicted in Figure 7.3c. We observe a positive ANE signal in the region R6 as expected. NF-SANE scan in the larger part of the nanowire containing domain wall #2 and #3 is shown in Figure 7.5d. Domain wall #3 has a change in magnetization from downwards to upwards across the nanowire width, similar to the case in Figure 7.3d. We observe a negative ANE signal at this domain wall, as expected.

Magnetic nanowires utilized in commercial devices contain multi-domain states of OOP-magnetized materials. Along the length of the nanowire, they have the regions of uniformly magnetized upwards and regions of uniformly downwards magnetized state separated by domain walls. It is crucial to map out these multi-domain states. For such cases, we can numerically integrate the observed ANE signal across the wire width to obtain a signal that is proportional to the magnetization. The result of this procedure is shown in the grey scale images Figure 7.5e,f, directly reflecting the domain structure in the wire.

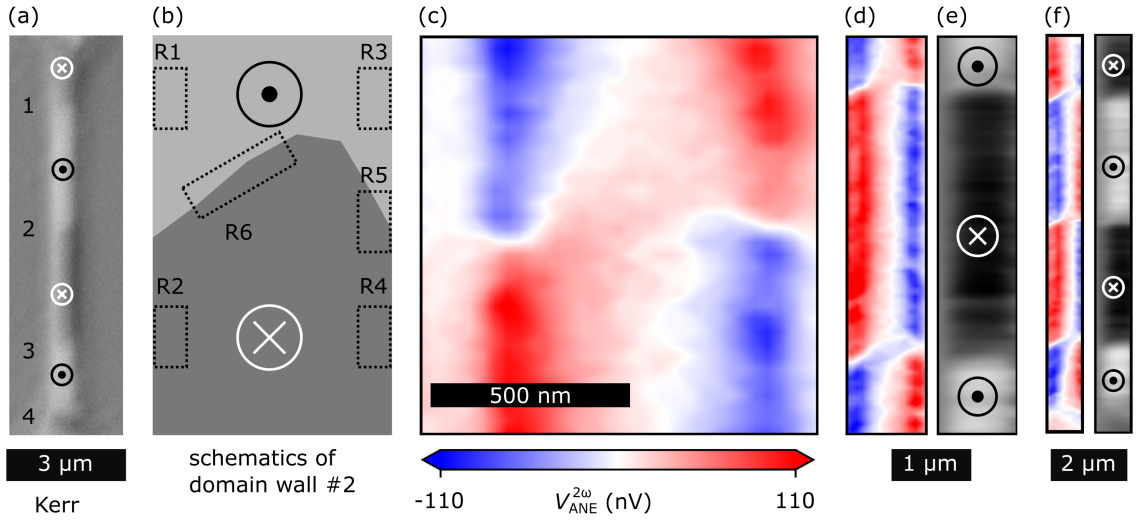

Figure 7.5: (a) Multi-domain state of PMA sample shown with the polar Kerr microscope. The nanowire section of the device consists of 4 domain walls marked as 1 to 4. (b) Schematic illustration of the magnetic states in the region surrounding the domain wall #2. (c) A NF-SANE scan of the magnetic nanowire in the region shown in (b). (d) A NF-SANE scan of the nanowire in the region surrounding the domain walls #2 and #3. (e) ANE signal in (d) is integrated along the wire width. (f) Same as (d,e) for the NF-SANE scan across the full length of the magnetic nanowire.

Finally, we discuss region R5, consisting of a domain wall along the wire length at the right edge. Since at the edges, the ANE signal is directly proportional to the OOP magnetization; we make an ANE line scan to determine the spatial distribution of the temperature gradient similar to Figure 6.9. We thereby find a spatial resolution of 66 nm for the NF-SANE microscope (Figure 7.6a).

In order to further confirm that the observed contrast with NF-SANE corresponds to the magnetic domain structure of the nanowire, we created a different magnetic domain structure in the nanowire, as shown with the polar Kerr microscope in Figure 7.6b. Sub-

sequent scan with the NF-SANE reveals the same magnetic domain structure as the one observed by the Kerr microscope Figure 7.6c,d.

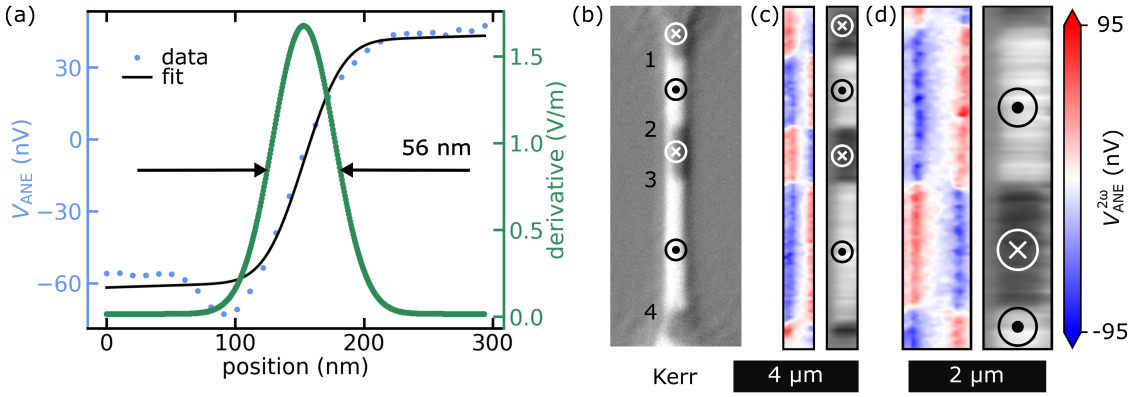

Figure 7.6: (a) ANE line scan in y direction in the region R5 (blue data points), a fit to an error function (black line), and the derivative of the fitted line scan (the left, blue axis). (b) A different multi-domain state created in the same PMA sample is shown with the polar Kerr microscope. Here also, the nanowire section of the device consists of 4 domain walls marked as 1 to 4. (c,d) NF-SANE measurements of the same magnetic structure. The measurements performed in the full wire length are shown in (c), while a higher pixel density scan in the region consisting of domain walls #1, #2,#3 is shown in (d).

7.4 Conclusion

We have demonstrated the applicability of SANE imaging for mapping magnetic domains in OOP-magnetized materials. We observe an ANE signal near the edges of the wire structures that is proportional to OOP magnetization. This results from a net average IP temperature gradient due to partial illumination of the wire structure at the edges. The average net IP temperature gradient vanishes when going away from the edges at a distance larger than the laser focal spot size. Here, no ANE signal is expected from a uniform magnetization. However, a nonuniform magnetization results in a nonzero ANE signal that relates to the magnetization gradient. This signal can be used to image magnetic domain structures similarly as it has been done with the Lorentz force-based transmission electron microscopy [123–125].

Part III

Noncollinear antiferromagnets

Chapter 8

Field-induced switching in NCAF

In the previous three Chapters, we demonstrated how the Berry curvature-driven ANE response can be utilized to detect the magnetic state of a ferromagnet. Studying well-understood magnetic structures of ferromagnets allowed us to infer the characteristics of these newly established measurement techniques. Here, we extend the method to non-collinear antiferromagnets for visualizing magnetic domains in a thin film of Mn_3Sn. As discussed in Chapter 2, applying a magnetic field in the Kagome plane Mn_3Sn allows to manipulate its magnetic ordering with six remanent states. These states can be characterized by a magnetic order parameter vector. We visualize field-induced switching into these different remanent states by detecting two orthogonal components of the order parameter vector. While such studies had previously been performed at the micrometer scale [55, 56], our analysis at the sub-micrometer resolution indicates that the method is affected by a nonmagnetic signal. We identify the source of such a nonmagnetic background and verify the extracted magnetic signal with the MOKE measurements. We use an optical-near-field to visualize the switching down to the nanoscale regime. Here, we observe that the magnetic contrast is spatially nonuniform, with some regions showing negligible magnetic signals. A similar observation was made in another contemporary work [60] that attributed these nonswitching regions corresponding to magnetic domains with a perpendicular magnetic anisotropy. Our detailed analysis indicates that such a spatially nonuniform magnetic contrast results from domain pinning.

In the first Section, we briefly mention a few relevant characteristics of the sample being studied. This is followed by details of the method for detecting magnetic states of Mn_3Sn using an ANE signal. A systematic ANE study showing the effect of the film temperature and magnetic field strength is discussed in the third Section. Magnetic domain imaging experiments at the sub-micrometer and nanoscale regimes are shown in the next two Sections.

8.1 Sample characterization

We demonstrate the magnetic field-induced switching in a NCAF by utilizing a 60 nm thick Mn_3Sn film grown on a MgO (111) substrate (see methods for the growth details).

A 4 nm thick Ru buffer layer was used that establishes an epitaxial growth of the Mn_3Sn films. We perform XRD 2θ- and ϕ-scans to verify a well-ordered and epitaxial growth of the film. Here, θ refers to the angle of the incident X-ray beam with respect to the plane of the sample, and ϕ is the in-plane angle of the beam (see methods Section 3.6). The XRD 2θ-scan of the film shows that only the (000L) family of the peaks are present for Ru and Mn_3Sn, implying a c-axis growth (Figure 8.1a). Moreover, the azimuthal ϕ-scan shows a six-fold symmetry for Ru and Mn_3Sn (Figure 8.1b), as expected for a hexagonal crystal structure. This six-fold symmetric ϕ-scan confirms the well-ordered orientation of the grains and an epitaxial relation between Ru and Mn_3Sn.

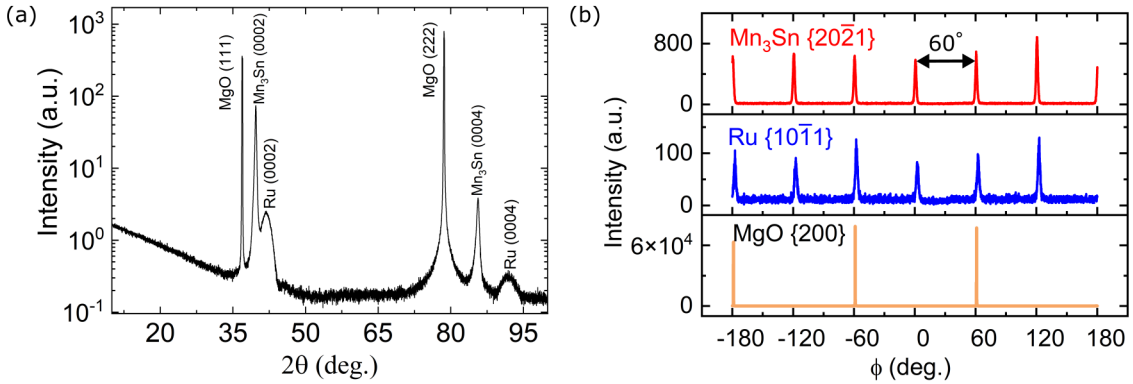

Figure 8.1: (a) XRD 2θ scan of the Mn_3Sn film with a Ru buffer layer grown on a MgO (111) substrate. (b) Azimuthal ϕ-scans of the MgO$\{200\}$, Ru$\{10\bar{1}1\}$, and $Mn_3Sn\{20\bar{2}1\}$ peaks.

8.2 ANE-based readout for the NCAFs

For the ANE-based magnetic characterization of FMs, an ANE response originating from off-diagonal elements of the anomalous Nernst conductivity tensor was utilized. In analogy to FMs, where the magnetization is a symmetry-breaking order parameter, the transport response of the NCAFs can be determined in terms of a cluster octupole moment, as theoretically demonstrated by Suzuki et al. [93]. We investigate six remanent magnetic states of Mn_3Sn as described in Section 2.2.3. ANE response of these magnetic states is determined by an associated magnetic order parameter that we show in the next subsection.

8.2.1 Magnetic order parameter for the noncollinear antiferromagnets

For our c-axis oriented film, the Kagome plane of Mn_3Sn lies in the plane of the film, which is sketched in a top view as shown in Figure 8.2. As discussed in Chapter 2 the moments of the Mn atoms rotate following a magnetic field applied in the Kagome plane. Three easy axes allow for six different magnetic states in remanence marked by MS1$\pm$, MS2$\pm$, and MS3$\pm$ (Figure 8.2). The magnetic space groups for MS1+ with clusters of magnetic octupole moments are the same as those of a ferromagnet with magnetization along $\hat{\mathbf{x}}$ [93]. Therefore, the transport response of MS1+ would be similar to that of

a ferromagnet magnetized along the positive x-direction (see Section 2.4). Similarly, five other remanent states can be characterized by an associated magnetic octupole order parameter (MOOP) vector as indicated by the respective arrow directions (Figure 8.2).

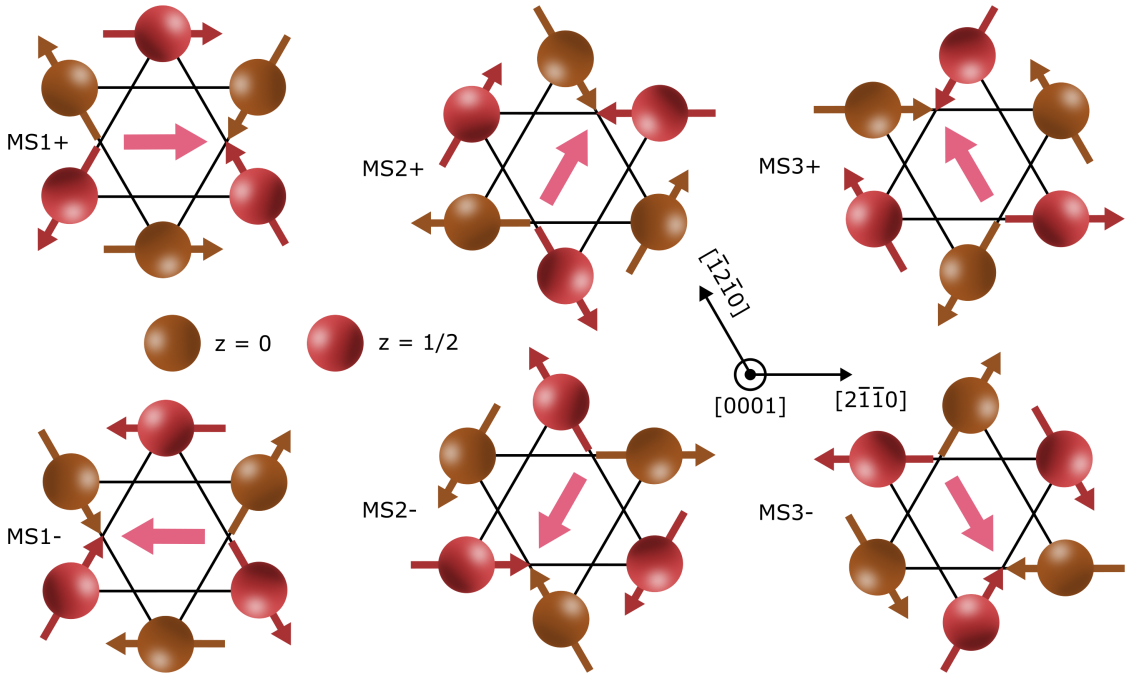

Figure 8.2: Top view of the Mn_3Sn crystal structure showing Mn atoms at z=0 and z=1/2 planes. The wider arrows show the associated MOOP vector for the six different remanent magnetic states of Mn_3Sn.

8.2.2 Magnetic octupole order parameter driven ANE response in NCAFs

In terms of the MOOP vector (**M**), the ANE-induced electrical response can be written as the following:

$$\mathbf{E}_{\mathrm{ANE}} \propto \nabla T \times \mathbf{M} \tag{8.1}$$

For our c-axis oriented film, the MOOP is IP-polarized ($\mathbf{M} = M_x\hat{\mathbf{x}} + M_y\hat{\mathbf{y}}$); thus, the IP component of $\mathbf{E}_{\mathrm{ANE}}$ is generated by only OOP temperature gradient $\nabla_z T$, given as,

$$\mathbf{E}_{\mathrm{ANE}} \propto M_y \cdot \nabla_z T \cdot \hat{\mathbf{x}} + M_x \cdot \nabla_z T \cdot \hat{\mathbf{y}} \tag{8.2}$$

To measure the ANE response, the Mn_3Sn film is patterned into a 10 µm wide wire (Figure 8.3b). A laser beam with a power of 1 mW and a wavelength of 532 nm is focused on the wire using an objective lens (Figure 8.3b). The resulting ANE response is detected by measuring the ANE-induced voltage in the wire oriented along the y-direction (V_y),

$$V_y \propto M_x \cdot \nabla_z T \tag{8.3}$$

Thus, the measurement of V_y allows us to deduce the x-component of the MOOP vector (M_x). A magnetic field (**H**) is applied along the x-direction to switch the MOOP vector along the x-direction (Figure 8.3c).

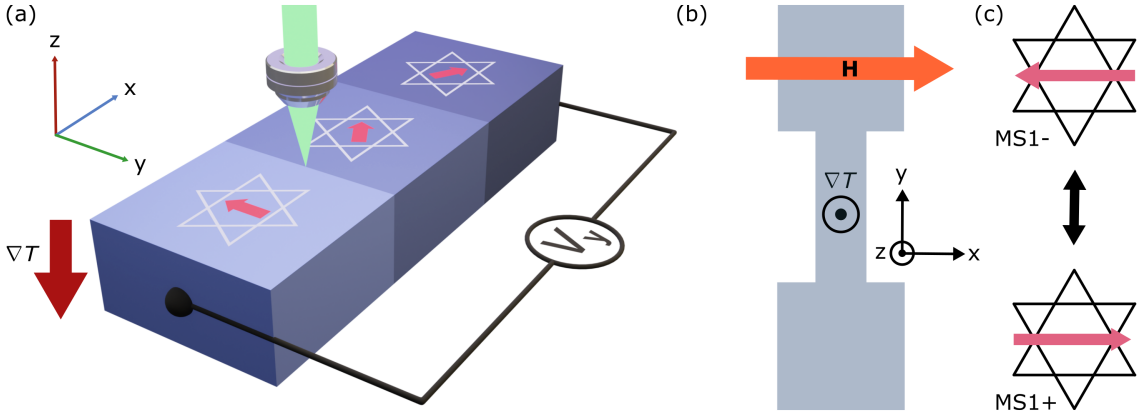

Figure 8.3: (a) Illustration of the ANE microscope: ANE response generated by a laser heating-induced OOP temperature gradient is used to sense the IP-polarized MOOP. (b) Schematic of the device structure and a magnetic field applied along the wire width. (c) Effect of an applied magnetic field along $\hat{\mathbf{x}}$ and -$\hat{\mathbf{x}}$ on the MOOP orientation.

8.3 Role of heating in switching of NCAFs

In the first set of measurements, we study the effect of the magnetic field strength and the film temperature on the switching efficiency. Our optical setup limits us by the field strength of 900 mT. The coercivity of our Mn_3Sn sample is expected to be larger than 1 T [55], resulting in a negligible switching with an applied field of up to 900 mT. However, at an elevated temperature of 125 °C, a significant switching is observed in a Mn_3Sn film grown using similar growth parameters [55]. We measure V_y at the film temperature T and in the presence of a field H applied along $\hat{\mathbf{x}}$. We define a switching parameter in % as (ξ),

$$\xi^{+}(H,T) = \frac{V_y(H,T) - V_y(-900\,\mathrm{mT}, 125\,^{\circ}\mathrm{C})}{V_y(900\,\mathrm{mT}, 125\,^{\circ}\mathrm{C}) - V_y(-900\,\mathrm{mT}, 125\,^{\circ}\mathrm{C})} \times 100 \tag{8.4}$$

$\xi^{+}(H,T)$ reflects the switching effect of a positive applied field H applied at the film temperature of T. Before each measurement, the MOOP vectors were aligned along $-\hat{\mathbf{x}}$ by applying a –900 mT field at 125 °C. The switching is normalised with respect to the switching induced by a 900 mT field at 125 °C. Similarly, the effect of a negative field H at the film temperature of T is studied in terms of ξ^{-} defined as,

$$\xi^{-}(H,T) = \frac{V_y(H,T) - V_y(900\,\mathrm{mT}, 125\,^{\circ}\mathrm{C})}{V_y(900\,\mathrm{mT}, 125\,^{\circ}\mathrm{C}) - V_y(-900\,\mathrm{mT}, 125\,^{\circ}\mathrm{C})} \times 100 \tag{8.5}$$

Here, the MOOP vectors were aligned along $\hat{\mathbf{x}}$ before each measurement. $\xi^{\pm}$ as a function of H,T is shown with a phase diagram in Figure 8.4a. The phase diagram depicts that the coercivity is reduced to ≈200 mT at 125°, it increases at lower temperatures and reaches

a value larger than 1T at 90 °C. We study switching induced by 900 mT for a broader temperature range. It induces negligible switching at room temperature (Figure 8.4b). The switching percentage increases with temperature and saturates at 125 °C, which is close to the Néel temperature of Mn_3Sn (150 °C). Thus, the magnetic state defined by cooling the film from 125 °C to room temperature in the presence of an applied field is expected to be stable, i.e. the magnetic state read at zero field and at room temperature after following this field cooling procedure would be the same as the one in the presence of the magnetic field at 125 °C.

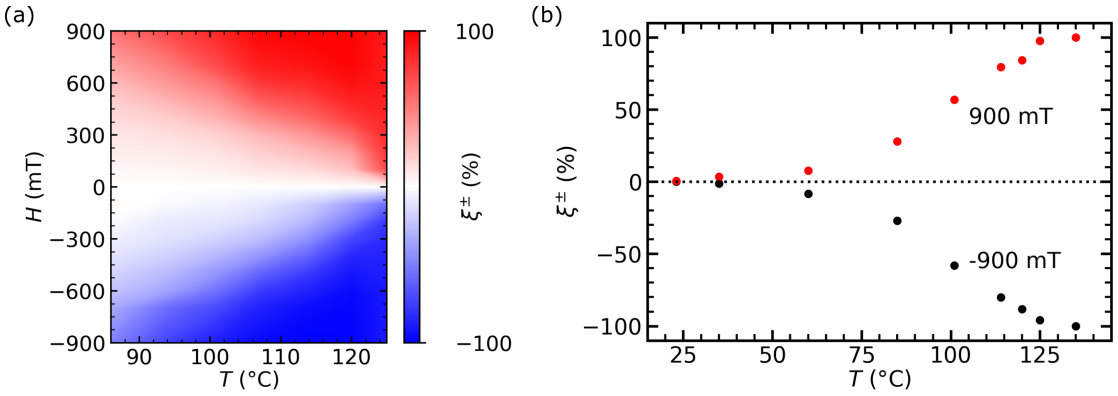

Figure 8.4: (a) Phase diagram showing switching percentage at different applied magnetic fields and the film temperature. (b) Switching percentage induced by applying a 900 mT at the different films temperature.

8.4 Magnetic domains in NCAFs at the sub-micrometer scale

We perform spatially resolved SANE measurements to visualise magnetic domains in our Mn_3Sn devices. Magnetic domains are imaged after field cooling the film in the presence of ±1.3 T magnetic field. This field cooling procedure switches the MOOP vector along $\hat{\mathbf{x}}$ and $-\hat{\mathbf{x}}$ for the applied field of 1.3 T and −1.3 T. The switching is reflected in the sign reversal of the measured voltage V_y in the majority of the region(Figure 8.5a,b). There are small areas where the sign of V_y is insensitive to the field direction. We attribute these regions with the field-independent signal to be the regions with a grain boundary or the regions with domain pinning. Domain pinning would result in a field-independent ANE voltage (V_{ANE}^{FI}), while grain boundaries result in a nonmagnetic Seebeck-effect (SE) voltage (V_{SE}^{NM}) [60], see Appendix A.2, B.2. The magnetic field-dependent ANE signal (V_{ANE}^{M}) can be separated by subtracting two images where the MOOP is field polarized in opposite directions (Figure 8.5c). Similarly, by adding these images, we obtain a spatial map of the field-independent contributions (Figure 8.5d). The resulting map reveals that there is a significant field-independent contribution ($V^{FI} = V_{ANE}^{FI} + V_{SE}^{NM}$). It is present throughout the wire structure, and its signal polarity is bipolar. V^{FI} is superimposed with V_{ANE}^{M} in the measured voltage V_y. When the device is field cooled in the presence of a positive (negative) field, the magnetic order switching results in red (blue) contrasts in the

majority of the regions where $V^{\mathrm{M}}_{\mathrm{ANE}}$ is larger than V^{FI}, except in small regions where the magnitude of V^{FI} is relatively higher. Previously, similar SANE imaging measurements

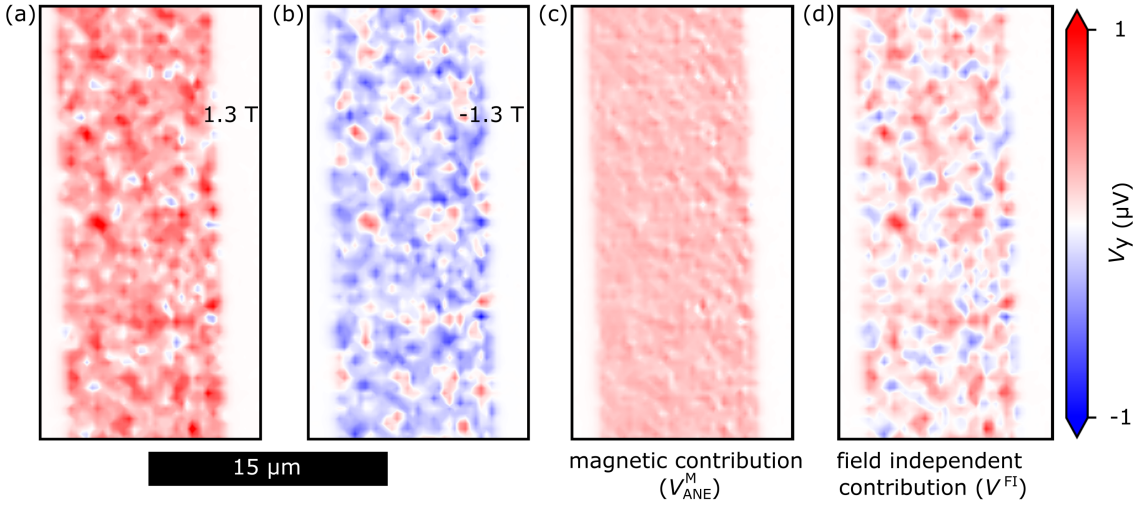

Figure 8.5: (a,b) Spatially resolved scanning ANE measurements of in Mn_3Sn wire structure after field cooling the device in the presence of ±1.3 T magnetic field, respectively. These measurements were performed by scanning the wire structure underneath a laser beam focused using an objective lens with a numerical aperture of 0.7. (c) V_y in (b) at each pixel is subtracted from that in (a). Before the subtraction, the two images were carefully aligned. The subtracted value at each pixel is divided by two. (d) V_y in (a,b) are averaged at each pixel.

were performed to observe field-induced switching in Mn_3Sn at the micrometre scale [55, 56]. Our analysis at the sub-micrometer scale reveals that the method is affected by a field-independent nonmagnetic signal contribution in addition to the magnetic contrast. We verify the magnetic contribution by constructing a hysteresis loop based on the ANE signal and comparing it with the hysteresis loop obtained using longitudinal MOKE.

We perform an ANE scan over a $10\,\mu m \times 20\,\mu m$ area of the wire at different applied fields and at the film temperature of 125 °C. The laser beam is focused with the NA=0.4 objective lens to minimise the field- and temperature-induced drifts. A smaller NA lens provides a larger spot size, thus requiring a smaller number of measurements steps that reduces the measurement time. At an applied field of −900 mT, the MOOP vectors are oriented along $-\hat{\mathbf{x}}$ (Figure 8.6a). The MOOP vectors retain this orientation in the remanence with a reduced ANE signal (Figure 8.6b). As the field along $\hat{\mathbf{x}}$ is increased in magnitude, the MOOP vectors gradually reorient along $\hat{\mathbf{x}}$ (Figure 8.6c,d,h,g,f). The domains retain this orientation even when the field is reduced in strength (Figure 8.6e). A field along $-\hat{\mathbf{x}}$ with increasing strength gradually reorients the MOOP vector along $-\hat{\mathbf{x}}$ (Figure 8.6i-l).

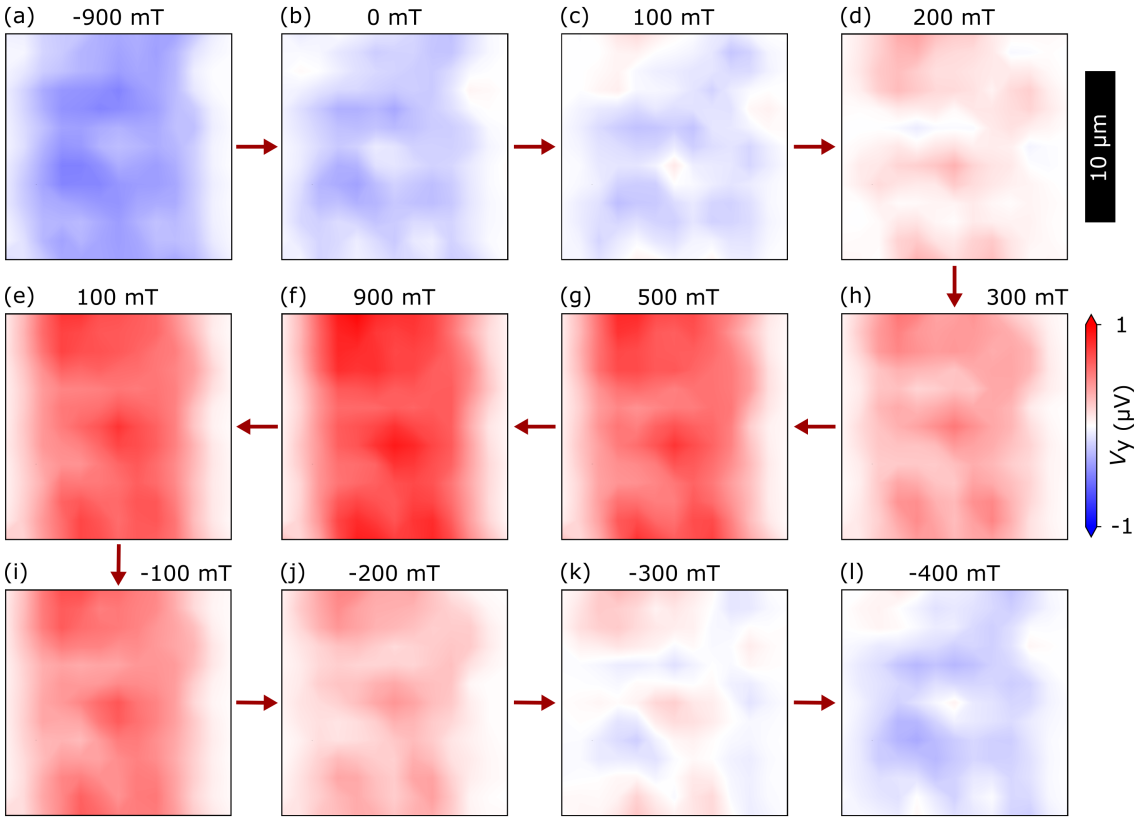

Figure 8.6: Magnetic domain images in Mn_3Sn wire structure at different applied magnetic fields and at the film temperature of 125 °C.

The average value of V_y as a function of the applied magnetic field gives us the ANE-based hysteresis loop (Figure 8.7a). Here, the field dependence of the signal corresponds to the switching of the magnetic order. This is further validated by a longitudinal MOKE-based hysteresis loop that shows similar coercivity (Figure 8.7b). The ANE-based hys-

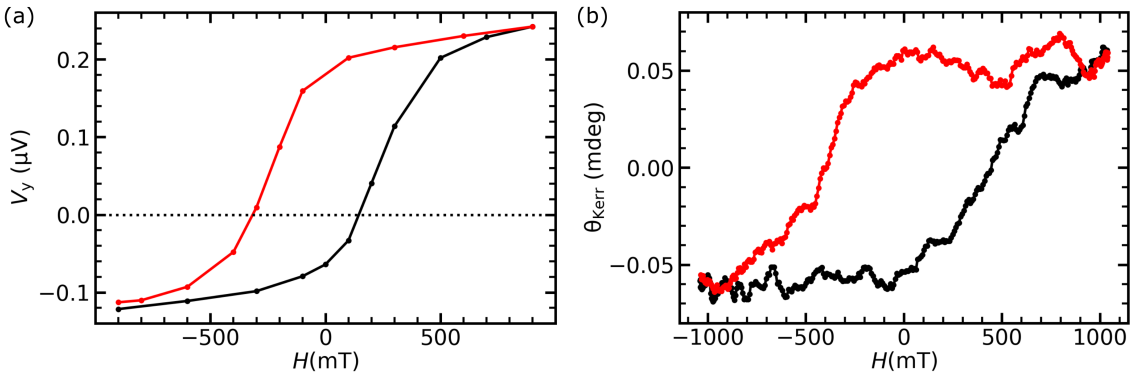

Figure 8.7: (a) ANE-based hysteresis. (b) Hysteresis loop at the film temperature of 125 °C obtained by longitudinal MOKE.

teresis shows an offset in V_y. The field-independent contribution either through the non-magnetic Seebeck effect V_{SE}^{NM}, or as a result of partial field-induced switching V_{ANE}^{FI} can cause this offset. A nonmagnetic signal in such opto-electrical measurements results from a well-understood Seebeck effect-induced thermoelectric voltage [126]. We show

that such a signal arises in our measurements at the grain boundaries due to different Seebeck coefficients of the grains (Appendix A.2, B.2). To investigate the presence of field-independent ANE signal $V_{\mathrm{ANE}}^{\mathrm{FI}}$, we study the angular dependence of the measured signal. This set of measurements is performed in a device consisting of wire structures oriented along the x- and y-axis (Figure 8.8a). The measured voltage signal in the horizontal ($V_{\mathrm{x}} \propto M_{\mathrm{y}}$) and the vertical arms ($V_{\mathrm{y}} \propto M_{\mathrm{x}}$) allows us to deduce two orthogonal components of the MOOP vector (see equation (8.2)). We switch the MOOP orientation by field-cooling the film in the presence of a 1.3 T magnetic field applied at different IP angles (θ). The average measured voltage in the two arms V_{x} (V_{y}), directly proportional to M_{y} (M_{x}) are plotted against θ(Figure 8.8c). The observed 90° phase gap between V_{x} and V_{y} confirms that they relate to two orthogonal components of $\mathbf{M}$. Both V_{x} and V_{y} are dependent on θ. That would mean that for an applied IP field at an angle θ, the MOOP vector reorients at an IP angle θ_1 (Figure 8.8b).

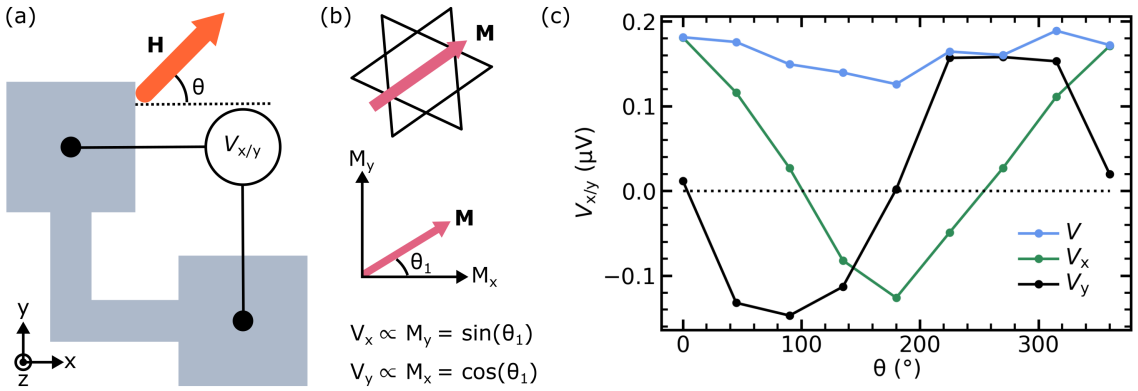

Figure 8.8: (a) Device structure shown schematically. MOOP vector is switched by applying an IP magnetic field at angle of θ. (b) Reorientation of the magnetic order with IP applied field. (c) Average V_{x} and V_{y} as a function of θ.

We demonstrate this further by spatially resolved measurements. Orientation of the MOOP vector along $\hat{\mathbf{x}}$ by applying IP field along $\theta = 0$ results in positive M_{x}. This is indicated by dominant red contrast in the vertical arm of the device due to the ANE signal from positive M_{x} (Figure 8.9a). In this case, M_{y} is zero. Thus, no ANE signal is expected in the horizontal arm. This reflects in arbitrary bipolar contrast due to V^{FI} in the horizontal arm. Applying the field at $\theta = 45°$ results in both M_{x} and M_{y} being positive, as observed by dominant red contrast in both arms (Figure 8.9b). Applying the field along $\theta = 90°$ reorients the MOOP along positive y-direction. This changes the contrast in the vertical arm from dominant red to $V^{\mathbf{FI}}$-like bipolar pattern (Figure 8.9c). Similarly, the field at $\theta = 135°$ results in positive M_{y} and negative M_{x} (Figure 8.9d).

In contrast to uni-axial magnetic materials, Mn_3Sn possesses three easy axes along $\langle \bar{2}\bar{1}10 \rangle$ directions [70, 127, 128].This means that there is an easy direction in the film's plane at every 60°. An applied IP field at angle θ results in the reorientation of the MOOP vector along θ_1 (Figure 8.8b). This orientation is likely to correspond to one of the nearest easy-switching directions. This is because the maximum separation between the field and easy directions would be 60°. Thus, the strength of the projection of 1.3 T applied field

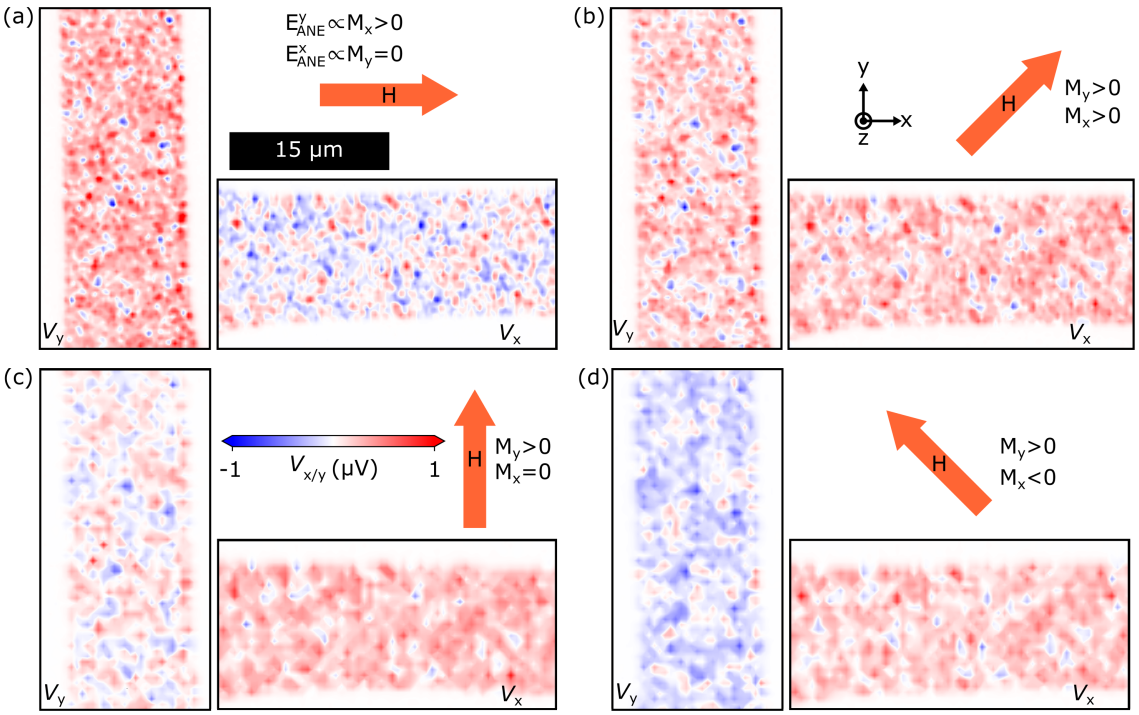

Figure 8.9: Spatially resolved ANE measurement in a cross-shaped Mn_3Sn device. The left vertical panel shows a scan over a 15 μm×30 μm region in the vertical wire structure; the right horizontal panel shows a 30 μm×15 μm region of the horizontal arm. The scans were performed after field cooling the device in the presence of a 1.3 T IP applied filed at different angles. (a) $\theta = 0°$. (b) $\theta = 45°$. (c) $\theta = 90°$. (d) $\theta = 135°$.

along the easy direction would be at least $1.3\,\mathrm{T} \times \cos(60°) = 650\,\mathrm{mT}$, which is larger than the coercivity. However, if this process achieved complete switching, the magnitude of $\mathbf{M}$ ($M = \sqrt{M_x^2 + M_y^2} \propto V = \sqrt{V_x^2 + V_y^2}$) would not be dependent on θ. Instead, V has a minimum at $\theta = 180°$. This indicates that the magnetic field induces a partial switching, and the population of domains pinned along $\hat{\mathbf{x}}$ is relatively higher.

8.5 Magnetic domains in Mn_3Sn at the nanoscale

The sub-micrometre domain imaging in previous Sections reveals that the magnetic domain size is smaller than the spot size of the focused laser beam (≈760 nm). To understand the switching behaviour of the domain at the nanoscale, we employ NF-SANE microscope to image magnetic domains in a Mn_3Sn nanowire. For this, the film is patterned into a device consisting of a 300 nm × 10 μm wire structure. The device is mounted onto a mobile chip carrier that can be placed in an external magnet with a heater. The magnetic domains are switched by cooling the film in the presence of a magnetic field applied along the nanowire width. ANE-induced voltage in the nanowire is measured while the sample underneath the AFM tip is illuminated with a laser beam (Figure 8.10a).

Magnetic domain images after field cooling in the presence of ±1.3 T magnetic field are shown in (Figure 8.10b,c). Subtracting and adding them gives magnetic and field-independent contributions, respectively (Figure 8.10d,e). Simultaneously measured to-

pography allows us to correlate field-independent V^{FI} signal with the granular structure of the device (Figure 8.10f). The regions with a larger V^{FI} in (Figure 8.10e) correspond to the region in the vicinity of the grains as shown with the AFM topography (Figure 8.10f). This shows that one of the contributions to V^{FI} is from the Seebeck effect-induced voltage $V_{\mathrm{SE}}^{\mathrm{NM}}$.

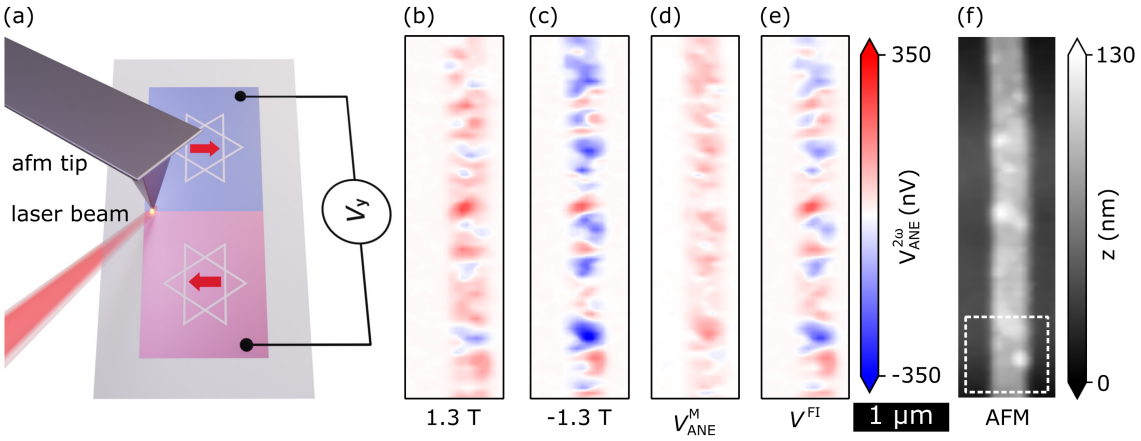

Figure 8.10: (a) Schematic illustration of the ANE-based near-field imaging in Mn_3Sn. A nanowire underneath the AFM tip is illuminated with a laser beam with a power of 25 mW and with a wavelength of 8 µm. The thermal voltage generated by the enhanced near field is detected by demodulating V_y at the second harmonics of the tip vibration frequency.(b,c) Spatially resolved near-field scanning ANE measured after field cooling the device in the presence of ±1.3 T magnetic field, respectively. The scanning was performed in a step size of 50 nm. (d) Map of the magnetic contribution to the measured signal. (e) Field-independent contribution to the measured voltage. (f) AFM topography of the device structure. The scan was recorded simultaneously, while performing scanning ANE measurements shown in (c).

In order to further investigate the field-independent contribution, we zoom in on a region containing a few grains, as marked by dotted square in Figure 8.10f. This is done by performing the scan in a smaller step size of 20 nm, giving higher pixel density. Magnetic domains in Mn_3Sn are thereby imaged with NF-SANE resolution of ≈70 nm. In addition to a relatively higher V^{FI} near the grain, a nonzero V^{FI} is observed away from the grains as well (Figure 8.11d,e). We attribute this to be the result of domain pinning giving field-independent ANE signal $V_{\mathrm{ANE}}^{\mathrm{FI}}$. Furthermore, field-dependent magnetic contribution is spatially nonuniform (Figure 8.10d, Figure 8.11c). This, too, suggests that the magnetic field induces partial switching, resulting a smaller $V_{\mathrm{ANE}}^{\mathrm{M}}$ in the region with smaller switching. This observation is similar to the switching behaviour of collinear antiferromagnets observed using high-resolution photoemission electron microscopy. In that case, current-induced spin-orbit-torque in CuMnAs [129] and Mn_2Au [130], as well as applied magnetic fields of up to 70 T in Mn_2Au [131], show a partial switching.

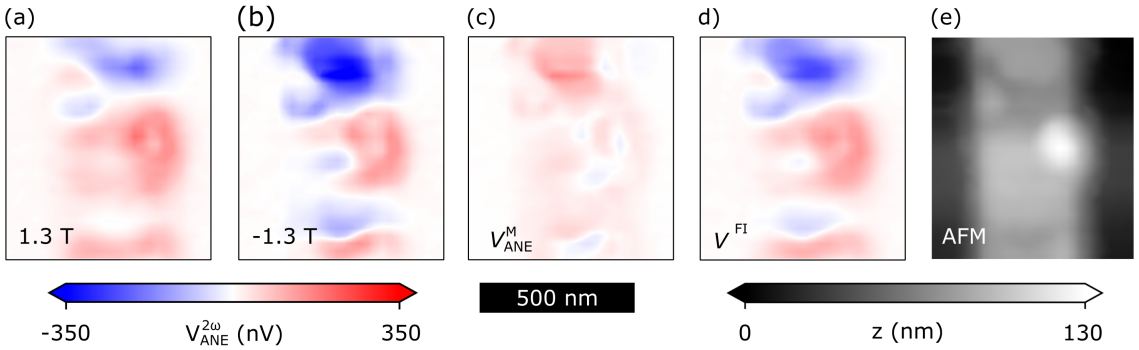

Figure 8.11: Near-field scanning measurements performed in a step size of 20 nm. (a,b) After field cooling in a ±1.3 T magnetic field, respectively. (c) Field-dependent contribution (d) Field-independent contribution. (e) AFM topography.

8.6 Discussion

We showed that the coercivity of Mn_3Sn is sensitive to the film temperature. By heating the film close to the ordering temperature, a small magnetic field on the order of 100 mT can alter the magnetic order. Due to the finite resistance of the Mn_3Sn micro-wire structures (≈500 Ω), resistive heating by applying a current through the wire structure can reduce the coercivity. We passed a current pulse through the wire to switch the magnetic state in the Mn_3Sn wire structure with an applied field of 900 mT (Appendix B1). Due to resistive heating with the current pulse, this field could alter the magnetic state, which otherwise induces negligible switching at room temperature. Several experiments based on spin-orbit-torque switching require a high current density pulse [70, 132, 133], therefore the effect of the current-induced heating on the coercivity needs to be considered in such experiments.

8.7 Conclusion

We demonstrated that the ANE response can be utilized to detect the magnetic state of a noncollinear antiferromagnet with nanoscale spatial resolution. By systematically studying the effect of the film temperature and the applied magnetic field, we show the role of heating on the coercivity. Our analysis at the sub-micrometres reveals that the method is affected by a nonmagnetic signal in addition to the magnetic contrast. We extract the magnetic signal and verify it with the magneto-optical Kerr measurements. By detecting two orthogonal components of the magnetic order parameter vector, we visualize different magnetic states of Mn_3Sn. Switching with an applied field at different angles in the Kagome plane, as well as the nanoscale domain imaging, indicate partial field-induced switching. This switching behaviour is similar to that of collinear antiferromagnets.

Chapter 9

Conclusion and Outlook

We used laser heating-induced opto-electrical signals to probe the magnetic state of a sample in a spatially resolved manner. These signals are generated by Berry curvature-driven optical or magnetotransport responses, which are related to the material's magnetic states but do not necessarily scale with the magnetization. For example, NCAFs show large optical and magnetotransport responses despite barely any net magnetization. Therefore, the results are significant for the rapidly growing field of chiral antiferromagnetic spintronics. In the first step, we studied standard ferromagnetic materials with well-understood magnetic properties to examine various characteristics of these methods.

Two of such responses studied in this thesis include the MCD effect. We showed that HDP voltage generated by laser heating-induced MCD response can be used to detect the magnetic states of the sample. Spatially resolved measurements of this HDP voltage provide a magnetic domain image of the sample. A similar magneto-optical response is the MOKE, which has been conventionally used to image domains in IP and OOP magnetized samples. However, the Kerr-based imaging contains additional background signals related to optical topography in addition to the magnetic contrast. In contrast, the method presented here provides background-free imaging. The MCD effect utilized for this method is shown to be present in NCAFs as well [41, 42]. Therefore, it would be interesting to extend the method for visualizing magnetic structures of NCAFs.

The majority of the discussion presented in the thesis concerns the second method based on ANE-driven response. We demonstrated that laser heating-induced temperature gradient generates an ANE signal in FMs as well as NCAFs, and we verified the magnetic origin of this signal. We performed spatially resolved measurements to image magnetic domains of IP magnetized CoFeB films, and the observed magnetic contrast was correlated with the magnetic domain images of the same sample obtained by a conventional Kerr-based optical microscope. In a scanning probe microscope like here, the size of the smallest resolvable feature is determined by the lateral size of the probe. Since the ANE signal in an IP magnetized material is proportional to the average OOP temperature gradient across the film thickness, we determined the lateral size of this average gradient. This was done by reversing the problem and studying a well-defined magnetic structure of a Landau pattern surrounding a magnetic vortex core. For a laser beam having a Gaus-

sian laser intensity across its focal spot, we found that the OOP temperature gradient was also a Gaussian with a FWHM of ≈760 nm. This was close to the FWHM of the laser intensity distribution ≈740 nm. These results were further supported by the finite element modeling simulations of the laser heating. The simulations also indicated that temperature spread due to laser heating is extended beyond the laser focal spot. In contrast, the average temperature gradient across the 15 nm thick CoFeB film was found to be confined to the laser focal spot.

We used an optical-near field underneath the apex of an AFM tip to further improve the spatial resolution of the ANE microscope beyond the size of the laser focal spot. We found the lateral size of the apex of the tip to be ≈30 nm, and the optical near-field being confined on the same scale of approximately 31 nm. FEM simulation indicated that, in this case, the FWHM of the OOP temperature gradient is expected to be 38 nm, which is only 26% higher than the FWHM of the spatial distribution of optical near-field. In experiments, we obtained a spatial resolution of the ANE measurements up to 56 nm. This was due to the broadening of the tip apex. However, for a new tip with smaller apex diameter of up to 20 nm, a scanning ANE measurement with a spatial resolution of up to 25 nm is possible.

We also demonstrated the applicability of SANE method for imaging magnetic domains in OOP-magnetized materials. Partially illuminating an OOP magnetized wire structure at the edges results in a net IP temperature gradient. This can be used to obtain an ANE signal that is proportional to OOP magnetization. The net IP temperature gradient vanishes away in the middle region of the wire structure. Here, a nonuniform magnetization results in a nonzero ANE signal that relates to the gradient of OOP magnetization. Such an ANE signal can also be used for imaging magnetization gradients, as it has been done by the Lorentz transmission electron microscopy.

We extended the ANE method to detect the magnetic state of a NCAF with nanoscale spatial resolution. Our analysis at the sub-micrometres reveals that the method is affected by a nonmagnetic signal in addition to the magnetic contrast. We extracted the magnetic signal and verified it with the MOKE measurements. Here, the nonmagnetic contribution originates from the differential Seebeck coefficients of two grains at the grain boundaries. The granular structures are a consequence of the high-temperature annealing process that is needed for the chemical ordering of the Mn_3Sn compound. This also implies that the nonmagnetic contribution is an inherent property of the prepared film and can be removed by a background subtraction as it is done in differential Kerr imaging [134]. The nonmagnetic background in the Kerr imaging results from the optical reflectivity of the sample; its magnitude is much larger than the magnetic signal, and it is highly sensitive to position of the sample. In contrast, the Seebeck effect-induced nonmagnetic signal in ANE imaging is comparable in magnitude to the magnetic signal, and it is independent of the sample position.

We showed the role of heating on the coercivity by systematically studying the effect of the film temperature and the applied magnetic field on the switching percentage. Our

analysis indicates that the coercivity is reduced to $\approx$100 mT at an elevated temperature of 125 °C. This allows the manipulation of the stubborn magnet with a readily available small magnetic field by applying a current pulse to heat the wire structure to an elevated temperature.

Detecting two orthogonal components of the magnetic order parameter vector allowed us to visualize different remanent magnetic states of Mn_3Sn. Switching with an applied field at different angles in the Kagome plane, as well as the nanoscale domain imaging, indicate partial field-induced switching. This switching behaviour is similar to field-induced switching of collinear antiferromagnets. Being able to visualize the partial switching can be helpful for future experiments aiming to maximize the switching percentage of Mn_3Sn films.

Finally, we point out that apart from magnetic domain imaging, laser heating-induced temperature gradient is a convenient and efficient tool for the ANE study of magnetic materials. Here, the device fabrication for the measurement of ANE voltage requires a one-step lithography process. The laser beam is absorbed in the film, which generates a temperature gradient directly in the film. This is in contrast to resistive heating-based ANE studies that require a multi-step lithography process, and the majority of the heat energy is dissipated elsewhere [32, 33, 80]. Moreover, the magnitude of the ANE signal scales inversely with the wire width of the device structure. Studying a narrower wire with an ANE microscope gives a larger ANE signal.

Part IV

Appendices

Appendix A

Scanning ANE microscope

A.1 Laser power dependence of the ANE signal

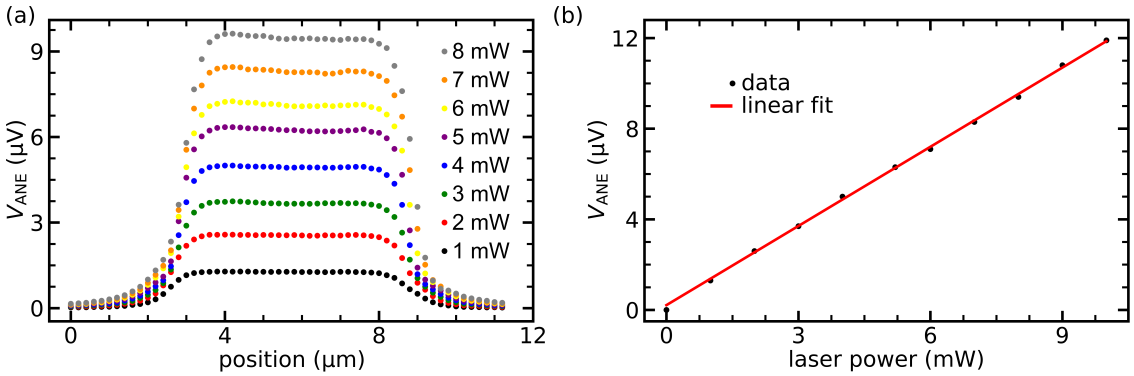

Figure A.1: (a) An ANE line scan across a 6 μm wide CoFeB wire structure at different laser power. (b) Average ANE signal across the wire vs the laser power is plotted and the linear fit is shown.

A.2 Nonmagnetic signal in ANE microscope

We discuss Seebeck effect induced thermal voltage (V_{SE}) in the context of the scanning ANE microscope. Laser heating leads to increase of the film temperature to T_h underneath the laser spot. In a wire structure with length L, V_{SE} can be written as follows:

$$V_{SE} \propto \int_0^L S \cdot \nabla T \, dy \tag{A.1}$$

Where S is the Seebeck coefficient. If the wire is homogeneous with a Seebeck coefficient of S_0 (Figure A.2a), then the equation (A.1) simplifies as follow:

$$V_{SE} \propto S_0 \cdot (T_1 - T_3) = S_0 \cdot (T_0 - T_0) = 0$$

Thus, the nonmagnetic thermal voltage does not arise in a homogeneous film. Next, we consider a film with nonuniform morphology. For the illustration purpose, we consider

a simpler case where the laser spot illuminates the junction of two different materials having Seebeck coefficients S_1 and S_2 (Figure A.2b). Here the equation (A.1) gives,

$$V_{\mathrm{SE}} \propto S_1 \cdot (T_1 - T_2) + S_2 \cdot (T_2 - T_3) = (S_2 - S_1)(T_{\mathrm{h}} - T_0) \tag{A.2}$$

Equation (A.1) indicates that in this case a nonzero thermal voltage arises. It is proportional to laser heating-induced increment of the film temperature $(T_{\mathrm{h}} - T_0)$ and the difference in the Seebeck coefficients. We image a standard magnetic structure of a Landau pattern in a CoFeB film. The film contains a dust particle so that the Seebeck coefficient in the dust region is different from that in the rest of the film. We observe a nonmagnetic signal in the region surrounding the dust (Figure A.2c). Across the dust particle, the sign of the nonmagnetic signal changes due to sign change of $S_2 - S_1$. we note that the magnitude of the nonmagnetic signal is higher relative to that of ANE signal in a typical ferromagnet.

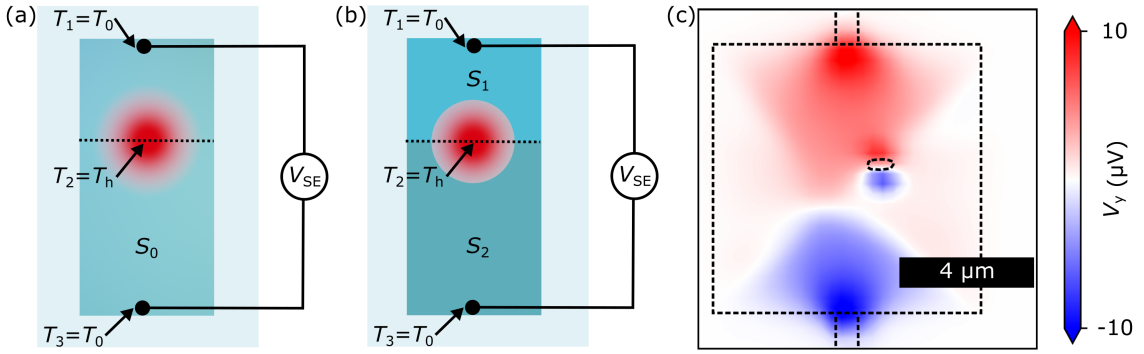

Figure A.2: (a) A laser beam illuminating a homogeneous film. (b) The laser beam illuminates a junction of two materials having different Seebeck coefficients. (c) SANE imaging of the Landau pattern in a CoFeB device containing of a dust particle at the position indicated by the dotted loop.

A.3 Different Landau patterns imaged with the ANE microscope

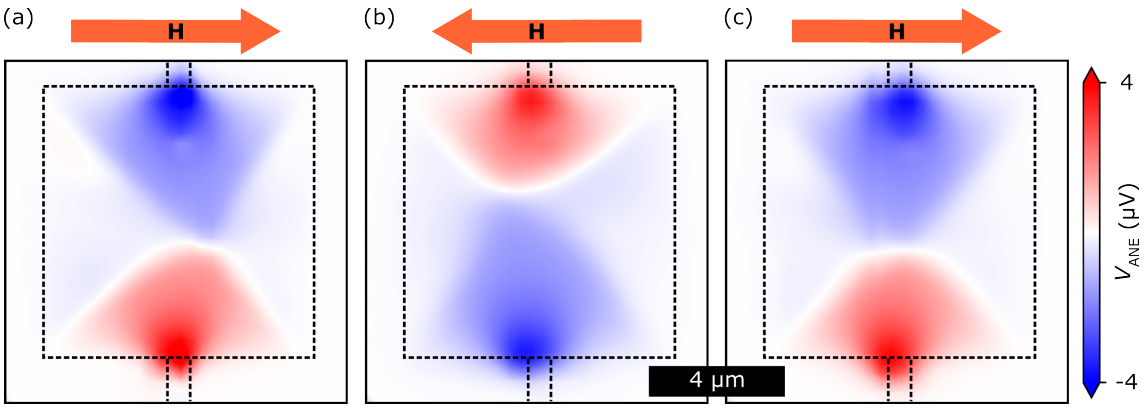

Figure A.3: SANE microscope image of the different Landau pattern created in a 8 µm × 8 µm slab with a thickness of 45 nm. (a) A magnetic field of 50 mT is applied along the x-direction. The imaging is subsequently performed after reducing the field to zero. (b) Same is repeated with an initial applied field of −50 mT. (c) The measurements in (a) is repeated.

A.4 NF-SANE spot size of the heat gradient

We show that the result for the spot size of the heat gradient obtained by ANE line scan is reproducible (Figure 6.3). The ANE line scan from a different set of the measurements reveals the spot size to be 74 nm, which is close to 76 nm obtained in Figure 6.3.

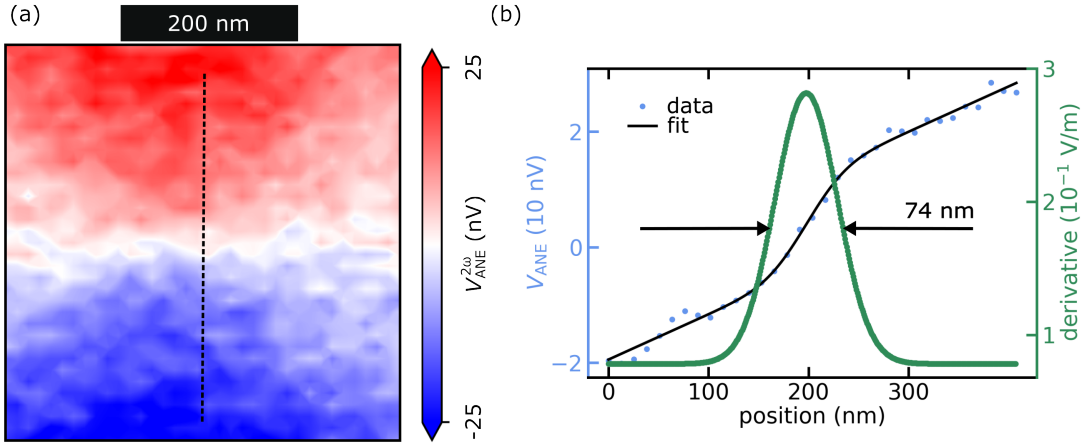

Figure A.4: (a) ANE imaging of the vortex core shown in Figure 6.3(a). ANE line scan along the dotted line shown in (a) (blue curve), the black line shows the fit to the error function. Right, green axis shows the derivative of the fitted curve.

A.5 Micromagnetic simulation

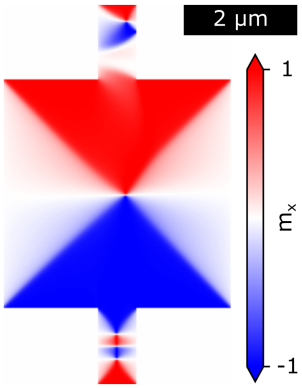

Figure A.5: Micromagnetic simulation for the device discussed in the Figure 6.6.

Appendix B

Noncollinear antiferromagnet

B.1 Reduced coercivity with the current-induced resistive heating

In Chapter 8 we showed that a magnetic field of upto 1 T induces negligible switching in Mn_3Sn at the room temperature. However, heating the film to 125 °C reduces the coercivity so that the same magnetic field can change the magnetic order. Here, we show that this result can be utilized to switch the magnetic order with the help of 900 mT field by passing a current pulse though the Mn_3Sn wire structure. This is caused by the resistive heating of the wire that reduces the coercivity. We start with a magnetic state with the MOOP vector oriented along $\hat{\mathbf{x}}$ (Figure B.1a). Then we apply a current pulse in the presence of −900 mT field. Subsequent ANE imaging reveals that this cause the MOOP vectors to switch along -$\hat{\mathbf{x}}$ (Figure B.1b). Applying the current pulse in the presence of 900 mT field reorients the MOOP vector along $\hat{\mathbf{x}}$ (Figure B.1c).

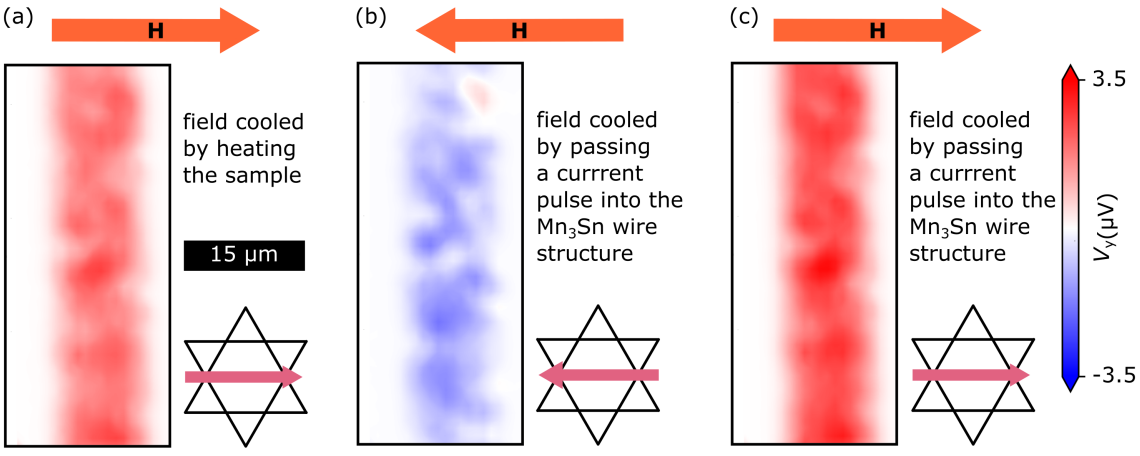

Figure B.1: (a) Initial magnetic state of a Mn_3Sn wire structure. The MOOP vector are switched along $\hat{\mathbf{x}}$ by cooling the device in a 900 mT applied field. (b) ANE imaging of the wire structure after applying a current pulse in the presence of −900 mT field. (c) Same as (b) but in the presence of 900 mT field.

B.2 Nonmagnetic signal in ANE scans of a NCAF

Here we show that the granular morphology of the Mn_3Sn films (Figure 8.10) results in a nonmagnetic thermal voltage signal in ANE measurements. We perform scanning ANE scan in a c-axis oriented 60 nm thick film of Mn_3Sn grown on a Al_2O_3 substrate. The ANE imaging of the film after field cooling in ±900 mT field (Figure B.2a,b) indicates that majority of the measured signal in this film is field-independent. This could be due dominance of either Seebeck effect induced thermal voltage or pinned domains resulting in a field-independent ANE signal. In order to get rid of such a field-independent ANE signals, we perform ANE imaging above the ordering temperature 150 °C. This is done by heating the film to 135 °C and increasing the laser power to 15 mW expected to further increase the temperature by 50°. This estimate is based on 18 °C increment by a laser beam with a power of 5 mW (Figure 5.3). In a disordered state, we observe nonzero signal that correspond to Seebeck effect-induced thermal voltage (Figure B.2c). The magnitude and the sign of this signal dependents on the gradient of the Seebeck coefficient, which, in turns, depends on the morphology of the film. This results in a complex profile of a such a signal. We intentionally focus a very high power laser beam to drastically change (by burning) the morphology at a point. We clearly see a larger bipolar signal in the vicinity of that point, similar to that in CoFeB film with a dust particle.

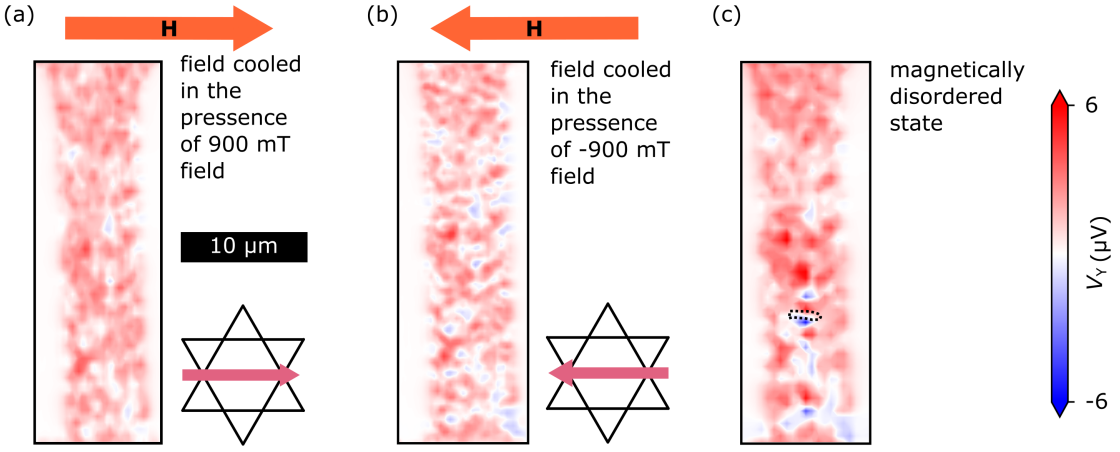

Figure B.2: (a,b) SANE scans in a Mn_3Sn wire structure after cooling the film in a ±900 mT field, respectively. (c) SANE imaging of the same device performed at an elevated temperature above the order temperature of Mn_3Sn. The dotted loop indicate the position of a point being burnt by higher power focused laser beam.

B.3 Nanoscale domain imaging in a NCAF nanowire

Here, we show additional nanoscale domain imaging discussed in Figures 8.11, 8.12. The measurements shown here were performed in a relatively wider (400 nm) nanowire. This results in a relatively smaller ANE signal $\left(V_{\mathrm{ANE}} \propto \frac{p}{w}\right)$. NF-SANE imaging performed after cooling the device in ±1.3 T field show that the MOOP can be switched back and forth between $\hat{\mathbf{x}}$ and $-\hat{\mathbf{x}}$ (Figure B.3a-c). The measurements performed in a smaller step

size (higher pixel density) shows that the measured signal arises only within the region containing the Mn_3Sn nanowire (Figure B.3d). Simultaneously measured AFM topography scan shows the granular nature of the film morphology (Figure B.3e)

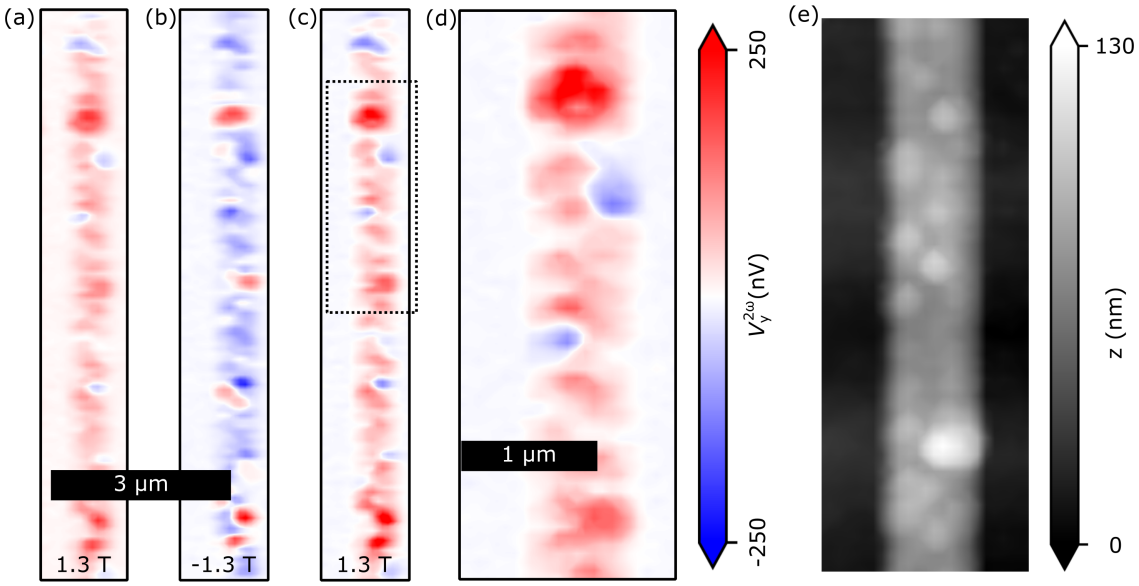

Figure B.3: (a-c) NF-SANE scan of a Mn_3Sn nanowire performed in a step size of 50 nm. The scans were performed after cooling the device in a magnetic field of ±1.3 T. (d) Higher pixel density NF-SANE scan with a step size of 20 nm performed in the region shown by the dotted square in (c). (d) AFM topographic scan performed simultaneously with NF-SANE scan shown in (d).

Curriculum vitae

Atul Pandey

Max Planck Institute of Microstructure Physics
Weinberg 2
06120 Halle
atul.pandey@mpi-halle.mpg.de

Education

12/2020 - 10/2024	Doctoral Candidate Martin-Luther-Universität Halle-Wittenberg and Max Planck Institute of Microstructure Physics
08/2014 - 05/2019	Five Year BS-MS dual degree, Major in Physics Indian Institute of Science Education and Research Kolkata India
07/2011 - 04/2013	Higher Secondary Education The Maharashtra State Board of Secondary & Higher Secondary Education India
07/2009 - 04/2011	High School Board of High School and Intermediate education Uttar Pradesh India

List of publications

1. Origin of helicity-dependent photoconductivity in magnetic and nonmagnetic wires
Atul Pandey, Rouven Dreyer, Palvan Seyidov, Chris Koerner, Saban Tirpanci, Binoy Krishna Hazra, Stuart Parkin, and Georg Woltersdorf
Phys. Rev. B **106**, 174420 (2022)
https://doi.org/10.1103/PhysRevB.106.174420

2. Anomalous Nernst effect based near field imaging of magnetic nanostructures
Atul Pandey, Jitul Deka, Jiho Yoon, Chris Koerner, Rouven Dreyer, James M. Taylor, Stuart S. P. Parkin, Georg Woltersdorf
ACS Nano **18**, **46**, 31949–31956 (2024)
https://doi.org/10.1021/acsnano.4c09749

3. Switching of magnetic domains in a noncollinear antiferromagnet at the nanoscale
Atul Pandey, Prajwal Rigvedi, Edouard Lesne, Jitul Deka, Jiho Yoon, Wolfgang Hoppe, Chris Koerner, Banabir Pal, James M. Taylor, Stuart S. P. Parkin, Georg Woltersdorf
https://doi.org/10.48550/arXiv.2409.15533

List of Tables

List of Figures

Bibliography

[1] Coughlin, T.M. *Fundamentals of Hard Disk Drives*, page 25–44. Springer International Publishing (2017).

[2] Theis, T.N. and Wong, H.S.P. The end of moore's law: A new beginning for information technology. *Computing in Science and Engineering* **19**(2), 41–50 (2017).

[3] Hu, J.M., Li, Z., Chen, L.Q., and Nan, C.W. High-density magnetoresistive random access memory operating at ultralow voltage at room temperature. *Nature Communications* **2**, 553 (2011).

[4] Baltz, V., Manchon, A., Tsoi, M., Moriyama, T., Ono, T., and Tserkovnyak, Y. Antiferromagnetic spintronics. *Rev. Mod. Phys.* **90**, 015005 (2018).

[5] Dieny, B. and Prejbeanu, I.L. *Magnetic Roandmap*, page 101–164. John Wiley and Sons, Inc. (2016).

[6] Pietambaram, S., Janesky, J., Dave, R., Sun, J., Steiner, G., and Slaughter, J. Exchange coupling control and thermal endurance of synthetic antiferromagnet structures for MRAM. *IEEE Transactions on Magnetics* **40**(4), 2619–2621 (2004).

[7] Duine, R.A., Lee, K.J., Parkin, S.S.P., and Stiles, M.D. Synthetic antiferromagnetic spintronics. *Nature Physics* **14**(3), 217–219 (2018).

[8] Yang, S.H., Naaman, R., Paltiel, Y., and Parkin, S.S.P. Chiral spintronics. *Nature Reviews Physics* **3**(5), 328–343 (2021).

[9] Gomonay, O., Jungwirth, T., and Sinova, J. Concepts of antiferromagnetic spintronics. *physica status solidi (RRL) – Rapid Research Letters* **11**(4), 1700022 (2017).

[10] Jungwirth, T., Marti, X., Wadley, P., and Wunderlich, J. Antiferromagnetic spintronics. *Nature Nanotechnology* **11**(3), 231–241 (2016).

[11] MacDonald, A.H. and Tsoi, M. Antiferromagnetic metal spintronics. *Philosophical Transactions of the Royal Society A: Mathematical, Physical and Engineering Sciences* **369**(1948), 3098–3114 (2011).

[12] Němec, P., Fiebig, M., Kampfrath, T., and Kimel, A.V. Antiferromagnetic optospintronics. *Nature Physics* **14**(3), 229–241 (2018).

[13] Gomonay, E.V. and Loktev, V.M. Spintronics of antiferromagnetic systems (Review Article). *Low Temperature Physics* **40**(1), 17–35 (2014).

[14] Železný, J., Wadley, P., Olejník, K., Hoffmann, A., and Ohno, H. Spin transport and spin torque in antiferromagnetic devices. *Nature Physics* **14**(3), 220–228 (2018).

[15] Nagaosa, N., Sinova, J., Onoda, S., MacDonald, A.H., and Ong, N.P. Anomalous Hall effect. *Rev. Mod. Phys.* **82**, 1539–1592 (2010).

[16] Wadley, P., Reimers, S., Grzybowski, M.J., Andrews, C., Wang, M., Chauhan, J.S., Gallagher, B.L., Campion, R.P., Edmonds, K.W., Dhesi, S.S., Maccherozzi, F., Novak, V., Wunderlich, J., and Jungwirth, T. Current polarity-dependent manipulation of antiferromagnetic domains. *Nature Nanotechnology* **13**(5), 362–365 (2018).

[17] Tang, F., Po, H.C., Vishwanath, A., and Wan, X. Comprehensive search for topological materials using symmetry indicators. *Nature* **566**(7745), 486–489 (2019).

[18] Wieder, B.J., Bradlyn, B., Cano, J., Wang, Z., Vergniory, M.G., Elcoro, L., Soluyanov, A.A., Felser, C., Neupert, T., Regnault, N., and Bernevig, B.A. Topological materials discovery from crystal symmetry. *Nature Reviews Materials* **7**(3), 196–216 (2021).

[19] Jungwirth, T., Sinova, J., Manchon, A., Marti, X., Wunderlich, J., and Felser, C. The multiple directions of antiferromagnetic spintronics. *Nature Physics* **14**(3), 200–203 (2018).

[20] Šmejkal, L., Mokrousov, Y., Yan, B., and MacDonald, A.H. Topological antiferromagnetic spintronics. *Nature Physics* **14**(3), 242–251 (2018).

[21] Bonbien, V., Zhuo, F., Salimath, A., Ly, O., Abbout, A., and Manchon, A. Topological aspects of antiferromagnets. *Journal of Physics D: Applied Physics* **55**(10), 103002 (2021).

[22] Chen, H., Liu, L., Zhou, X., Meng, Z., Wang, X., Duan, Z., Zhao, G., Yan, H., Qin, P., and Liu, Z. Emerging Antiferromagnets for Spintronics. *Advanced Materials* **36**(14), 2310379 (2024).

[23] Das, K. and Agarwal, A. Berry curvature induced thermopower in type-I and type-II Weyl semimetals. *Phys. Rev. B* **100**, 085406 (2019).

[24] Nayak, A.K., Fischer, J.E., Sun, Y., Yan, B., Karel, J., Komarek, A.C., Shekhar, C., Kumar, N., Schnelle, W., Kübler, J., Felser, C., and Parkin, S.S.P. Large anomalous Hall effect driven by a nonvanishing Berry curvature in the noncolinear antiferromagnet Mn_3Sn/Ge. *Science Advances* **2**(4), e1501870 (2016).

[25] Liu, J. and Balents, L. Anomalous Hall Effect and Topological Defects in Antiferromagnetic Weyl Semimetals: Mn_3Sn/Ge. *Phys. Rev. Lett.* **119**, 087202 (2017).

[26] Kübler, J. and Felser, C. Non-collinear antiferromagnets and the anomalous Hall effect. *EPL (Europhysics Letters)* **108**(6), 67001 (2014).

[27] Nakatsuji, S., Kiyohara, N., and Higo, T. Large anomalous Hall effect in a non-collinear antiferromagnet at room temperature. *Nature* **527**(7577), 212–215 (2015).

[28] Chen, H., Niu, Q., and MacDonald, A.H. Anomalous Hall Effect Arising from Noncollinear Antiferromagnetism. *Phys. Rev. Lett.* **112**, 017205 (2014).

[29] Šmejkal, L., MacDonald, A.H., Sinova, J., Nakatsuji, S., and Jungwirth, T. Anomalous Hall antiferromagnets. *Nature Reviews Materials* **7**(6), 482–496 (2022).

[30] Ikhlas, M., Tomita, T., Koretsune, T., Suzuki, M.T., Nishio-Hamane, D., Arita, R., Otani, Y., and Nakatsuji, S. Large anomalous Nernst effect at room temperature in a chiral antiferromagnet. *Nature Physics* **13**(11), 1085–1090 (2017).

[31] Wuttke, C., Caglieris, F., Sykora, S., Scaravaggi, F., Wolter, A.U.B., Manna, K., Süss, V., Shekhar, C., Felser, C., Büchner, B., and Hess, C. Berry curvature unravelled by the anomalous Nernst effect in Mn_3Ge. *Phys. Rev. B* **100**, 085111 (2019).

[32] Beckert, S., Godinho, J.a., Johnson, F., Kimák, J., Schmoranzerová, E., Zemen, J., Šobáň, Z.c.v., Olejník, K., Železný, J., Wunderlich, J., Němec, P., Kriegner, D., Thomas, A., Goennenwein, S.T.B., Cohen, L.F., and Reichlová, H. Anomalous Nernst effect in Mn_3NiN thin films. *Phys. Rev. B* **108**, 024420 (2023).

[33] Zhou, X., Hanke, J.P., Feng, W., Blügel, S., Mokrousov, Y., and Yao, Y. Giant anomalous Nernst effect in noncollinear antiferromagnetic Mn-based antiperovskite nitrides. *Phys. Rev. Mater.* **4**, 024408 (2020).

[34] Hong, D., Anand, N., Liu, C., Liu, H., Arslan, I., Pearson, J.E., Bhattacharya, A., and Jiang, J.S. Large anomalous Nernst and inverse spin-Hall effects in epitaxial thin films of kagome semimetal Mn_3Ge. *Phys. Rev. Mater.* **4**, 094201 (2020).

[35] Higo, T., Man, H., Gopman, D.B., Wu, L., Koretsune, T., van 't Erve, O.M.J., Kabanov, Y.P., Rees, D., Li, Y., Suzuki, M.T., Patankar, S., Ikhlas, M., Chien, C.L., Arita, R., Shull, R.D., Orenstein, J., and Nakatsuji, S. Large magneto-optical Kerr effect and imaging of magnetic octupole domains in an antiferromagnetic metal. *Nature Photonics* **12**(2), 73–78 (2018).

[36] Feng, W., Guo, G.Y., Zhou, J., Yao, Y., and Niu, Q. Large magneto-optical Kerr effect in noncollinear antiferromagnets Mn_3X $(X = \mathrm{Rh},\ \mathrm{Ir},\ \mathrm{Pt})$. *Phys. Rev. B* **92**, 144426 (2015).

[37] Uchimura, T., Yoon, J.Y., Sato, Y., Takeuchi, Y., Kanai, S., Takechi, R., Kishi, K., Yamane, Y., DuttaGupta, S., Ieda, J., Ohno, H., and Fukami, S. Observation of domain structure in non-collinear antiferromagnetic Mn_3Sn thin films by magneto-optical Kerr effect. *Applied Physics Letters* **120**(17), 172405 (2022).

[38] Wu, M., Isshiki, H., Chen, T., Higo, T., Nakatsuji, S., and Otani, Y. Magneto-optical Kerr effect in a non-collinear antiferromagnet Mn_3Ge. *Applied Physics Letters* **116**(13), 132408 (2020).

[39] Wu, M., Kondou, K., Nakatani, Y., Chen, T., Isshiki, H., Higo, T., Nakatsuji, S., and Otani, Y. Magnetic octupole domain evolution and domain-wall structure in the noncollinear Weyl antiferromagnet Mn_3Ge. *APL Materials* **11**(8), 081115 (2023).

[40] Wu, M., Chen, T., Nomoto, T., Tserkovnyak, Y., Isshiki, H., Nakatani, Y., Higo, T., Tomita, T., Kondou, K., Arita, R., Nakatsuji, S., and Otani, Y. Current-driven fast magnetic octupole domain-wall motion in noncollinear antiferromagnets. *Nature Communications* **15**, 4305 (2024).

[41] Kimata, M., Sasabe, N., Kurita, K., Yamasaki, Y., Tabata, C., Yokoyama, Y., Kotani, Y., Ikhlas, M., Tomita, T., Amemiya, K., Nojiri, H., Nakatsuji, S., Koretsune, T., Nakao, H., Arima, T.h., and Nakamura, T. X-ray study of ferroic octupole order producing anomalous Hall effect. *Nature Communications* **12**, 5582 (2021).

[42] Yamasaki, Y., Nakao, H., and Arima, T.h. Augmented Magnetic Octupole in Kagomé 120-degree Antiferromagnets Detectable via X-ray Magnetic Circular Dichroism. *Journal of the Physical Society of Japan* **89**(8), 083703 (2020).

[43] Abbe, E. Beiträge zur Theorie des Mikroskops und der mikroskopischen Wahrnehmung. *Archiv für Mikroskopische Anatomie* **9**(1), 413–468 (1873).

[44] ARAKI, T. The history of optical microscope. *Mechanical Engineering Reviews* **4**(1), 16–00242 (2017).

[45] Kino, G.S. and Corle, T.R. *Confocal scanning optical microscopy and related imaging systems*. Academic Press (1996).

[46] Cheong, S.W., Fiebig, M., Wu, W., Chapon, L., and Kiryukhin, V. Seeing is believing: visualization of antiferromagnetic domains. *npj Quantum Materials* **5**, 3 (2020).

[47] Wadley, P., Howells, B., Železný, J., Andrews, C., Hills, V., Campion, R.P., Novák, V., Olejník, K., Maccherozzi, F., Dhesi, S.S., Martin, S.Y., Wagner, T., Wunderlich, J., Freimuth, F., Mokrousov, Y., Kuneš, J., Chauhan, J.S., Grzybowski, M.J., Rushforth, A.W., Edmonds, K.W., Gallagher, B.L., and Jungwirth, T. Electrical switching of an antiferromagnet. *Science* **351**(6273), 587–590 (2016).

[48] Bommanaboyena, S.P., Backes, D., Veiga, L.S.I., Dhesi, S.S., Niu, Y.R., Sarpi, B., Denneulin, T., Kovács, A., Mashoff, T., Gomonay, O., Sinova, J., Everschor-Sitte, K., Schönke, D., Reeve, R.M., Kläui, M., Elmers, H.J., and Jourdan, M. Readout of an antiferromagnetic spintronics system by strong exchange coupling of Mn2Au and Permalloy. *Nature Communications* **12**, 6539 (2021).

[49] Bodnar, S.Y., Filianina, M., Bommanaboyena, S.P., Forrest, T., Maccherozzi, F., Sapozhnik, A.A., Skourski, Y., Kläui, M., and Jourdan, M. Imaging of current induced Néel vector switching in antiferromagnetic Mn_2Au. *Phys. Rev. B* **99**, 140409 (2019).

[50] Reimers, S., Lytvynenko, Y., Niu, Y.R., Golias, E., Sarpi, B., Veiga, L.S.I., Denneulin, T., Kovács, A., Dunin-Borkowski, R.E., Bläßer, J., Kläui, M., and Jourdan, M. Current-driven writing process in antiferromagnetic Mn2Au for memory applications. *Nature Communications* **14**, 1861 (2023).

[51] Chen, J., Badioli, M., Alonso-González, P., Thongrattanasiri, S., Huth, F., Osmond, J., Spasenović, M., Centeno, A., Pesquera, A., Godignon, P., Zurutuza Elorza, A., Camara, N., de Abajo, F.J.G., Hillenbrand, R., and Koppens, F.H.L. Optical nano-imaging of gate-tunable graphene plasmons. *Nature* **487**(7405), 77–81 (2012).

[52] Huber, A.J., Keilmann, F., Wittborn, J., Aizpurua, J., and Hillenbrand, R. Terahertz Near-Field Nanoscopy of Mobile Carriers in Single Semiconductor Nanodevices. *Nano Letters* **8**(11), 3766–3770 (2008). PMID: 18837565.

[53] Chuang, T.C., Su, P.L., Wu, P.H., and Huang, S.Y. Enhancement of the anomalous Nernst effect in ferromagnetic thin films. *Phys. Rev. B* **96**, 174406 (2017).

[54] Weiler, M., Althammer, M., Czeschka, F.D., Huebl, H., Wagner, M.S., Opel, M., Imort, I.M., Reiss, G., Thomas, A., Gross, R., and Goennenwein, S.T.B. Local Charge and Spin Currents in Magnetothermal Landscapes. *Phys. Rev. Lett.* **108**, 106602 (2012).

[55] Reichlova, H., Janda, T., Godinho, J., Markou, A., Kriegner, D., Schlitz, R., Zelezny, J., Soban, Z., Bejarano, M., Schultheiss, H., Nemec, P., Jungwirth, T., Felser, C., Wunderlich, J., and Goennenwein, S.T.B. Imaging and writing magnetic domains in the non-collinear antiferromagnet Mn_3Sn. *Nature Communications* **10**, 5459 (2019).

[56] Johnson, F., Kimák, J., Zemen, J., Šobáň, Z., Schmoranzerová, E., Godinho, J., Němec, P., Beckert, S., Reichlová, H., Boldrin, D., Wunderlich, J., and Cohen, L.F. Identifying the octupole antiferromagnetic domain orientation in Mn_3NiN by scanning anomalous Nernst effect microscopy. *Applied Physics Letters* **120**(23), 232402 (2022).

[57] Bartell, J.M., Ngai, D.H., Leng, Z., and Fuchs, G.D. Towards a table-top microscope for nanoscale magnetic imaging using picosecond thermal gradients. *Nature Communications* **6**, 8460 (2015).

[58] Janda, T., Godinho, J., Ostatnicky, T., Pfitzner, E., Ulrich, G., Hoehl, A., Reimers, S., Šobáň, Z., Metzger, T., Reichlová, H., Novák, V., Campion, R.P., Heberle, J., Wadley, P., Edmonds, K.W., Amin, O.J., Chauhan, J.S., Dhesi, S.S., Maccherozzi,

F., Otxoa, R.M., Roy, P.E., Olejník, K., Němec, P., Jungwirth, T., Kaestner, B., and Wunderlich, J. Magneto-Seebeck microscopy of domain switching in collinear antiferromagnet CuMnAs. *Phys. Rev. Mater.* **4**, 094413 (2020).

[59] Zhang, C., Bartell, J.M., Karsch, J.C., Gray, I., and Fuchs, G.D. Nanoscale Magnetization and Current Imaging Using Time-Resolved Scanning-Probe Magnetothermal Microscopy. *Nano Letters* **21**(12), 4966–4972 (2021).

[60] Isshiki, H., Budai, N., Kobayashi, A., Uesugi, R., Higo, T., Nakatsuji, S., and Otani, Y. Observation of Cluster Magnetic Octupole Domains in the Antiferromagnetic Weyl Semimetal Mn_3Sn Nanowire. *Phys. Rev. Lett.* **132**, 216702 (2024).

[61] Pfitzner, E., Hu, X., Schumacher, H.W., Hoehl, A., Venkateshvaran, D., Cubukcu, M., Liao, J.W., Auffret, S., Heberle, J., Wunderlich, J., and Kästner, B. Near-field magneto-caloritronic nanoscopy on ferromagnetic nanostructures. *AIP Advances* **8**(12), 125329 (2018).

[62] Van Waeyenberge, B., Puzic, A., Stoll, H., Chou, K.W., Tyliszczak, T., Hertel, R., Fähnle, M., Brückl, H., Rott, K., Reiss, G., Neudecker, I., Weiss, D., Back, C.H., and Schütz, G. Magnetic vortex core reversal by excitation with short bursts of an alternating field. *Nature* **444**(7118), 461–464 (2006).

[63] Wachowiak, A., Wiebe, J., Bode, M., Pietzsch, O., Morgenstern, M., and Wiesendanger, R. Direct Observation of Internal Spin Structure of Magnetic Vortex Cores. *Science* **298**(5593), 577–580 (2002).

[64] Dzyaloshinsky, I. A thermodynamic theory of "weak" ferromagnetism of antiferromagnetics. *Journal of Physics and Chemistry of Solids* **4**(4), 241–255 (1958).

[65] Hubert, A. and Schäfer, R. *Magnetic domains: the analysis of magnetic microstructures*. Springer Science & Business Media (2008).

[66] Johnson, M.T., Bloemen, P.J.H., Broeder, F.J.A.d., and Vries, J.J.d. Magnetic anisotropy in metallic multilayers. *Reports on Progress in Physics* **59**(11), 1409–1458 (1996).

[67] Brown, P.J., Nunez, V., Tasset, F., Forsyth, J.B., and Radhakrishna, P. Determination of the magnetic structure of Mn_3Sn using generalized neutron polarization analysis. *Journal of Physics: Condensed Matter* **2**(47), 9409–9422 (1990).

[68] Tomiyoshi, S. and Yamaguchi, Y. Magnetic Structure and Weak Ferromagnetism of Mn_3Sn Studied by Polarized Neutron Diffraction. *Journal of the Physical Society of Japan* **51**(8), 2478–2486 (1982).

[69] Nagamiya, T., Tomiyoshi, S., and Yamaguchi, Y. Triangular spin configuration and weak ferromagnetism of Mn_3Sn and Mn_3Ge. *Solid State Communications* **42**(5), 385–388 (1982).

[70] Pal, B., Hazra, B.K., Göbel, B., Jeon, J.C., Pandeya, A.K., Chakraborty, A., Busch, O., Srivastava, A.K., Deniz, H., Taylor, J.M., Meyerheim, H., Mertig, I., Yang, S.H., and Parkin, S.S.P. Setting of the magnetic structure of chiral kagome antiferromagnets by a seeded spin-orbit torque. *Science Advances* **8**(24), eabo5930 (2022).

[71] Foner, S. Versatile and Sensitive Vibrating-Sample Magnetometer. *Review of Scientific Instruments* **30**(7), 548–557 (1959).

[72] Drung, D., Abmann, C., Beyer, J., Kirste, A., Peters, M., Ruede, F., and Schurig, T. Highly Sensitive and Easy-to-Use SQUID Sensors. *IEEE Transactions on Applied Superconductivity* **17**(2), 699–704 (2007).

[73] Hall, E.H. On a New Action of the Magnet on Electric Currents. *American Journal of Mathematics* **2**(3), 287 (1879).

[74] Pugh, E.M., Rostoker, N., and Schindler, A. On the Hall Effect in Ferromagnetics. *Phys. Rev.* **80**, 688–692 (1950).

[75] Karplus, R. and Luttinger, J.M. Hall Effect in Ferromagnetics. *Phys. Rev.* **95**, 1154–1160 (1954).

[76] Sundaram, G. and Niu, Q. Wave-packet dynamics in slowly perturbed crystals: Gradient corrections and Berry-phase effects. *Phys. Rev. B* **59**, 14915–14925 (1999).

[77] Kubo, R. Statistical-Mechanical Theory of Irreversible Processes. I. General Theory and Simple Applications to Magnetic and Conduction Problems. *Journal of the Physical Society of Japan* **12**(6), 570–586 (1957).

[78] Kubo, R., Yokota, M., and Nakajima, S. Statistical-Mechanical Theory of Irreversible Processes. II. Response to Thermal Disturbance. *Journal of the Physical Society of Japan* **12**(11), 1203–1211 (1957).

[79] Nernst, W.W. and Ettingshausen, A. The reference for the Nernst effect. *Ann* **29**(343) (1886).

[80] Nakayama, H., Masuda, K., Wang, J., Miura, A., Uchida, K.i., Murata, M., and Sakuraba, Y. Mechanism of strong enhancement of anomalous Nernst effect in Fe by Ga substitution. *Phys. Rev. Mater.* **3**, 114412 (2019).

[81] Sakai, A., Mizuta, Y.P., Nugroho, A.A., Sihombing, R., Koretsune, T., Suzuki, M.T., Takemori, N., Ishii, R., Nishio-Hamane, D., Arita, R., Goswami, P., and Nakatsuji, S. Giant anomalous Nernst effect and quantum-critical scaling in a ferromagnetic semimetal. *Nature Physics* **14**(11), 1119–1124 (2018).

[82] Asamitsu, A., Miyasato, T., Abe, N., Fujii, T., Onose, Y., Onoda, S., Nagaosa, N., and Tokura, Y. Anomalous Hall effect and Nernst effect in itinerant ferromagnets. *Journal of Magnetism and Magnetic Materials* **310**(2), 2000–2002 (2007).

[83] Weischenberg, J., Freimuth, F., Blügel, S., and Mokrousov, Y. Scattering-independent anomalous Nernst effect in ferromagnets. *Phys. Rev. B* **87**, 060406 (2013).

[84] Chuang, T.C., Su, P.L., Wu, P.H., and Huang, S.Y. Enhancement of the anomalous Nernst effect in ferromagnetic thin films. *Phys. Rev. B* **96**, 174406 (2017).

[85] Chen, T., Minami, S., Sakai, A., Wang, Y., Feng, Z., Nomoto, T., Hirayama, M., Ishii, R., Koretsune, T., Arita, R., and Nakatsuji, S. Large anomalous Nernst effect and nodal plane in an iron-based kagome ferromagnet. *Science Advances* **8**(2), eabk1480 (2022).

[86] Zhou, X., Hanke, J.P., Feng, W., Blügel, S., Mokrousov, Y., and Yao, Y. Giant anomalous Nernst effect in noncollinear antiferromagnetic Mn-based antiperovskite nitrides. *Phys. Rev. Mater.* **4**, 024408 (2020).

[87] Singh, H.K., Samathrakis, I., Shen, C., and Zhang, H. Giant anomalous Hall and anomalous Nernst conductivities in antiperovskites and their tunability via magnetic fields. *Phys. Rev. Mater.* **6**, 045402 (2022).

[88] Xiao, D., Yao, Y., Fang, Z., and Niu, Q. Berry-Phase Effect in Anomalous Thermoelectric Transport. *Physical Review Letters* **97**(2), 026603 (2006).

[89] Sato, K. and Ishibashi, T. Fundamentals of Magneto-Optical Spectroscopy. *Frontiers in Physics* **10** (2022).

[90] Schatz, P.N. and McCaffery, A.J. The Faraday effect. *Quarterly Reviews, Chemical Society* **23**(4), 552 (1969).

[91] Feng, W., Hanke, J.P., Zhou, X., Guo, G.Y., Blügel, S., Mokrousov, Y., and Yao, Y. Topological magneto-optical effects and their quantization in noncoplanar antiferromagnets. *Nature Communications* **11**, 118 (2020).

[92] Li, X., Liu, C., Zhang, Y., Zhang, S., Zhang, H., Zhang, Y., Meng, W., Hou, D., Li, T., Kang, C., Huang, F., Cao, R., Hou, D., Cui, P., Zhang, W., Min, T., Lu, Q., Xu, X., Sheng, Z., Xiang, B., and Zhang, Z. Topological Kerr effects in two-dimensional magnets with broken inversion symmetry. *Nature Physics* **20**(7), 1145–1151 (2024).

[93] Suzuki, M.T., Koretsune, T., Ochi, M., and Arita, R. Cluster multipole theory for anomalous Hall effect in antiferromagnets. *Phys. Rev. B* **95**, 094406 (2017).

[94] Bosco, R., Van Den Beucken, J., Leeuwenburgh, S., and Jansen, J. Surface Engineering for Bone Implants: A Trend from Passive to Active Surfaces. *Coatings* **2**(3), 95–119 (2012).

[95] TAKAHASHI, N. and KIKUCHI, H. Rayleigh Criterion: The Paradigm of Photolithography Equipment. *Annals of Business Administrative Science* **16**(5), 203–213 (2017).

[96] Mueller, H. THE THEORY OF PHOTOELASTICITY. *Journal of the American Ceramic Society* **21**(1), 27–33 (1938).

[97] Pandey, A., Dreyer, R., Seyidov, P., Koerner, C., Tirpanci, S., Hazra, B.K., Parkin, S., and Woltersdorf, G. Origin of helicity-dependent photoconductivity in magnetic and nonmagnetic wires. *Phys. Rev. B* **106**, 174420 (2022).

[98] Wang, H., Wang, L., Jakob, D.S., and Xu, X.G. Tomographic and multimodal scattering-type scanning near-field optical microscopy with peak force tapping mode. *Nature Communications* **9**, 2005 (2018).

[99] COMSOL. Heat gradient module. *www.comsol.com* **v 6.2** (2024).

[100] Vansteenkiste, A., Leliaert, J., Dvornik, M., Helsen, M., Garcia-Sanchez, F., and Van Waeyenberge, B. The design and verification of MuMax3. *AIP Advances* **4**(10), 107133 (2014).

[101] Zwarycz-Makles, K. and Majorkowska-Mech, D. Gear and Runge–Kutta Numerical Discretization Methods in Differential Equations of Adsorption in Adsorption Heat Pump. *Applied Sciences* **8**(12), 2437 (2018).

[102] Wang, K., Xu, Z., Huang, Y., Qiu, Y., and Dong, S. Magnetic, thermal, electrical properties and crystallization kinetics of Co60Fe20B20 alloy films. *Sci. China Mater* **59**, 639–647 (2016).

[103] Als-Nielsen, J. and McMorrow, D. *Elements of modern X-ray physics*. John Wiley & Sons (2011).

[104] Robertson, J. Elements of X-ray diffraction by BD Cullity (1979).

[105] Wang, H.W., Shieh, C.F., Chen, H.Y., Shiu, W.C., Russo, B., and Cao, G. Standing [111] gold nanotube to nanorod arrays via template growth. *Nanotechnology* **17**(10), 2689–2694 (2006).

[106] Stephens, P.J. Magnetic Circular Dichroism (1976).

[107] van der Laan, G. and Figueroa, A.I. X-ray magnetic circular dichroism—A versatile tool to study magnetism. *Coordination Chemistry Reviews* **277–278**, 95–129 (2014).

[108] Haertinger, M., Back, C.H., Yang, S.H., Parkin, S.S.P., and Woltersdorf, G. Properties of Ni/Co multilayers as a function of the number of multilayer repetitions. *Journal of Physics D: Applied Physics* **46**(17), 175001 (2013).

[109] You, L., Sousa, R.C., Bandiera, S., Rodmacq, B., and Dieny, B. Co/Ni multilayers with perpendicular anisotropy for spintronic device applications. *Applied Physics Letters* **100**(17), 172411 (2012).

[110] Seifert, P., Vaklinova, K., Ganichev, S., Kern, K., Burghard, M., and Holleitner, A.W. Spin Hall photoconductance in a three-dimensional topological insulator at room temperature. *Nature Communications* **9**, 331 (2018).

[111] Liu, Y., Besbas, J., Wang, Y., He, P., Chen, M., Zhu, D., Wu, Y., Lee, J.M., Wang, L., Moon, J., Koirala, N., Oh, S., and Yang, H. Direct visualization of current-induced spin accumulation in topological insulators. *Nature Communications* **9**, 2492 (2018).

[112] Zeng, X.L., Liu, Y., Zhang, Y., Wu, J., Zhu, S.B., and Chen, Y.H. Observation of the spin-Hall effect in Pt/GaAs by circular polarized photoconductivity. *Optics Express* **30**(2), 2089 (2022).

[113] Liu, Y., Liu, Y., Chen, M., Srivastava, S., He, P., Teo, K.L., Phung, T., Yang, S.H., and Yang, H. Current-induced Out-of-plane Spin Accumulation on the (001) Surface of the $IrMn_3$ Antiferromagnet. *Phys. Rev. Appl.* **12**, 064046 (2019).

[114] Jungwirth, T., Wunderlich, J., and Olejník, K. Spin Hall effect devices. *Nature Materials* **11**(5), 382–390 (2012).

[115] Kukreja, R., Bonetti, S., Chen, Z., Backes, D., Acremann, Y., Katine, J.A., Kent, A.D., Dürr, H.A., Ohldag, H., and Stöhr, J. X-ray Detection of Transient Magnetic Moments Induced by a Spin Current in Cu. *Phys. Rev. Lett.* **115**, 096601 (2015).

[116] Stamm, C., Murer, C., Berritta, M., Feng, J., Gabureac, M., Oppeneer, P.M., and Gambardella, P. Magneto-Optical Detection of the Spin Hall Effect in Pt and W Thin Films. *Phys. Rev. Lett.* **119**, 087203 (2017).

[117] Yang, H., Schmoranzerová, E., Jang, P., Nath, J., Guillet, T., Joumard, I., Auffret, S., Jamet, M., Němec, P., Gaudin, G., and Miron, I.M. Helicity dependent photoresistance measurement vs. beam-shift thermal gradient. *Nature Communications* **13**, 6790 (2022).

[118] Yu, A.Y.C., Donovan, T.M., and Spicer, W.E. Optical Properties of Cobalt. *Phys. Rev.* **167**, 670–673 (1968).

[119] Breitenstein, L., Lendecke, P., Bohlens, S., Meier, G., and Merkt, U. Stray field of a Landau magnetization pattern. *Journal of Applied Physics* **104**(8), 083909 (2008).

[120] You, Y., Lam, H., Wan, C., Wan, C., Zhu, W., Han, L., Bai, H., Zhou, Y., Qiao, L., Chen, T., Pan, F., Liu, J., and Song, C. Anomalous Nernst Effect in an Antiperovskite Antiferromagnet. *Phys. Rev. Appl.* **18**, 024007 (2022).

[121] Ma, L., Zhang, Y., Zhao, H., Fu, H.R., Tang, M., Yang, H.L., Shi, Z., Tian, N., and You, C.Y. Anomalous Nernst effect in epitaxial Fe and FexNi1-x alloy thin films. *AIP Advances* **9**(3), 035227 (2019).

[122] Beckert, S., Godinho, J.a., Johnson, F., Kimák, J., Schmoranzerová, E., Zemen, J., Šobáň, Z.c.v., Olejník, K., Železný, J., Wunderlich, J., Němec, P., Kriegner, D., Thomas, A., Goennenwein, S.T.B., Cohen, L.F., and Reichlová, H. Anomalous Nernst effect in Mn_3NiN thin films. *Phys. Rev. B* **108**, 024420 (2023).

[123] Kumar, C.S. *Magnetic characterization techniques for nanomaterials*. Springer (2017).

[124] Phatak, C., Petford-Long, A., and De Graef, M. Recent advances in Lorentz microscopy. *Current Opinion in Solid State and Materials Science* **20**(2), 107–114 (2016).

[125] Yu, X., DeGrave, J.P., Hara, Y., Hara, T., Jin, S., and Tokura, Y. Observation of the magnetic skyrmion lattice in a MnSi nanowire by Lorentz TEM. *Nano letters* **13**(8), 3755–3759 (2013).

[126] Kasap, S. Thermoelectric effects in metals: thermocouples. *Canada: Department of Electrical Engineering University of Saskatchewan* pages 1–11 (2001).

[127] Sugimoto, S., Nakatani, Y., Yamane, Y., Ikhlas, M., Kondou, K., Kimata, M., Tomita, T., Nakatsuji, S., and Otani, Y. Electrical nucleation, displacement, and detection of antiferromagnetic domain walls in the chiral antiferromagnet Mn_3Sn. *Communications Physics* **3**(111) (2020).

[128] Brown, P.J., Nunez, V., Tasset, F., Forsyth, J.B., and Radhakrishna, P. Determination of the magnetic structure of Mn_3Sn using generalized neutron polarization analysis. *Journal of Physics: Condensed Matter* **2**(47), 9409–9422 (1990).

[129] Grzybowski, M.J., Wadley, P., Edmonds, K.W., Beardsley, R., Hills, V., Campion, R.P., Gallagher, B.L., Chauhan, J.S., Novak, V., Jungwirth, T., Maccherozzi, F., and Dhesi, S.S. Imaging Current-Induced Switching of Antiferromagnetic Domains in CuMnAs. *Phys. Rev. Lett.* **118**, 057701 (2017).

[130] Bodnar, S.Y., Filianina, M., Bommanaboyena, S.P., Forrest, T., Maccherozzi, F., Sapozhnik, A.A., Skourski, Y., Kläui, M., and Jourdan, M. Imaging of current induced Néel vector switching in antiferromagnetic Mn_2Au. *Phys. Rev. B* **99**, 140409 (2019).

[131] Sapozhnik, A.A., Filianina, M., Bodnar, S.Y., Lamirand, A., Mawass, M.A., Skourski, Y., Elmers, H.J., Zabel, H., Kläui, M., and Jourdan, M. Direct imaging of antiferromagnetic domains in Mn_2Au manipulated by high magnetic fields. *Phys. Rev. B* **97**, 134429 (2018).

[132] Tsai, H., Higo, T., Kondou, K., Nomoto, T., Sakai, A., Kobayashi, A., Nakano, T., Yakushiji, K., Arita, R., Miwa, S., Otani, Y., and Nakatsuji, S. Electrical manipulation of a topological antiferromagnetic state. *Nature* **580**(7805), 608–613 (2020).

[133] Higo, T., Kondou, K., Nomoto, T., Shiga, M., Sakamoto, S., Chen, X., Nishio-Hamane, D., Arita, R., Otani, Y., Miwa, S., and Nakatsuji, S. Perpendicular full switching of chiral antiferromagnetic order by current. *Nature* **607**(7919), 474–479 (2022).

[134] Soldatov, I.V. and Schäfer, R. Selective sensitivity in Kerr microscopy. *Review of Scientific Instruments* **88**(7), 073701 (2017).